

POLITECNICO DI TORINO

Corso di Laurea Magistrale in Ingegneria Meccanica

Master Thesis

**Quench Protection Heaters FE Analysis and
Thermal Conductivity Measurements of Nb₃Sn
Cables for High-Field Accelerator Magnets**



Supervisor:

Prof. Lorenzo PERONI

Author:

Carmelo BARBAGALLO

CERN Supervisor:

Susana IZQUIERDO BERMUDEZ

April 2020

Declaration of Authorship

I, Carmelo BARBAGALLO, declare that this thesis titled, “Quench Protection Heaters FE Analysis and Thermal Conductivity Measurements of Nb₃Sn Cables for High-Field Accelerator Magnets” and the work presented in it are my own. I confirm that:

- This work was done while in candidature for the Technical Student Programme at CERN (The European Organization for Nuclear Research).
- Where any part of this thesis has previously been submitted for a degree or any other qualification at this University or any other institution, this has been clearly stated.
- Where I have consulted the published work of others, this is always clearly attributed.
- Where I have quoted from the work of others, the source is always given. With the exception of such quotations, this thesis is entirely my own work.
- I have acknowledged all main sources of help.
- Where the thesis is based on work done by myself jointly with others, I have made clear exactly what was done by others and what I have contributed myself.



Signed:

A handwritten signature in black ink that reads "Carmelo Barbagallo".

Date:

06/02/2020

“Remember to look up at the stars and not down at your feet. Try to make sense of what you see and wonder about what makes the universe exist. Be curious. And however difficult life may seem, there is always something you can do and succeed at. It matters that you don't just give up”

Prof. Stephen Hawking

Abstract

Mechanical Engineering
Department of Mechanical and Aerospace Engineering

Master of Science

Quench Protection Heater FE Analyses and Thermal Conductivity Measurements of Nb₃Sn cables in High-Field Accelerator Magnets

by Carmelo BARBAGALLO

The Large Hadron Collider (LHC), the world's largest and most powerful particle accelerator, represents a research instrument at CERN to improve our understanding of matter and the Universe. To date, scientists and engineers around the world are working hard to develop its upgrade, the High-Luminosity LHC (HL-LHC). More powerful superconducting accelerator magnets are being designed at CERN, allowing the peak magnetic field strength to be augmented by around 50% than current LHC magnets. These magnets will permit to increase the HL-LHC integrated luminosity - i.e. the total number of collisions - by a factor of ten beyond the LHC's design value, allowing the scientific community to study the phenomena discovered at the LHC in greater detail.

Due to the high peak field, in the range of 12 T to 13 T, magnets will use an innovative superconducting technology based on the use of Nb₃Sn as superconductor. From this perspective, quench protection is becoming a topic of very high interest. That means preventing damage in the case of an unexpected loss of superconductivity and the heat generation related to that. This procedure foresees the disconnection of the magnet current supply and the use of so-called protection heaters. The heaters suppress the superconducting state in a large fraction of the windings and permit a uniform dissipation of the stored energy.

In this thesis work, a numerical analysis on state-of-the-art quench protection heaters for high-field accelerators magnets is proposed, aiming to investigate on their performance and evaluate the prospects in high-field magnet protection. FE-analyses simulating the heat transfer from protection heater to superconducting cables in Nb₃Sn magnets were carried-out in COMSOL Multiphysics[®], in order to evaluate the heater efficiency from time delay between the heater activation and normal zone initiation in the coil. Results from simulations were compared with measured data from R&D Nb₃Sn quadrupoles and dipoles under development at CERN for HiLumi project. The thesis was also focused on the study of the thermal conductivity of epoxy-impregnated coils, for having a better understanding of this thermal property which plays a key role in heat transfer phenomena during a quench. Thermal conductivity of different insulating materials used in Nb₃Sn impregnated coils was studied. Finally, a multi-strand cables FE-model was built in COMSOL to replicate the experimental procedure used at CERN Cryolab to measure the thermal conductivity of epoxy-impregnated Nb₃Sn Rutherford cable stacks.

POLITECNICO DI TORINO

Sommario

Ingegneria Meccanica
Dipartimento di Ingegneria Meccanica e Aerospaziale

Corso di Laurea Magistrale

Quench Protection Heater FE Analyses and Thermal Conductivity Measurements of Nb₃Sn cables in High-Field Accelerator Magnets

A cura di Carmelo BARBAGALLO

Il *Large Hadron Collider* (LHC), il più grande e potente acceleratore di particelle del mondo, rappresenta al CERN uno strumento di ricerca per migliorare la comprensione della materia e dell'Universo. Ad oggi, scienziati e ingegneri di tutto il mondo stanno lavorando duramente per lo sviluppo del suo *upgrade*, l'*High-Luminosity LHC* (HL-LHC). Al CERN sono stati progettati magneti superconduttori più potenti, che consentono di aumentare l'intensità di picco del campo magnetico di circa il 50% rispetto ai magneti dell'attuale LHC. Questi magneti permetteranno di aumentare la luminosità integrata dell'HL-LHC – cioè il numero totale di collisioni – di un fattore dieci oltre il valore di progetto dell'LHC, permettendo alla comunità scientifica di studiare in maggiore dettaglio i fenomeni scoperti con l'LHC.

A causa dell'alto campo magnetico, tra i 12 T e i 13 T, i magneti utilizzeranno un'innovativa tecnologia superconduttiva basata sull'utilizzo del superconduttore Nb₃Sn. In questo scenario, lo studio del sistema di protezione nel caso di *quench* sta diventando un argomento di notevole interesse. Ciò significa prevenire danni al magnete nel caso di un'improvvisa perdita dello stato superconduttivo e della generazione di calore a essa correlata. In caso di quench, la procedura prevede la disconnessione dell'alimentazione della corrente del magnete e l'utilizzo di elementi riscaldanti, chiamati *protection heater*. Tali elementi sopprimono lo stato superconduttivo in una grande frazione degli avvolgimenti del magnete e consentono una dissipazione uniforme dell'energia immagazzinata.

Nel presente lavoro di tesi viene proposta un'analisi numerica sullo stato dell'arte dei *protection heater* usati in magneti ad alto campo magnetico per acceleratori di particelle, al fine d'indagare sulle loro prestazioni e valutare nuove prospettive nella protezione di tali magneti. Analisi agli elementi finiti, che simulano lo scambio termico nei magneti tra gli heater e i cavi superconduttori in Nb₃Sn, sono state effettuate in COMSOL Multiphysics® al fine di determinare l'efficienza dell'heater tramite la valutazione dell'*heater delay*, ossia il tempo che intercorre tra l'attivazione dell'heater e l'inizio dello stato resistivo nella bobina. I risultati delle simulazioni sono stati confrontati con le misure sperimentali effettuate sui quadrupoli e dipoli basati su tecnologia Nb₃Sn, in sviluppo al CERN per il progetto *HiLumi*. Il lavoro di tesi è stato anche incentrato sullo studio della conducibilità termica delle bobine impregnate con resina epossidica, al fine di avere una migliore comprensione di questa proprietà termica che svolge

un ruolo fondamentale nei fenomeni di scambio termico durante il *quench*. Infine, un modello agli elementi finiti di un cavo multi-filamento è stato realizzato in COMSOL Multiphysics®, con lo scopo di replicare numericamente la procedura sperimentale utilizzata dal laboratorio Cryolab al CERN per misurare la conducibilità termica di provini di cavi in Nb₃Sn di tipo Rutherford impregnati con resina epossidica.

Acknowledgments

This Master Thesis work was developed at CERN (The European Organization for Nuclear Research) while in candidature for the Technical Student Programme. I feel very grateful for this exceptional experience I have had during this year at CERN, both professionally and personally. This opportunity allowed me to work in the one of the best research center in the world, in direct contact with the best scientists from all over the world. From a professional point of view, I learned a lot about research world, in particular magnet technology development and numerical modelling. From a personal point of view, I appreciated the possibility to know different cultures and people. That has allowed me to know better myself and to respect the others, as well as to enrich my person for a cultural point of view.

One of the best parts of completing this thesis is to have the opportunity to formally thank the people who have made this experience that what it was. First, I thank Susana Izquierdo Bermudez, my supervisor at CERN, for her guidance on investigated topics and trust in my abilities. I thank Prof. Lorenzo Peroni, my supervisor at the Polytechnic University of Turin, for his academic supervision, support and trust since the early stage of this experience. I also thank Tiina Salmi for her interest in my work, cooperation during tests in SM18 facility and guidance in quench modelling. I thank Patricia Tavares Coutinho Borges De Sousa, Torsten Koettig and Beatriz Del Valle Grande for their help in thermal conductivity activity. I thank Marco Morrone for his help, the interesting sharing on finite element simulations and for encouraging conversations. I also thank Nicola Cersullo for his friendship and for having shared this experience at CERN from the first day. I thank Fabrizio Niccoli for his suggestions and for funny moments during lunches and coffee breaks in cafeteria. I thank all my colleagues of Magnet Design & Technology section of CERN for all expertise shared. For their support, big thanks to my friends Guglielmo Luca Bambino and Matteo Armando. I shared with them my university experience in a way that they became very good friends. I want to thank my Family to have trusted always in me, my “second family” in Turin, and my friends from Ramacca and Geneva.

Last but not least, special thanks to my girlfriend Giuliana. She has always supported me in all decisions and strongly encouraged me with her unconditional love.

Contents

Declaration of Authorship	iii
<i>Abstract</i>	vii
<i>Sommario</i>	viii
<i>Acknowledgments</i>	x
List of Abbreviations	xvi
List of Symbols	xx
1. Introduction	24
1.2 Scope of the thesis	25
1.3 Structure of the thesis.....	25
2. The LHC and the HL-LHC	26
2.1 The Large Hadron Collider	26
2.2 The CERN accelerator complex	27
2.3 The High-Luminosity Large Hadron Collider.....	30
2.3.1 Luminosity	30
2.3.2 Machine upgrade.....	31
3. Superconducting accelerator magnets and their protection	32
3.1 Superconducting accelerator magnets	32
3.1.1 Particle accelerators and their physics	32
3.1.2 The LHC main magnets and their general features.....	33
3.1.3 Superconducting materials in accelerator magnets	35
3.1.4 Practical wires and cables for magnets	36
3.1.5 LHC dipole and quadrupole magnets.....	38
3.1.6 Nb ₃ Sn magnets for HiLumi upgrade.....	42
3.2 Quench protection in superconducting magnets.....	45
3.2.1 What is a quench?	45
3.2.2 Quench detection and current supply disconnection.....	46
3.2.3 Temperature rise and MIITs	47
3.2.4 Quench protection strategies.....	48
3.2.5 Heater designs.....	49
4. Quench protection heater numerical simulation	55
4.1 Quench heater delay: from experimental procedure to numerical thermal model.....	55
4.1.1 Quench heater delay experimental procedure	55
4.1.2 Domain modelling	56
4.1.3 Governing equation.....	59

4.1.4	Boundary conditions	59
4.1.5	Material properties	60
4.1.6	Current sharing temperature.....	62
4.1.7	Numerical solution.....	63
4.2	Quench heater delay analysis for MQXFS5 magnet.....	64
4.2.1	Quench heater delay simulations results	64
4.2.2	Heater temperature profile	70
4.2.3	Heat diffusion in the coil.....	71
4.3	Quench heater analysis results and for 11 T magnet	71
4.3.1	Quench heater delay simulations results	71
4.4	Estimation of the heater adiabatic temperature.....	82
4.4.1	Analytical approach	82
4.4.2	FE heater model approach	83
4.5	Concluding remarks on quench heater analysis	84
5.	Steady-state measurements and numerical modelling of thermal conductivity of impregnated Nb₃Sn cable stacks	85
5.1	Thermal conductivity of single components.....	85
5.1.1	Evaluation of the interface resistance	88
5.1.2	Epoxy resin thermal conductivity	92
5.1.3	Impregnated S2-glass thermal conductivity.....	92
5.1.4	Impregnated S2-glass with binder thermal conductivity	93
5.1.5	Impregnated S2-glass-mica with binder thermal conductivity	93
5.2	Thermal conductivity measurements of coil segments and cable stacks components.....	95
5.2.1	Steady-state measurement method.....	98
5.2.2	Experimental setup description.....	100
5.2.3	Experimental results.....	101
5.3	Numerical model of Nb ₃ Sn cable stacks.....	105
5.3.1	Model implementation	105
5.3.2	Strand transposition effect modelling	111
5.3.3	Interfacial thermal contact resistance modelling.....	112
5.3.4	Numerical solution.....	116
5.4	Results of thermal conductivity simulations on Nb ₃ Sn cables stacks.....	116
5.4.1	Results of <i>Case A</i> : thermal conductivity of coil sample #3	116
5.4.2	Results of <i>Case B</i> : strand transposition effect on thermal conductivity of coil sample #3	120
5.4.3	Results of <i>Case C</i> : effect of interstand thermal resistance on thermal conductivity of coil sample #3	121

5.4.4	Results of the analogy between thermal and electrical contact resistance	125
5.5	Concluding remarks on cable stacks analysis	128
6.	Conclusions	130
Annex 1	132
Section 1:	Real coil resistive voltage signals from tests MBHSP106 magnet	132
Annex 2	134
Section 1:	Thermal conductivity measurements for single components	134
Section 2:	Thermal conductivity measurements for coil segments	141
References	146

List of Abbreviations

11 T	Dipole magnet developed in collaboration with Fermilab and CERN
ALICE	A Large Ion Collider Experiment, one of the four main LHC experiments
ATLAS	A Toroidal LHC ApparatuS, one of the four main LHC experiments
B1	Low field coil block for MBHSP106 magnet
B2	Medium field coil block for MBHSP106 magnet
B3	High field coil block for MBHSP106 magnet
Bi-2212	Bismuth based high temperature superconductor
BDF	Backward Differentiation Formulas
BSCCO	Bismuth based high temperature superconductors
CERN	European Organization for Nuclear Research
Cernox	Temperature sensors for thermal conductivity measurements of coil sample
CMS	Compact Muon Solenoid, one of the four main LHC experiments
CMY	Cooper-Mikic-Yovanovic plastic model
Cryolab	The CERN Central Cryogenic Laboratory
COMSOL	A FEM based simulation software
CTD-101K	Epoxy resin used in Nb ₃ Sn cables
CTD-1202	Ceramic binder
Cu	Copper
Cu/SC, Cu/non-Cu	Copper to superconductor ratio
FE	Finite element
FEM	Finite element method
Fermilab, FNAL	Fermi National Accelerator Laboratory in Batavia, Illinois, US
GM, GMG, GMHT	Samples made of different combination of mica/glass and glass sheet
G10	G10 fiberglass epoxy
HFU	Heater Firing Unit
HiLumi	LHC luminosity upgrade program
HiLumi LHC	High-Luminosity Large Hadron Collider
HL-LHC	High-Luminosity Large Hadron Collider
HS	Heater station
HT	Heat treatment
HTS	High temperature superconductor
IDA	Implicit Differential-Algebraic solver
IL	Inner coil layer
INFN	The National Institute for Nuclear Physics
INFN-LASA	Laboratory for Accelerators and Applied Superconductivity of INFN
InL	Inter layer of the coil
InL-HF	Inter layer high field quench heaters
InL-MF	Inter layer medium field quench heaters
InL-LF	Inter layer low field quench heaters
InL-QH	Only inter layer quench heater fired configuration
IP	Interaction point

IR	Interaction-region in LHC
ISOLDE	The Isotope mass Separator On-Line facility
LEP	Large Electron-Positron Collider
LHC	Large Hadron Collider
LHCb	Large Hadron Collider beauty, one of the four main LHC experiments
LHe	Liquid helium
LINAC 2	Linear Accelerator 2
LTS	Low temperature superconductor
MB	LHC main dipole Nb-Ti magnet
MBH	LHC main dipole Nb ₃ Sn magnet under development
MBHSP106	Short model of MBH magnet equipped with inter layer quench heaters
MIITs	Current decay integral
MQ	LHC main quadrupole Nb-Ti magnet
MQXA	LHC IR quadrupole Nb-Ti magnet
MQXB	LHC IR quadrupole Nb-Ti magnet
MQXF	LHC IR upgrade quadrupole Nb ₃ Sn magnet under development
MQXFS	Short model of MQXF magnet
Nb	Niobium
Nb ₃ Sn	Niobium-tin based low temperature superconductor
Nb-Ti	Niobium-titanium based low temperature superconductor
LARP	The US LHC Accelerator Research Program
OFHC	Oxygen-free high thermal conductivity copper
OL	Outer coil layer
OL-HF	Outer layer high field
OL-LF	Outer layer low field
OL-QH	Only outer layer quench heater fired configuration
OL-QH+InL-QH	Outer layer and inter layer quench heaters both fired
PDEs	Partial Differential Equations
PH	Protection heater
PIT	Powder in tube process for superconducting wires
PS	Proton Synchrotron
PSB	Proton Synchrotron Booster
QH	Quench heater
QXF, MQXF	LHC IR upgrade quadrupole Nb ₃ Sn magnet under development
R&D	Research and Development
RF	Radio-frequency cavities
RMS	Root mean square
RRR	Residual resistivity ratio
SC	Superconductor
S2-glass	Glass fiber used in Nb ₃ Sn cables
Sn	Tin
SM18	CERN magnet test facility
SS	Stainless-steel
SSL	Current short sample limit for a cable

SPS	Super Proton Synchrotron
Stycast [®]	High thermal conductivity epoxy resin
Ti	Titanium
TVO	Temperature sensor
U.S.	United States
YBCO	Yttrium based high temperature superconductor

List of Symbols

A	Cross-sectional of the sample
A_a	Apparent cross-section or nominal area
A_c	Contact area
A_{cable}	Cross-sectional area of the cable
A_v	Void area
B	Magnetic field
b	Length of coil sample #3 in z -direction
\tilde{b}	Reduced magnetic field
B_c	Critical magnetic field
B_{c1}	Lower critical field
B_{c2}	Upper critical field
B_{c20}	Upper critical field at zero temperature and strain
B_{op}	Operational conductor peak field
B_x	Horizontal component of the magnetic field
B_y	Vertical component of the magnetic field
C	Capacitance of heater power supply
\tilde{C}	Experimental constant in Wiedemann-Franz law for contact resistances
C_0	Normalization constant in ITER-2008 critical surface parametrization
c	Speed of light ($c = 299,792,458$ m/s)
c_p	Specific heat
$C_{p,ss}$	Volumetric heat capacity of stainless-steel
d_{QH}	Heater thickness
E	Electric field
E_{dump}	Energy dissipated in the dump resistor
E_{QH}	Energy dissipated in the quench heater
F	Geometric luminosity reduction factor
F_L	Lorentz force
f_i	Fraction areas of the different components in a Rutherford cable
f_{rev}	Revolution frequency
G	Quadrupole gradient
G_{op}	Operational gradient
H_c	Surface microhardness
h_c	Contact conductance
h_{cable}	Cable thickness
h_g	Gap conductance
h_j	Joint thermal contact conductance
I	Current
h_r	Radiative conductance
I_0	Current at $t=0$
I_{cable}	Current flowing in the cable
I_c	Critical current

$I_{\text{nom}}, I_{\text{op}}$	Nominal (or operational) current
I_{mag}	Magnet current
I_{QH}	Quench heater current
I_{QH_0}	Quench heater current at $t=0$
I_{ss}	Short sample current
I_{ult}	Ultimate current
J	Current density
J_{c}	Critical current density
J_{Cu}	Current density in copper
J_{ss}	Heater current density
k	Thermal conductivity
$k_{\text{cable}}(T)$	Thermal conductivity computed in COMSOL for coil sample #3 (<i>Case A</i>)
$k_{\text{ins,azimuthal}}$	Derived thermal conductivity of azimuthal sample insulation
$k_{\text{ins,radial}}$	Derived thermal conductivity of radial sample insulation
$k_{\text{ins,stacks}}$	Derived thermal conductivity of stack parallel sample insulation
$k_{\text{long}}(T)$	Thermal conductivity along the strands
$k_{\text{long}}^i(T)$	Thermal conductivity contribution along the strands for each material
k_{pitch}	Strand transposition effect contribution on the transverse thermal conductivity
k_{s}	Harmonic mean thermal conductivity
k_{sample}	Experimental thermal conductivity of the sample
$k_{\text{tot}}(T)$	Total transverse thermal conductivity of the sample
L	Active length of a sample / Distance between two Cernox sensors
L_{m}	Machine luminosity
L_{mag}	Magnet inductance
L_{pitch}	Twist pitch length
L_{transp}	Transposition length
l_{QH}	Quench heater length
m	Effective mean absolute asperity slope of surface profile
N_{b}	Number of particles per bunch
n_{b}	Number of bunches per beam
N_{event}	Number of events generated in the collisions
N_{s}	Number of cables in a coil sample
P	Power applied through sample heaters
P_{lower_i}	Computed power at the lower part of the interstrand interface for the i -cable
P_{upper_i}	Computed power at the upper part of the interstrand interface for the i -cable
$P_{\text{QH}}(t)$	Surface power density of the heater
$P_{\text{QH}}(0)$	Surface peak power density of the heater
p	Contact pressure
p_{q}	Modulus of particle momentum
PH_{period}	Length of a heater period
\dot{Q}	Heat flux in vertical direction
q	Charge of particle

$q_{\text{gen,ss}}$	Volumetric heat generation in stainless-steel heater
R	Heater circuit resistance
R_{bulk}	Thermal resistance of the bulk material
R_{dump}	Resistance of dump resistor
R_{el}	Electrical contact resistance
$R_{\text{el}i}$	Electrical contact resistance for the considered i -cable
R_{int}	Thermal resistance of the copper-to-resin interface
R_{th}	Thermal contact resistance
$R_{\text{th}i}$	Interstrand thermal resistance for the considered i -cable
R_{mica}	Thermal resistance of mica
$R_{\text{quench}}(t)$	Resistance of the normal zone
R_{QH}	Heater strip resistance
$R_{\text{S-2}}$	Thermal resistance of S-2 glass
R_{tot}	Total measured thermal resistance of an 11 T sample
$R_{\text{tot}}(\#5)$	Total thermal resistance of sample #5
R_{w}	Wiring resistance
r	Radius of curvature of accelerator orbit
r_{in}	Coil inner radius
r_{out}	Coil outer radius
S	Volumetric heat capacity
$s(\varepsilon)$	Strain function
T	Temperature
\bar{T}, T_{ave}	Average temperature between two Cernox sensors
T_{bath}	Temperature of helium bath
T_1	Temperature recorded by sensor Cernox 1
T_2	Temperature recorded by sensor Cernox 2
T_{c}	Critical temperature
T_{cold}	Temperature of the cold heat sink
T_{cs}	Current sharing temperature
T_{ct}	Average temperature of the contacting surfaces
$T_{\text{ct}i}$	Average temperature of the contacting surfaces for the i -cable
$T_{\text{fin.}}$	Final temperature of the heater (analytical approach)
$T_{\text{lower}i}$	Computed temperature at the lower part of the interstrand interface
$T_{\text{upper}i}$	Computed temperature at the upper part of the interstrand interface
T_{max}	Maximum temperature in the cable
T_{op}	Operational temperature
T_{QH}	Quench heater temperature
t	Time
\tilde{t}	Reduced temperature
t_{delay}	Delay time between quench initiation and protection activation
t_{ins}	Insulation thickness of the cable
$t_{\text{int.layer}}$	Insulation thickness of the inter layer

$t_{\text{int.OD}}$	Insulation thickness of outer diameter coil insulation
$t_{\text{int.ID}}$	Insulation thickness of inner diameter coil insulation
U	Voltage
U_c	Voltage across the capacitor
U_{max}	Maximum voltage across magnet terminals
U_{QH}	Voltage across the quench heater
$U_{\text{QH,max}}$	Maximum voltage across the quench heater
U_{th}	Voltage threshold for quench detection
V_{QH}	Quench heater volume
x_i	Load line fraction
w_{QH}	Heater width
v	Particle velocity
β^*	Beta function at the collision point
γ	Mass density
γ_c	Electric conductivity
$\tilde{\gamma}_r$	Relativistic gamma factor
ΔT	Absolute temperature gradient between two temperature sensors
ΔT_i	Temperature gradient at the interface between two strands of a cable i
ε	Intrinsic longitudinal strain
ε_n	Normalized transverse beam emittance
θ_c	Full crossing angle at the interaction point
λ_{Cu}	Cable copper fraction
μ_0	Vacuum permeability ($\mu_0 = 4\pi \cdot 10^{-7} \text{ Tm/A}$)
ρ	Resistivity
ρ_{Cu}	Resistivity of copper
ρ_{ss}	Stainless-steel resistivity
σ	Effective RMS surface roughness
σ_{event}	Cross-section of the event
σ_z	RMS bunch length
σ^*	Transverse RMS beam size at the interaction point
τ	Time constant of the heater pulse
τ_e	Characteristic extraction time
φ	Twisting angle

Chapter 1

Introduction

The discovery of superconductivity by Professor Heike Kamerlingh Onnes and his collaborators in 1911 represented a remarkable achievement in low-temperature physics and evoked hopes for no-loss electrical transmission to improve various applications, among which building of superconducting magnets for high-energy particle accelerators appears to be the most challenging. The Large Hadron Collider (LHC) at CERN (Geneva, Switzerland) represents the largest application of superconductivity. After many years of advancement both in the theoretical understanding and in the fabrication methods, superconducting magnets are used today in medical applications, i.e. radiotherapy with hadrons or ions, particle accelerators and detectors.

This thesis focuses on superconducting magnets designed for Hi-Luminosity LHC. The aim of the present work is to analyze the design and performance of magnet protection system in case of a quench, i.e., the irreversible loss of superconductivity in the winding, which is one of the most important aspects in magnets design for particle accelerators. The goal of the quench protection system is to safely discharge the energy stored in the magnet to avoid overheating and consequently damaging of the windings. The protection system is based on electric quench protection heaters which suppress the superconducting state over a large fraction of the winding permitting a fast and uniform dissipation of the stored energy. The heater efficiency is higher the faster they deposit energy to the coils in order to increase their temperature above the critical temperature of superconductor and provoke a quench. During the accelerator operation superconducting magnets are subjected to overheating caused by hysteretic losses and continuous heat deposition on the coils. Consequently, the knowledge of thermal properties of coil components, i.e., the thermal conductivity of cable insulating layers, is of crucial importance to understand the heat diffusion along the coil, for example during a quench. Superconducting magnets are designed to have very small mechanical and thermal tolerances, and to work in a highly controlled environment. For this reason, FE analysis represents a fundamental approach to study in depth the mechanical and thermal behavior of magnets, in order to optimize components in their design phase and ensure magnet's reliability and performance. The research contained in this thesis analyzes three relevant topics:

- a numerical analysis on state-of-the-art heaters in Nb₃Sn based accelerator magnets aiming to evaluate their performance and validate design for future magnets;
- a benchmark of results from quench heater delay simulations with experimental data coming from CERN SM18 magnet test facility;
- a numerical investigation on thermal conductivity of impregnated Nb₃Sn coil samples and comparison with experimental data coming from CERN Cryolab.

1.2 Scope of the thesis

This study aimed to investigate on the efficiency of quench protection heaters for high-field accelerator magnets and explore the thermal conductivity of Nb₃Sn cable samples and their single components. Starting from a real coil model, FE-based models were built-up by considering different conditions in model implementation to simulate the heater delay in the coil, i.e., the time delay between the heater activation and consequent normal zone initiation in the winding. Parametric thermal transient studies were performed by changing various design and powering parameters to understand the impact on heater performance. Results obtained from simulations were compared with experimental data from CERN SM18 to validate the simulated delays. As second part of the thesis, after having carried-out a study on the thermal conductivity of cable single components, numerical stationary thermal simulations were developed to estimate the overall thermal conductivity of Nb₃Sn cable samples. Implemented models allow to numerically replicate the experimental procedure used at CERN Cryolab to measure the thermal conductivity of epoxy-impregnated Nb₃Sn Rutherford cable stacks. Results obtained were then compared with experimental data coming from CERN Cryolab. Parametric studies on the implementation of interstand thermal contacts were also carried-out to improve numerical model. Models were implemented and solved using COMSOL Multiphysics[®], a commercial multiphysics Finite Element Method (FEM) software capable of solving physical problems expressed as systems of Partial Differential Equations (PDEs).

This research focuses on Nb₃Sn dipoles (11 T) and quadrupoles (MQXF) that are being developed for the LHC luminosity upgrade by the U.S. LARP (LHC Accelerator Research Program) collaboration.

1.3 Structure of the thesis

Chapter 2 gives an overview on the Large Hadron Collider (LHC) and the CERN accelerator complex, while in the second part the High Luminosity Large Hadron Collider (HL-LHC) project is presented. Chapter 3 describes general characteristics, design and fabrication of superconducting magnets used in the LHC and in its planned upgrade, focusing on principal aspects related to magnet quench protection. Then, characteristics of quench protection design for superconducting magnets are shown in detail. Chapter 4 presents a 2-D heat conduction FE model to simulate the quench heater delay in superconducting coil. This simulation model was applied to MQXF and 11 T magnets for several investigated studies and results were compared with experimental data. Chapter 5 presents an investigation on thermal conductivity of Rutherford cable components. A 2-D-FE model to measure the thermal conductivity of epoxy-impregnated Nb₃Sn Rutherford cable stacks is presented, as well as a comparison with experimental data.

Chapter 2

The LHC and the HL-LHC

The Large Hadron Collider (LHC) is the world's largest and most powerful particle collider built to date. The purpose of the LHC is to allow physicists to test the predictions of different theories of particle physics and continue to push our understanding of the fundamental structure of the universe. Nowadays, scientists and engineers around the world are developing its upgrade, the High Luminosity Large Hadron Collider (HL-LHC). This challenging upgrade aims to increase the integrated luminosity of the machine by a factor of ten beyond the LHC's design value, in order to observe rare phenomena and collect more accurate measurements.

2.1 The Large Hadron Collider

The Large Hadron Collider (LHC) is a two-ring superconducting hadron accelerator and collider built by the European Organization for Nuclear Research (CERN) between 1998 and 2008 and located in the Franco-Swiss border on the outskirts of Geneva. The LHC is installed approximately 175 m underground in the already existing 26.7 km tunnel that previously housed the Large Electron-Positron Collider (LEP) [Eva2008]. An aerial view of CERN and the surrounding region is shown in figure 2.1.



Figure 2.1: Aerial view of CERN and the surrounding region. The three drawn rings show the position of the accelerator complex located underground. The small ring is the Proton Synchrotron (PS), the middle ring is the Super Proton Synchrotron (SPS) and the largest ring is the Large Hadron Collider (LHC) [CERN1991].

The LHC is designed to produce proton-proton collisions at a center of mass energy of 14 TeV and a luminosity of up to $10^{34} \text{ cm}^{-2} \text{ s}^{-1}$, i.e., the number of collisions per cm^2 and per second, which leads to around bunches of protons collisions every 25 ns (600 million collisions per second) [Eva2008]. The goal of the LHC and its experiments is to reveal the physics beyond

the Standard Model, providing experimental evidences for new particles, such as the Higgs boson discovered in 2012, new forces and new symmetries or evidences of extra space dimensions [Gia2015].

2.2 The CERN accelerator complex

The LHC's rings consist of superconducting magnets and accelerating cavities in which the counter-rotating proton beams are accelerated at 299,792,455 m/s (99.999999% of the speed of light) inside pipes under ultra-high vacuum. Radio-frequency (RF) cavities increase the particle energy at every turn, producing an alternating electrical potential that acts on the particles as an accelerating field. Dipole and quadrupole magnets respectively bend and focus the proton beams into their circular trajectory. This equipment is mostly superconducting, which calls for a comprehensive cryogenic system [Tay2000].

Before to reach the desired energy, the proton beams pass through several acceleration steps in a succession of machines that compose the accelerator complex. A schematic view of the CERN accelerator complex is shown in figure 2.2.

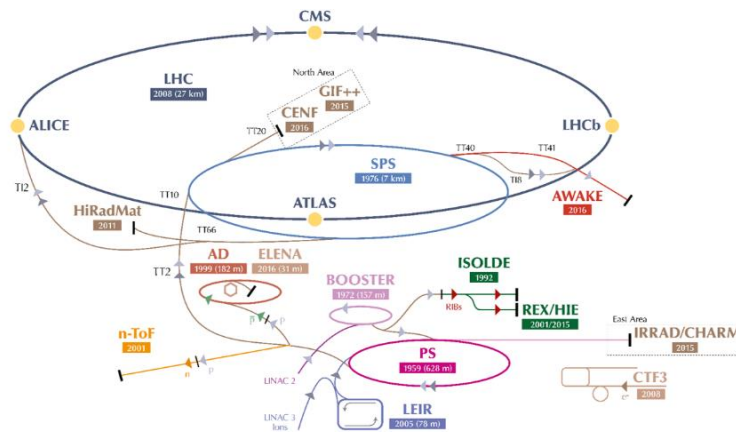


Figure 2.2: Schematic view of the CERN accelerator complex. The LHC is the last ring (dark blue) in a complex series of particle accelerators. The four main LHC experiments – ALICE, ATLAS, CMS and LHCb – are shown at the interaction points (indicated in yellow) [CERN2016].

Firstly, protons are obtained by ionization of hydrogen gas and accelerated up to the energy of 50 MeV into the Linear Accelerator 2 (LINAC 2). Then, the beam is injected into the Proton Synchrotron Booster (PSB), where protons are accelerated up to 1.4 GeV. Successively, the Proton Synchrotron (PS) accelerates protons up to 25 GeV and injects them into the Super Proton Synchrotron (SPS), where they are accelerated to 450 GeV. Finally, protons enter into the two LHC beam pipes where they reach their maximum energy of 7 TeV. The beam in one pipe circulates clockwise while the beam in the other pipe goes anticlockwise. The two beams are brought in collision inside four detectors – ALICE, ATLAS, CMS and LHCb – where the total energy at the collision point is equal to 14 TeV [CERN2012a]. Levels of energy and speeds

reached by protons along their path inside the accelerator complex are summarized in table 2.1. LHC main technical parameters are reported in table 2.2.

Table 2.1: Levels of energy and speeds of protons inside the accelerator complex [CERN2012a].

Accelerator	Speed [% c]	Kinetic energy of proton
LINAC 2	31.4	50.0 MeV
PSB	91.6	1.4 GeV
PS	99.93	25.0 GeV
SPS	99.9998	450.0 GeV
LHC	99.999999	7.0 TeV

Table 2.2: LHC main technical parameters [LHCCLOSER].

Parameter	Unit	Value
Circumference	[m]	26,659
Dipole operating temperature	[K]	1.9
Number of magnets	[-]	9,300
Peak magnetic dipole field	[T]	8.33
Nominal energy, protons	[TeV]	7
Nominal energy, ions	[TeV/nucleon]	2.76
Minimum distance between bunches	[m]	~ 7
Bunch spacing	[ns]	25
Design luminosity	[$\text{cm}^{-2} \text{s}^{-1}$]	10^{34}
No. of bunches per proton beam	[-]	2,808
No. of protons per bunch (at start)	[-]	$1.15 \cdot 10^{11}$
Number of turns per second	[-]	11,245

The accelerator complex includes also several facilities, such as the Isotope mass Separator On-Line (ISOLDE) facility dedicated to the production of a large variety of radioactive ion beams for many different experiments in nuclear physics and life sciences [CERN2017].

The four main LHC detectors have been built to record and study collisions and investigate on different physical phenomena:

- **ALICE:** A Large Ion Collider Experiment, designed to study heavy ion collisions [CERN2012b];
- **ATLAS:** A Toroidal LHC ApparatuS, a general-purpose detector that investigates a wide range of physics, from the search for the Higgs boson to particles that could make up dark matter. A real image of ATLAS detector is shown in figure 2.3 [CERN2012c];
- **CMS:** The Compact Muon Solenoid, a general-purpose detector that studies a wide range of physics processes. It has the same scientific goal as the ATLAS experiments,

but it uses different technical solutions and a different magnet-system design [CERN2012d].

- **LHCb:** The Large Hadron Collider beauty, a detector that investigates on differences between matter and antimatter by studying heavy particles containing a b-quark [CERN2012e].

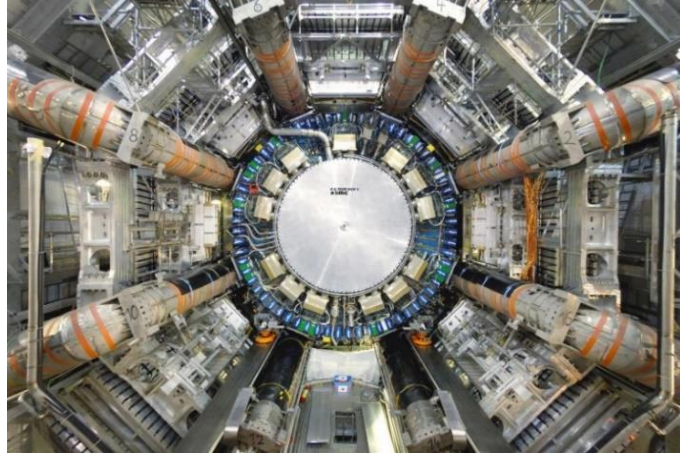


Figure 2.3: A real image of ATLAS detector, one of the four main LHC experiments [CERN2012c].

The particle collisions allow the LHC to create in the experiments a superheated mixture of subatomic particles called *quark-gluon plasma*, which pervaded the Universe immediately after the Big Bang. An image of a proton-proton collision event at CMS is shown in figure 2.4.

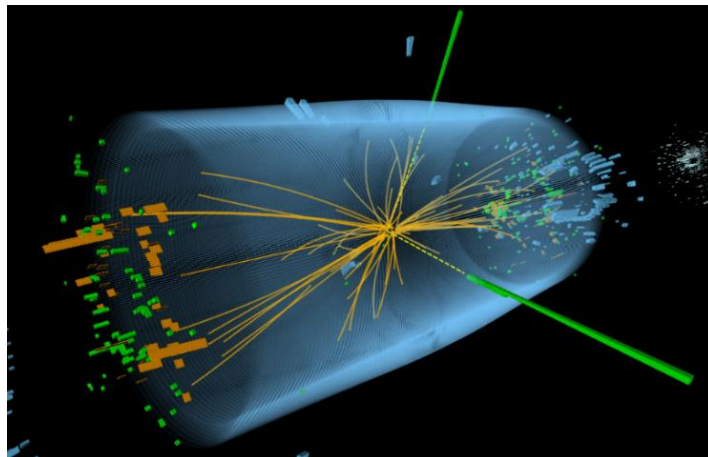


Figure 2.4: A proton-proton collision event at CMS detector [CERN2012f].

The first collision started in 2009 [CERN2009] and in 2012 the ATLAS and CMS experiments announced the achievement of one of the main LHC goals, that is the experimental observation of the particle called *Higgs boson* predicted by the Standard Model [CERN2014]. In 2013 theoretical physicists François Englert and Peter W. Higgs were jointly awarded the Nobel Prize

in Physics for the theory of the Higgs mechanism “that contributes to our understanding of the origin of mass of subatomic particles, and which was confirmed through the discovery of the predicted fundamental particle, by the ATLAS and CMS experiments at CERN’s Large Hadron Collider” [NOBEL2013]. This discovery marked “the culmination of decades of intellectual effort by many people around the world” (Rolf-Dieter Heuer, CERN Director-General from 2009 to 2015) [CERN2013].

2.3 The High-Luminosity Large Hadron Collider

The High-Luminosity Large Hadron Collider (HL-LHC) is a proposed upgrade to the Large Hadron Collider (LHC) aimed to increase the LHC’s integrated luminosity of the machine providing a better chance to investigate on new physical processes. The LHC’s luminosity design value is $10^{34} \text{ cm}^{-2} \text{ s}^{-1}$, which gives a total integrated luminosity, i.e., total collisions created, of about 40 fb^{-1} per year. The main goal of the HiLumi project is to increase the integrated luminosity by a factor ten beyond the LHC’s design value [Apo2015]. Indeed, the higher the luminosity, the more data the experiments can gather to allow them to observe rare processes.

2.3.1 Luminosity

Luminosity is an important indicator of the performance of an accelerator: it is proportional to the number of collisions that occur in a given amount of time. The number of events generated in the LHC collisions is given by:

$$N_{\text{event}} = L_m \sigma_{\text{event}} \quad (2.1)$$

where L_m is the machine luminosity and σ_{event} represents the interaction cross-section for the event under study [Eva2008]. The machine luminosity is defined as the number of events per unit area and unit time [Rus2011], and is given by:

$$L_m = \frac{N_b^2 n_b f_{\text{rev}} \tilde{\gamma}_r}{4\pi \varepsilon_n \beta^*} F \quad (2.2)$$

where N_b is the number of particles per bunch, n_b the number of bunches per beam, f_{rev} the revolution frequency, $\tilde{\gamma}_r$ the relativistic gamma factor, ε_n the normalized transverse beam emittance, and β^* the beta function at the collision point. The factor F is the geometric luminosity reduction factor due to the crossing angle at the interaction point (IP):

$$F = \left(1 + \left(\frac{\theta_c \sigma_z}{2\sigma^*} \right)^2 \right)^{-\frac{1}{2}} \quad (2.3)$$

where θ_c is the full crossing angle at the interaction point, σ_z the RMS bunch length, and σ^* the transverse RMS beam size at the interaction point [Eva2008]. All the above expressions assume equal beam parameters for the two circulating beams [Rus2011].

2.3.2 Machine upgrade

The high luminosity configuration will require upgrades of existing equipment to face the ambition challenge of the High-Luminosity LHC. New equipment not included in LHC will be installed in HL-LHC and for certain systems a complete change of layout and performance will be carried out. New superconducting dipoles (11 T) and quadrupoles (MQXF) based on Nb₃Sn technology will replace the existing magnets and more compact superconducting RF grab cavities will be installed. Finally, new technology for beam collimation and long high-power superconducting links with zero energy dissipation will be introduced [Apo2015]. The HL-LHC should be operational by 2025 and it will permit to study in detail new particles observed at the LHC and exploit the full potential of the accelerator [CERN2015].

Chapter 3

Superconducting accelerator magnets and their protection

Particle accelerators are machines used to accelerate electrically charged particles to nearly light speed increasing their kinetic energy. In circular accelerator, superconducting magnets are required to produce a strong magnetic field with very high quality and control the particle beam trajectory during its orbital motion. Magnets of the LHC represent the state-of-the-art of superconducting accelerator magnet technology. LHC magnets operate at magnetic fields above 8 T. To obtain this magnetic field without losses, LHC magnets make use of superconducting cables and are cooled to a temperature of 1.9 K by using superfluid helium. In this context, the critical surface of the chosen superconductor material, which is the boundary between superconductivity and normal resistivity, represents one of the main parameters to consider during magnet design. However, the possibility of having a quench, i.e., an irreversible sudden loss of superconductivity, can never be fully excluded. A quench can cause a rapid heat and voltage generation in magnet windings and a pressure rise in the cryostat, until to lead to the destruction of the machine at worst. For this reason, magnet protection studies represent one of the most important and unavoidable steps during the design phase of a magnet.

3.1 Superconducting accelerator magnets

3.1.1 Particle accelerators and their physics

In high-energy physics, particle accelerators are machines that use electromagnetic fields to accelerate charged particles at high velocity and produce particle-particle collisions at high energy. Inside the accelerator, particles reach velocities near the speed of light and energies in the range of GeV or TeV before they are made to collide against each other at the experiments [CERN2012g]. From the high energy density localized in the collision, new particles merges. The energy density and temperature produced in the collisions at the LHC are similar to those that existed a few moments after the Big Bang. In this way physicists study how matter and ultimately our universe were formed. The maximum energy reached during the collisions depends on the sum of the two particle beams energies. The more energy obtained into these collisions, the more massive particles can come out of them. For this reason, the challenge becomes to build accelerators which are able to reach higher and higher level of energy. In addition to the beam energy, a key parameter is the luminosity. HL-LHC will increase the luminosity allowing to study rare physical processes not yet observed so far.

Physics behind LHC is that of a synchrotron, a cycling particle accelerator in which particles travel around a circular path several times to reach the desired energy [Fer2017]. LHC is the

largest synchrotron-type accelerator ever built. When a particle of charge q travels into a particle accelerator with velocity \mathbf{v} , its dynamic is ruled by the Lorentz force:

$$\mathbf{F}_L = q\mathbf{E} + q(\mathbf{v} \times \mathbf{B}) \quad (3.1)$$

where \mathbf{E} is the electric field, \mathbf{B} the magnetic field. The term $q\mathbf{E}$ is called the *electric force*, while the term $q(\mathbf{v} \times \mathbf{B})$ is the *magnetic force*. The electric force is mostly used to increase the particle energy while the magnetic force to guide particle beam along desired path [Wie2007]. The acceleration itself is obtained by means of the oscillations of electric field in the RF-cavities [CERN2012h], where the field oscillations are timed with great precision so that particles passing along the beam pipe feels the attraction of the approaching cavity and the repulsion of the just passed cavity. In the accelerator the magnetic field increases with time during process being synchronized to the increasing kinetic energy of the particles. Before the collision, at each turn particles gain momentum p_q whose magnitude is given by:

$$p_q = qrB \quad (3.2)$$

where r is the constant radius of curvature of the accelerator orbit [Fer2017]. The control of beam path is obtained by using magnetic fields: dipole field bends the particle beam and quadrupole field keeps it focused. The higher the particle momentum (or the beam energy), the higher the magnetic field needed to maintain the particles on the same orbit.

3.1.2 The LHC main magnets and their general features

The dipoles and quadrupoles in accelerators are typically several meters long and are characterized by a high magnetic field of several Tesla, high current densities and high stored energies (in the order of MJ/m) [Salmi2015c]. Typically, magnet consists of a curved saddle shape coil, shown in figure 3.1, in which the magnetic the magnetic field B is produced by a current I (or current density J).

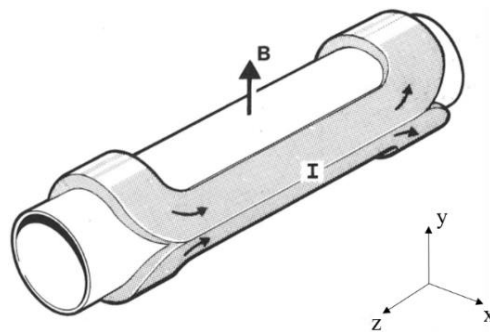


Figure 3.1: Curve saddle shape coil. The field B is perpendicular to the long dimension of the magnet. In the figure is also represented the current I flowing inside the coil [Wil1983].

In the LHC, dipoles produce the main vertical magnetic field, perpendicular to the particle direction and used to bend the particle beam along the circular trajectory, given by:

$$B_y = -\frac{\mu_0 J}{2} (r_{\text{out}} - r_{\text{in}}) \quad (3.3)$$

where $\mu_0 = 4\pi \cdot 10^{-7}$ Tm/A is a fundamental constant called the *vacuum permeability*, r_{out} is the coil inner radius and r_{in} the coil outer radius [Fer2017]. The x-component of the magnetic field B_x is null. In dipoles, the larger the magnetic field, the larger the energy. For this reason, in order to reach high energies is necessary to build dipoles with high fields or an accelerator with larger radius.

Quadrupoles focus and stabilize the beam. They create a magnetic field that is null in the center of the vacuum chamber and which increases linearly with the distance from the center of the quadrupole. Considering the generic coordinates x and y , the magnetic field B can be expressed in terms of the field gradient G as follows [Tod2012]:

$$\begin{cases} B_x = Gy \\ B_y = Gx \end{cases} \quad (3.4)$$

In quadrupoles, the larger the magnetic field, the larger the focusing strength. With reference to figure 3.1, the current density J is positive when flowing towards positive z [Wil1983]. The field lines for a dipole and a quadrupole are shown in figure 3.2.

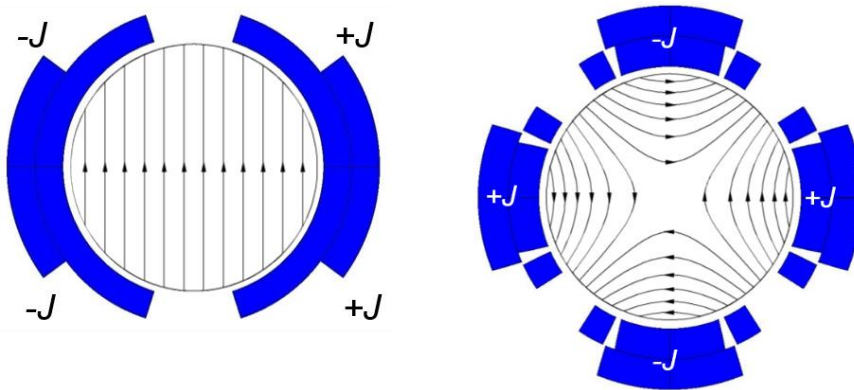


Figure 3.2: Magnetic field lines for a dipole (left) and a quadrupole (right). The magnetic field of dipole is constant over the space. The magnetic field of quadrupole is null in the center of the vacuum chamber and linearly dependent on the distance from the center of the quadrupole [Fer2017].

Finally, interaction region (IR) quadrupoles are used to reduce the beam size and increase the collision rate before the collision between the counter-circulating beams. Finally, higher order multiple magnets are used to further trim the beam and compensate field errors.

3.1.3 Superconducting materials in accelerator magnets

Superconductivity is a phenomenon whereby certain metals, when cooled down to very low temperature, allow electricity to pass through them without any resistance. The temperature at which the superconducting state appears is called the *critical temperature* T_c , that is a characteristic parameter of the specific metal. Below this temperature, the electrical resistance of a superconducting material drops to zero and the current flows inside the material without any dissipation of energy. Other two important parameter for superconductors are the critical magnetic field B_c and the critical current density J_c , above which superconductors lose their superconducting state. The critical current density depends on temperature and field, i.e., $J_c = J_c(T, B)$. These three parameters are interdependent and together form in (T, B, J) space the so-called *critical surface*, that is specific for each superconducting material [Mes1996]. The critical surfaces of Nb-Ti and Nb₃Sn are shown in figure 3.3. Superconductivity prevails everywhere below the critical surface, resistance everywhere above it.

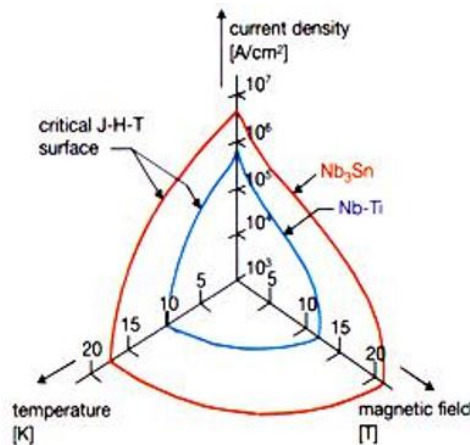


Figure 3.3: Critical surface of Nb-Ti and Nb₃Sn in (T, B, J) space. The operating volume of a superconducting material, where it has zero electrical resistivity, is enclosed by the T_c , B_{c2} and J_c lines [Eva2009].

Materials that work at temperature below 30 K are usually called *Low Temperature Superconductors* (LTS), while materials that have a transition temperature up to 138 K are referred as *High Temperature Superconductors* (HTS) [CESUR]. In addition to the property of complete lack of electrical resistance, superconductors are characterized by a perfect diamagnetism known as the *Meissner effect*. All practical materials used for accelerator magnets are compounds and so-called *Type II* hard superconductors. In these superconductors the transition from superconducting state to normal state does not occur abruptly, but gradually between the lower critical field B_{c1} and the upper critical field B_{c2} , through which the external field partially penetrates the conductor as resistive flux vortices [Salmi2015c].

Among all superconductors, the only two materials presently used for large scale magnet production are Nb-Ti and Nb₃Sn. Despite its upper critical field B_{c2} is only 10 T at 4.2 K, Nb-Ti is still used for magnet production because of its ductility which simplifies the fabrication

processes for wires and cables. Nb-Ti technology is used in magnets of moderate field strength (up to 6.25 T at 4.2 K). Nb₃Sn is used instead for higher fields with upper critical fields of about 20 T at 4.2 K [Mes1996]. One of the main changes for the LHC upgrade is the introduction of Nb₃Sn technology for the existing inner triplet magnets, in order to have high field performance beyond the capabilities of Nb-Ti cables.

3.1.4 Practical wires and cables for magnets

3.1.4.a LTS cables

Superconducting materials used in magnet windings are produced in wires and cables that are stable, which means they remain superconductive during the operation of magnet. The stabilization in LTS wires is obtained by inserting thin filaments of superconducting material into a stabilizer copper matrix to form a *multi-filament wire* or *strand* [Wil1983]. Copper matrix reduces temperature excursions by increasing the wire heat capacity and improving its thermal conductivity. In the context of magnet protection, it offers a low resistance path for the operation current in case of a quench. Wire diameter is typically in the order of 1 mm, while filament diameter is less than 50 μm [Salmi2015c]. Small filament diameter allows to reduce magnetic instabilities and field distortions caused by superconductor magnetization. Filaments are also twisted together to reduce interfilament coupling and AC losses [Fer2017]. Cross-sections of Nb-Ti and Nb₃Sn wires are shown in figure 3.4.

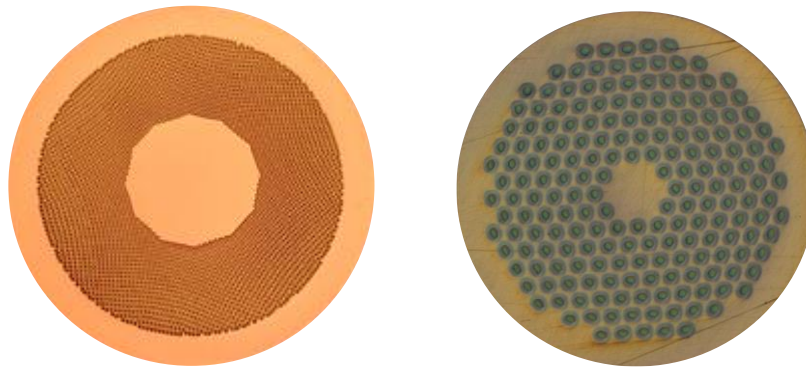


Figure 3.4: Cross-section of Nb-Ti [LUVATA] (left) and Nb₃Sn [Fer2017] (right) multi-filament wire.

Fabrication process of Nb₃Sn wires consists of different techniques, such as internal tin and powder in tube (PIT) process [Fer2017]. Components of wire (Cu, Nb, Sn) are stacked in 5-30 cm diameter billets, and the wire is made by using multi-step hot extrusion and drawing processes. Nb and Sn are subjected to several days of heat treatment in a range temperature of 650-700 °C in order to react together and form the Nb₃Sn superconducting material. Since the Nb₃Sn phase is brittle and sensitive to bending, cables are made from unreacted wire. Then, the coil composed by unreacted cable is put into the reaction oven. This procedure, also called *wind-and-react* method, is the most common in accelerator magnets [Salmi2015c]. The principal

difference with Nb-Ti fabrication process is that Nb-Ti superconducting phase is not brittle [Gree1992]. Superconducting cables are composed by several strands, and for this reason they are also called *multi-strand cables*. The most common cable used in accelerator magnets is the flat multi-strand two-layer Rutherford cable. These cables are keystoneed, i.e., pressed to a trapezoidal shape, in order to fit sectors coil geometry. Rutherford cables for accelerator magnets are typically made of round strands of Nb-Ti or Nb₃Sn. Cables are covered with an insulating layer, typically 0.1 mm thick, before the winding to permit the electrical insulation between the turns. Nb-Ti cables are insulated with Kapton, while pre-impregnated glass, e-glass, s-glass and ceramic insulation are used for Nb₃Sn cables [Imb2003a].

Main characteristics of a Rutherford cable are high current densities, very high packing factor, good stacking possibilities as well as mechanical stability [Will2009]. The present Nb₃Sn superconducting magnets are designed to operate at 80% of SSL, i.e., the short sample limit, which is the highest possible current reachable by the magnet. A schematic representation of a Rutherford cable is shown in figure 3.5, while a real cross-section of Nb₃Sn Rutherford-type cable used in superconducting magnets is shown in figure 3.6.

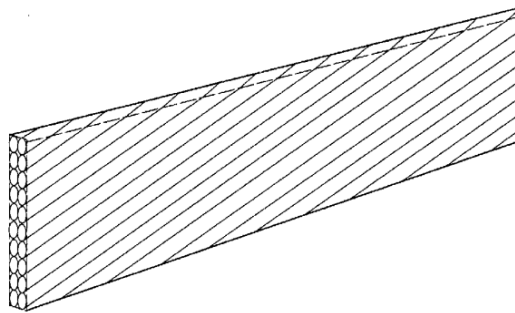


Figure 3.5: Schematic representation of a Rutherford cable [Dev2004].



Figure 3.6: Cross-section of keystoneed 40-strand (0.7 mm diameter) Nb₃Sn Rutherford cable with an 11 mm wide and 25 μm thick stainless-steel core [Fer2017].

3.1.4.b HTS cables

Nowadays, HTS cables represent the most promising technology for reach very high magnetic field. The most auspicious HTS materials presently are yttrium barium copper oxide (YBCO) and bismuth strontium calcium copper oxide (BSCCO). Figure 3.7 (b) shows a prototype Roebel cable for an HTS accelerator demonstration dipole magnet [CERN2014a]. The strips are made of stainless-steel and copper, except the last one which is an HTS tape (figure 3.7 (a)) [S-

POWER2015]. The advantage of using YBCO is the larger critical current density at low temperature, as shown in figure 3.8. However, HTS cables adoption for magnet applications is very challenging due to technical difficulties concerning their sensitivity to external magnetic field orientation, the slow transition to normal state in case of a quench, the high cost of fabrication and finally their shape [Gur2011].

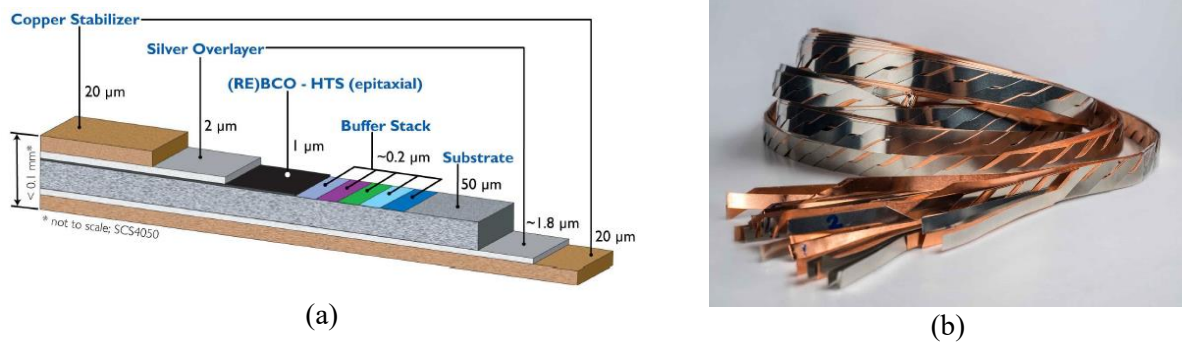


Figure 3.7: Structure of an YBCO tape [S-POWER2015] (a) and a prototype Roebel cable (b) to be used to wind a High Temperature Superconductor accelerator dipole [CERN2014a].

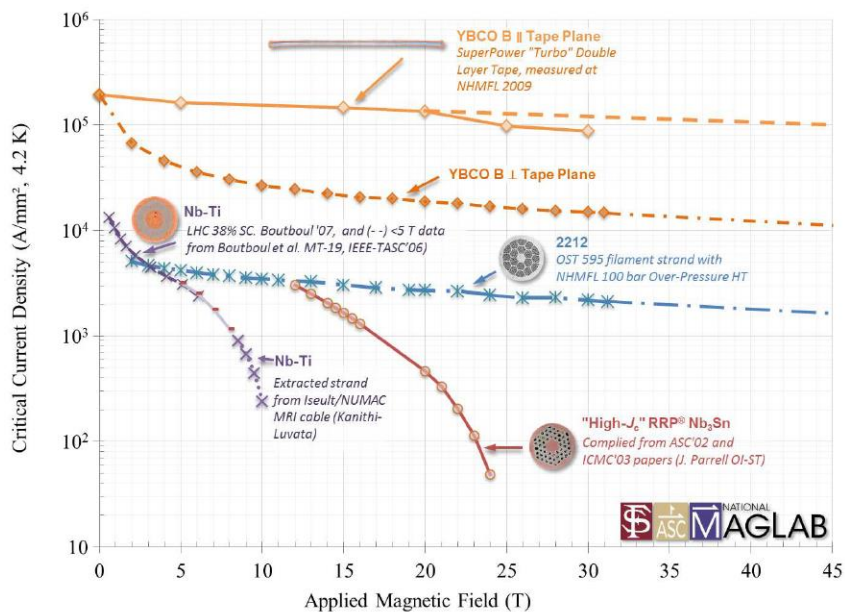


Figure 3.8: Critical current density vs. applied magnetic field in Nb-Ti, Nb₃Sn, Bi-2212 and YBCO at 4.2 K [Lee2014].

3.1.5 LHC dipole and quadrupole magnets

The LHC magnet system is composed by 1,232 main dipoles (MB) and 386 main quadrupoles (MQ) which are installed together with various types of magnets for insertion and correction [Rus2011]. The LHC main dipoles (MB) and main quadrupoles (MQ) guide the particle beam

inside the accelerator ring, while the interaction region quadrupoles MQXA and MQXB provide the final focus to the beam, just before the beam-beam collision [Eva2008].

The LHC main dipole and quadrupole magnets have two apertures in a common structure to house the two beam pipes for the two counter-circulating particle beams. This “two-in-one” concept consists of two and four superconducting coils for dipole and quadrupole respectively, which are arranged around the beam pipes and installed in a common structure called *cold mass*. The coils are surrounded by a containment structure composed by coil clamping elements, the collars, the iron yoke and the shrinking cylinder, which all contribute to the structural stability of cold mass assembly during the action of the electro-magnetic forces. The iron yoke contains also the bus bars which accommodates cables to power the magnets of the arcs that are connected in series. All the components inside the shrinking cylinder, which compose the cold mass, are cooled by superfluid helium and kept at 1.9 K during accelerator operation. Finally, the cold mass is inserted inside a cryostat whose main components are the radiation shield (at 4.5-20 K), the thermal shield (at 55-75 K), and a cylindrical wall called *vacuum vessel*. Typically, Nb₃Sn coils are epoxy-impregnated before the assembly procedure. All the components between the beam vacuum chamber walls and shrinking cylinder are immersed in superfluid helium at atmospheric pressure. The helium in the cold mass is cooled down to 1.9 K by two-phase low-pressure helium that circulates inside a heat-exchanger tube located in the upper part of the magnet cross-section [Eva2008]. The dipole and quadrupole cryostat cross-sections are respectively shown in figure 3.9 and figure 3.10.

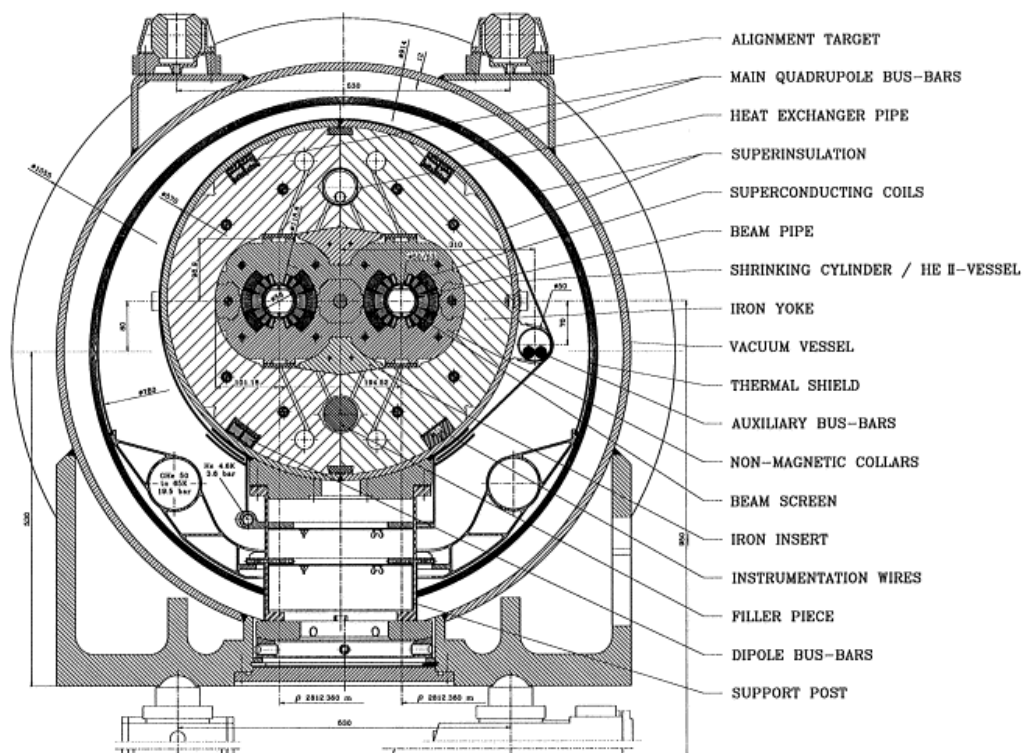


Figure 3.9: Cross-section of the LHC dipole cryostat, showing the two beam pipes, coils, collars and the iron yoke [Osw2011].

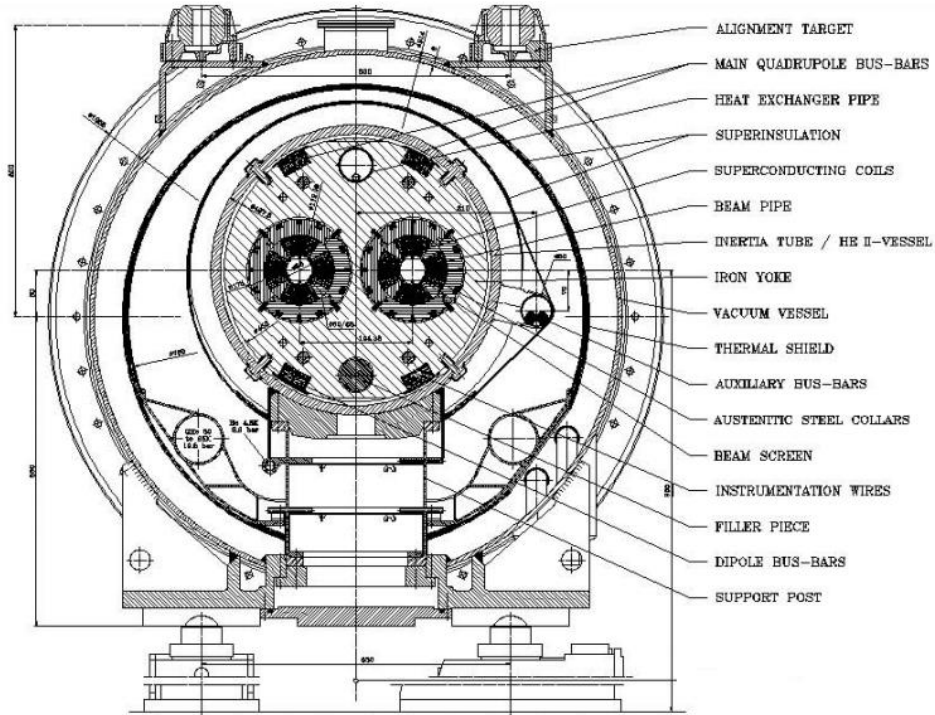


Figure 3.10: Cross-section of the LHC quadrupole [Eva2008].

To obtain a perfect field, a $\cos-\theta$ current density distribution around the bore for a dipole field and a $\cos-2\theta$ for a quadrupole field is required [Russ2011]. Figure 3.11 shows the field lines of an ideal dipole and quadrupole where the coil is a shell with constant thickness.

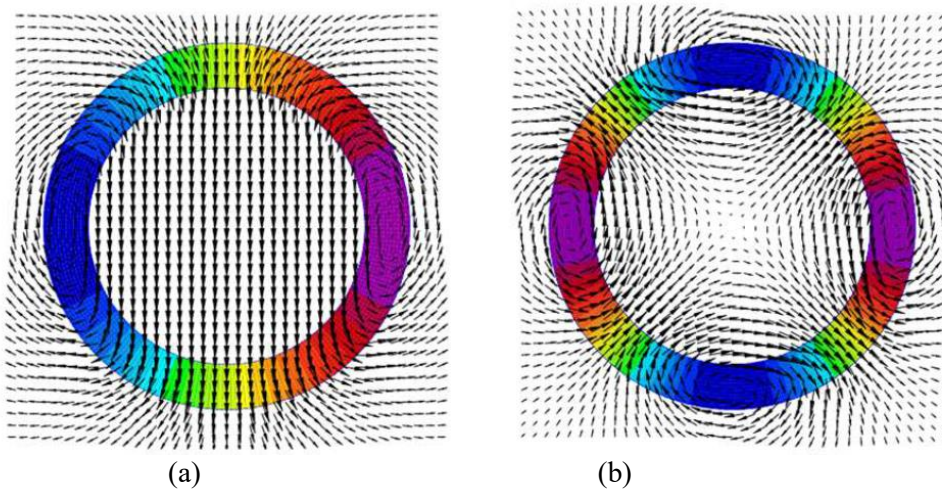


Figure 3.11: A cylindrical coil with $\cos-\theta$ (a) and $\cos-2\theta$ (b) current density distribution to create respectively perfect dipole and quadrupole fields [Russ2011].

Usually the coils have not a perfect cylindrical shape because the used cables are rectangular or trapezoidal. Coils present cables connected in series and they are subdivided in cable blocks separated by wedges. Coils in each aperture are arranged in two cable layers, that are the *outer layer* and the *inter layer*, shown in figure 3.12. In the LHC main dipoles and quadrupoles, keystoneed Rutherford cable are used. In particular, LHC dipole has a different cable on outer

and inner layer to obtain higher current density in the outer layer, where the magnetic field is lower, and facilitate the quench protection. The main quadrupoles are composed by the MB outer layer cable [Salmi2015c]. Figure 3.12 shows the cross-section of the LHC main dipole (a) and quadrupole (b). The magnetic field design and optimization is largely discussed in [Russ2011].

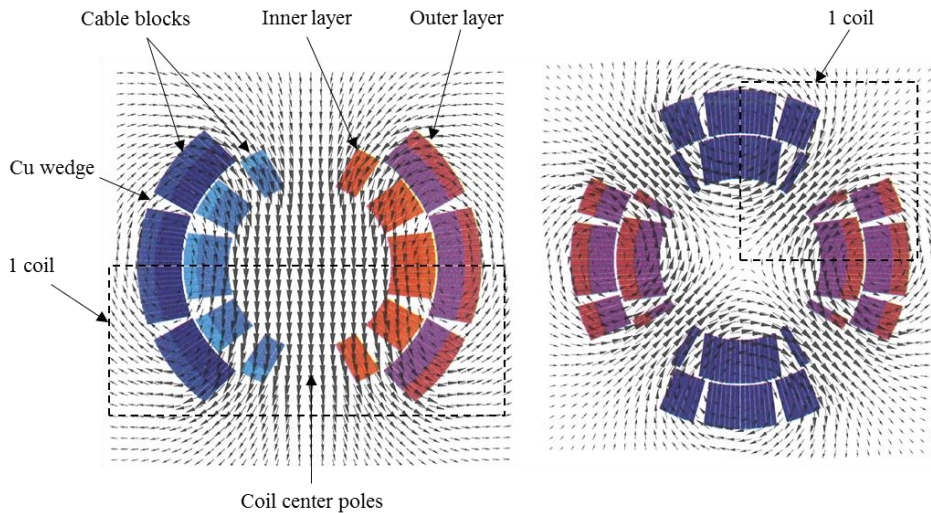


Figure 3.12: LHC dipole (a) and quadrupole (b) coils with two-layer sector coils made with keystoneed Rutherford cable [Russ2011].

The IR quadrupoles MQXA and MQXB, called also *low- β* quadrupoles, are instead single aperture magnets, which are arranged in a sequence to form the so-called *inner triplet*. Each inner triplet consists of three quadrupole optical elements and four magnets (Q1, Q2a, Q2b, Q3) [Bor2001]. The cross-section of MQXB magnet is shown in figure 3.13.

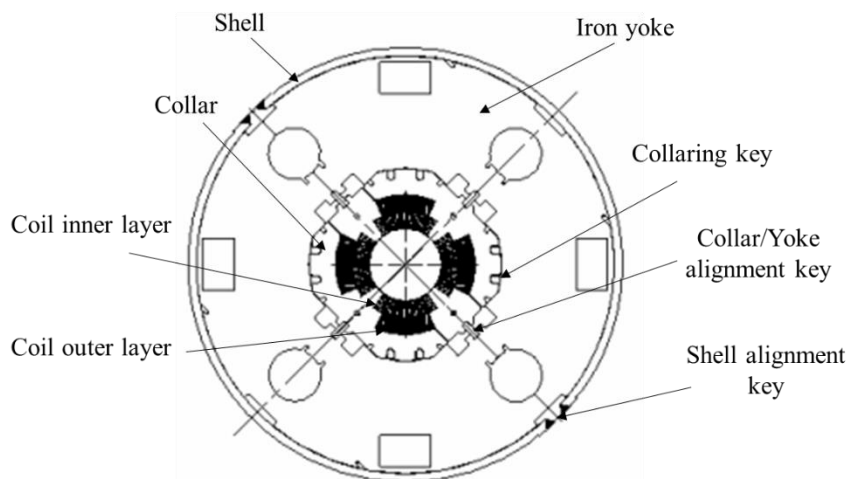


Figure 3.13: Cross-section of Nb-Ti quadrupole MQXFB of the LHC inner triplet [And2001].

3.1.6 Nb₃Sn magnets for HiLumi upgrade

As part of the HiLumi project, the existing inner triplet Nb-Ti quadrupoles will be replaced with new larger aperture Nb₃Sn magnets. The new quadrupoles, referred as QXF or MQXF, have been designed and fabricated in collaboration between CERN and the U.S. LARP. In addition, some of the present dipoles will be substituted with shorter Nb₃Sn dipoles having higher magnetic fields. These new dipoles, called 11 T dipoles, have been built in collaboration with CERN and Fermilab. The research exposed in this thesis focuses on MQXF quadrupole and 11 T dipole short models that are under development at CERN for the LHC luminosity upgrade.

3.6.1.a MQXF magnet

MQXF quadrupoles represent the high-luminosity upgrade of the actual inner triplet quadrupole magnets, referred as Q1, Q2a, Q2b, and Q3. The current LHC low- β quadrupoles use Nb-Ti superconducting coils to generate a gradient of 251 T/m in a 70 mm aperture. The magnetic length and the peak field are respectively 6.3 m and 7.7 T for Q1 and Q3 magnets, while 5.5 m and 8.67 T for Q2a and Q2b. The new low- β quadrupoles MQXF features an aperture of 150 mm and, making use of the Nb₃Sn superconducting technology, will generate at 1.9 K a gradient of 132.6 T/m and a conductor peak field of 11.4 T at a current of 16.47 kA. All MQXF magnets present the same cross-section design. Figure 3.14 shows a 2-D cross-section of MQXF quadrupole inclusive of a detailed description of the components.

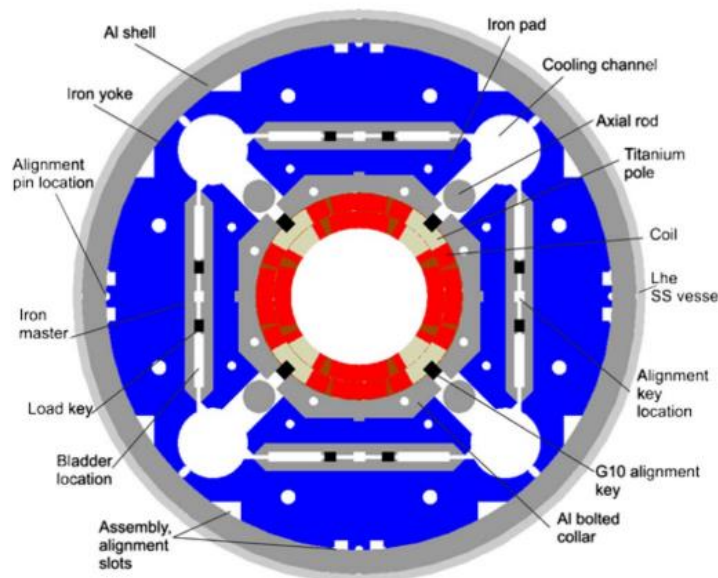


Figure 3.14: A 2-D cross-section of MQXF quadrupole of the HL-LHC inner triplet. [Boz2016].

It is planned to install two magnets, named MQXFA (4.2 m of magnetic length), connected together in one cold mass and cryostat for the Q1 and Q3 quadrupoles; while, one magnet named MQXFB, with a magnetic length of 7.15 m, will be installed in a single cold mass and cryostat for the Q2a and Q2b. A series of short models having 1.2 m of magnetic length, called

MQXFS, and of long prototypes, is presently being studied and fabricated both at CERN and at LARP [Fer2016].

The MQXF coils are composed by 50 turns wound in 2 layers around a Ti alloy pole and subdivided in 4 blocks per quadrant. Coils are made with a Nb₃Sn Rutherford-type cable composed by 40 strands of 0.85 mm. These cables have a Cu/non-Cu ratio of 1.2 and a non-Cu J_c at 4.2 K of 2450 A/mm² at 12 T [Fer2016]. The bare superconducting cable is 1.525 mm thick, 18.150 mm wide and has a keystone angle of 0.4°. The cable is insulated with a layer 145±5 µm thick of S2-glass under at a pressure of 5 MPa. Finally, the coils are inserted inside the containment structure composed by aluminium collars, iron pads, iron master keys, iron yoke, aluminium shells, stainless-steel LHe vessel and axial loading system [Fer2016]. The main strand specification and cable parameters are listed in table 3.1. The principal dimensional and operational parameters of the magnet are summarized in table 3.2. A detailed description of MQXF design, fabrication method and relevant analyses is provided in [Fer2016].

Table 3.1: Strand specification and cable parameters for MQXF magnet [Fer2016].

Parameter	Unit	Value
Strand diameter	[mm]	0.85
Cu/SC	[-]	1.2±0.1
RRR	[-]	>150
J_c (12 T, 4.2 K)	[A/mm ²]	>2450
Number of strands in cable	[-]	40
Cable bare width (before/after HT)	[mm]	18.150/18.363
Keystone angle	[deg.]	0.40
Pitch length	[mm]	109
Cable core width	[mm]	12
Cable core thickness	[µm]	25
Insulation thickness per side at 5 MPa	[µm]	145±5

Table 3.2: Coil and magnet parameters for MQXF magnet [Fer2016].

Parameter	Unit	Value
Coil aperture diameter	[mm]	150
Magnetic length (Q1-Q3)/(Q2)	[m]	4.20/7.15
Number of layers	[-]	2
Number of turns inner/outer layer	[-]	22/28
Operational temperature T_{op}	[K]	1.9
Operational gradient G_{op}	[T/m]	132.6
Operational current I_{op}	[kA]	16.47
Operational conductor peak field B_{op}	[T]	11.4
I_{op}/I_{ss} at 1.9 K	[%]	77
Stored energy density at I_{op}	[MJ/m]	1.17
Differential inductance at I_{op}	[mH/m]	8.21

3.1.6.b 11 T magnet

In the framework of LHC upgrade, new shorter Nb₃Sn dipoles (MBH), referred as 11 T, will replace some of the existing 8.33-T 15-m-long Nb-Ti LHC main dipoles (MB) in order to create space for additional collimators in the dispersion suppressor region of the LHC. The present proposal is the development of a 5.5 m twin-aperture 11 T dipole which is able to provide the same integrated strength (119 T·m) of previous MB dipoles at the operation current of 11.85 kA. The new layout consists in the replacement of one MB dipole with two of these magnets with a collimator in between [Zlo2015]. Figure 3.15 shows a 2-D cross-section of twin-aperture 11 T dipole inclusive of a detailed description of the components.

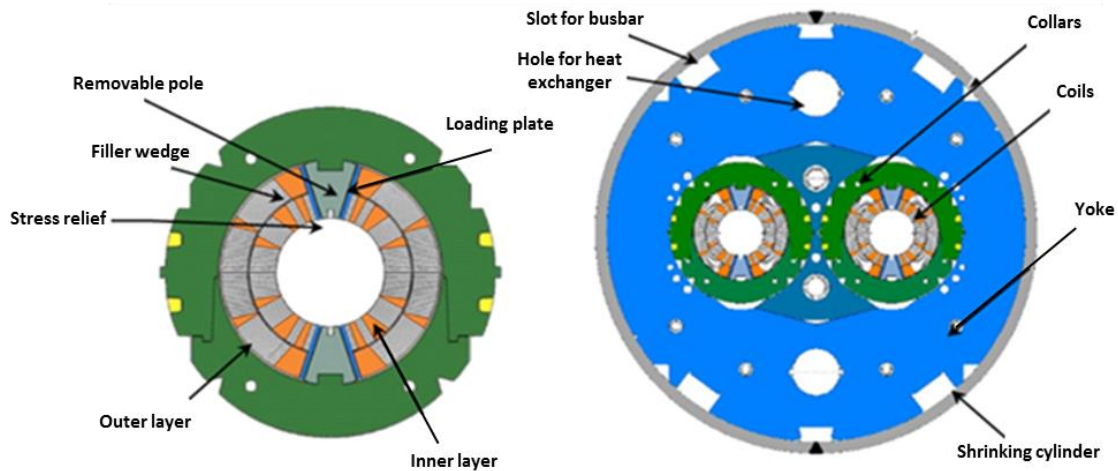


Figure 3.15: A 2-D cross-section of twin-aperture 11T dipole of the HL-LHC [Alo2015].

The 11 T coils consist of 56 turns wound in 2 layers around the pole and subdivided in six blocks per quadrant [Nil2017]. The magnet presents separate stainless-steel collars for each aperture and a MB yoke modified in the area of the collar yoke interface. The dipole is able to generate a dipole field of 11 T in a 60 mm aperture at an operation current of 11.85 kA. Coils are made with a Nb₃Sn Rutherford-type cable composed by 40 strands 0.70 mm in diameter [Zlo2015]. These cables have a Cu/non-Cu ratio of 1.1 and a non-Cu J_c at 4.2 K of 2750 A/mm² at 12 T. The bare superconducting cable is 1.25 mm thick, 14.847 mm wide and has a keystone angle of 0.79°. The cable insulating layer is in total 155 µm thick, and it is composed by a layer of S2-glass 75 and mica 75 and 80 µm thick, respectively. Finally, the coils are inserted in the cold mass. The main strand specification and cable parameters are listed in table 3.3. The principal dimensional and operational parameters of the magnet are reported in table 3.4. A detailed description of 11 T design, fabrication method and relevant analyses is provided in [Zlo2015].

Table 3.3: Strand specification and cable parameters for 11 T magnet [Zlo2015, Nil2017].

Parameter	Unit	Value
Strand diameter	[mm]	0.70
Cu/SC	[-]	1.15
RRR	[-]	>150
J_c	[A/mm ²]	2750
Number of strands in cable	[-]	40
Cable bare width (before/after HT)	[mm]	14.7/14.847
Keystone angle	[deg.]	0.79
Pitch length	[mm]	100
Cable core width	[mm]	12
Cable core thickness	[μ m]	25
Insulation thickness per side at 30 MPa	[mm]	0.1

Table 3.4: Coil and magnet parameters for 11 T magnet [Zlo2015, Nil2017].

Parameter	Unit	Value
Coil aperture diameter	[mm]	60
Magnetic length (short model/long model) at 1.9 K	[m]	1.6/5.3
Number of layers	[-]	2
Number of turns	[-]	56
Operational temperature T_{op}	[K]	1.9
Operational current I_{op}	[kA]	11.85
Operational conductor peak field B_{op}	[T]	11.76
I_{op}/I_{ss} at 1.9 K	[%]	0.79
Stored energy density at I_{op}	[MJ/m]	0.896
Differential inductance at I_{op}	[mH/m]	11.97

3.2 Quench protection in superconducting magnets

3.2.1 What is a quench?

In regular operating conditions, magnets operate below the superconductor critical surface without exhibiting resistive losses. Small disturbances can cause a local temperature (or magnetic field) increase in the coil and consequently a reduction of the cable critical current (I_c) below the magnet operation current (I_{mag}). When the critical surface is crossed, the excess current, i.e., the difference between I_{mag} and I_c , does not flow without resistance anymore and losses occur [Salmi2015c]. In this condition, the stabilizer matrix in the cable provides a lower resistance path to excess current and increases the heat capacity to absorb the generated heat. The phase in which the current is not transported only by the superconductor, but it is shared between the superconducting part and the copper stabilizer, is called *current sharing regime* and the conductor temperature at which it starts is the current sharing temperature T_{cs} . At the current

sharing temperature, the superconductor is in the transition phase from superconducting to normal state [Bar2013]. The switching to the normal resistive state generates somewhere in the coil a power dissipation by the Joule effect, which causes an overheating of interest portion and also of surrounding region by thermal diffusion along the conductor. If the Joule heating is sufficient and the cooling power is not enough to remove the generated heat, the temperature increases, and this effect propagates through the entire coil which transits to resistive, or normal conducting, state. This series of events is called a *quench* and *quench propagation* [Dev1992]. The current density in the copper matrix of Nb₃Sn cable can exceed 1 kA/mm² [Salmi2015c] and, if nothing is done to discharge the current in order to contrast the temperature rises, the coil may be damaged irreversibly.

Several factors can cause a quench. Some of these are internal causes, for example AC-losses during the magnet rump, magneto-thermal instabilities or conductor movements caused by high Lorenz forces, others are external disturbances such as beam losses or unexpected temperature increase in the coolant.

To avoid damage in the magnet, the energy stored in the magnetic field after a quench must be safely dissipated; in addition, magnet temperature and voltage must be limited in a safety range. Once the quench is detected, the current supply is switched off in order to obtain as fast as possible current decay. Another way to discharge the magnet energy is through an external dump resistor or internally into the windings [Salmi2015c].

3.2.2 Quench detection and current supply disconnection

The detection of a quench during magnet operation has to take place as fast as possible using dedicated instrumentations. The criterion used to detect a quench in accelerator magnets is based on the measuring of the voltage rise associated to the resistive zone in the cable. Magnets are instrumented with a series of voltage taps along their winding. A balanced bridge circuit compares the voltage over at least two segments of the magnet. The inductive voltage is the same on both sides of the bridge, so the discrepancy is associated with a resistive voltage on either side. The quench protection system is activated when the resistive voltage becomes higher than a voltage detection threshold U_{th} and stays above it for a certain time called *validation time*. The U_{th} in LHC quadrupoles and dipoles is 100 mV, with a validation time of 10 ms used to avoid false signals [Brü2015]. The time delay elapsing between the quench onset and the reaching of the threshold voltage is called *detection time* and it depends on the magnet operation conditions. For example, during the LHC dipole commissioning [Ver2008] a detection time of about 20 ms was measured near the maximum operation current.

After the quench detection, the beam is safely aborted and immediately the current supply is disconnected. The current starts to decay in the magnet circuit according to this formula:

$$I(t) = I_0 e^{-t/\tau_e} \quad (3.5)$$

where τ_e is a time constant, called also *characteristic extraction time*, defined as the ratio between the total inductance and the total resistance in the circuit [Fer2015].

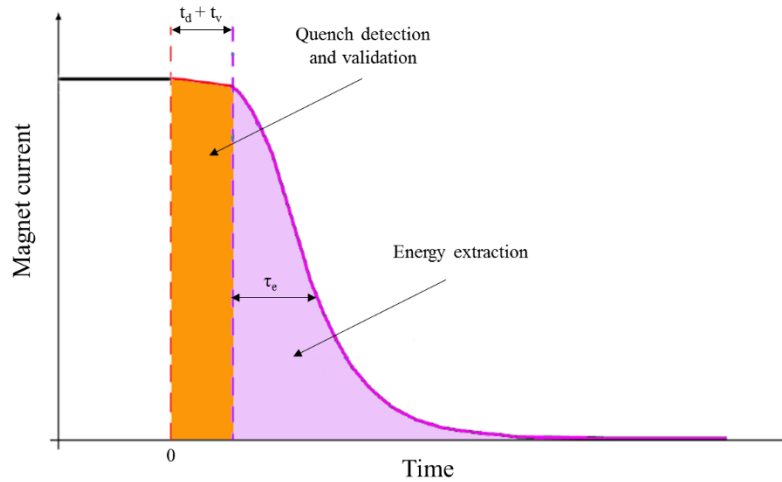


Figure 3.16: Current decay profile during a quench in a magnet [Mar].

3.2.3 Temperature rise and MIITs

During a quench, the heat generation in the quenched region of the coil is principally caused by the operation current which flows in the resistive matrix metal of the superconducting cable. Clearly, the peak temperature location is the zone of the coil in which the quench starts, the so-called *hot spot*. To protect the magnet during a quench, it is important to maintain the peak temperature under a suitable level. For this reason, among parameters involved during the quench propagation, the peak temperature is the most critical one. In order to relate the current decay profile after a quench to the peak temperature, the so-called MIITs notion is used [Tod2013].

If we assumed local adiabatic conditions, all the volumetric heat generated by the Joule effect in the cable cross-section is absorbed in the cable thermal mass and the temperature rise dT during time dt is:

$$J(t)^2 \rho(B, T) dt = \gamma c_p(T) dT \quad (3.6)$$

where J (in A/m^2) is the current density in the cable cross-section, ρ (in $\Omega \cdot m$) the electrical resistivity, γ (in kg/m^3) and c_p (in $J/(kg \cdot K)$) respectively the mass density and the specific heat of the cable.

If we consider that all the current flows in the copper, we can calculate the average power density in the cable cross-section as follows:

$$J(t)^2 \rho(T) = J_{\text{Cu}}(t)^2 \rho_{\text{Cu}}(T) \lambda_{\text{Cu}} = \frac{I_{\text{mag}}(t)^2}{\lambda_{\text{Cu}}^2 A_{\text{cable}}^2} \rho_{\text{Cu}}(B, T) \lambda_{\text{Cu}} \quad (3.7)$$

where J_{Cu} is the current density flowing in the copper, ρ_{Cu} the resistivity of copper, λ_{Cu} the cable copper fraction, I_{mag} the magnet current and A_{cable} the cross-sectional area of the cable. This assumption could be considered valid because the resistivity of copper is about two orders of magnitude lower than the resistivity of a superconductor in normal state.

Combining the equations (3.6) and (3.7) and integrating after rearranging, the squared current decay integral is obtained:

$$\int_0^\infty I_{\text{mag}}(t)^2 dt = \int_{T_{\text{op}}}^{T_{\text{max}}} \lambda_{\text{Cu}} A_{\text{cable}}^2 \frac{\gamma c_p(T)}{\rho_{\text{Cu}}(B, T)} dT \quad (3.8)$$

where T_{max} is the maximum acceptable temperature in the cable and T_{op} the operation temperature. The term on the left of equation (3.8) is called the *quench load*, and when it is scaled with a factor 10^{-6} , its unit is called *MIITs*. The left-hand side of equation (3.8) depends only on the response of the circuit, while the right-hand side is a property of materials in the cable. The quench load is an important parameter that permits to relate the current decay profile after a quench to the hot spot temperature [Salmi2015c].

3.2.4 Quench protection strategies

3.2.4.a External dump resistor

One of the possible strategies to extract part of the energy in the quenching magnet is the use of an external dump resistor. The energy dissipated in the dump resistor, E_{dump} , is given by:

$$E_{\text{dump}} = R_{\text{dump}} \int_0^\infty I_{\text{mag}}^2(t) dt \quad (3.9)$$

where R_{dump} is the resistance of dump resistor which is switched in series with the magnet after the current supply disconnection. The larger is this resistance, the faster is the current decay. In practice, R_{dump} is limited by the maximum magnet voltage that is in the order of 1 kV [Tod2013], so for magnet current of 10 kA the dump resistance value is 100 m Ω . The maximum dump resistor is independent of the magnet length, but it depends only on the magnet current. For this reason, relatively small fraction of the energy can be extracted in long magnet. The advantages in using external resistor are the prompt availability and the fast recovery of the operation temperature after the quench due the limited energy dumped in the helium.

3.2.4.b Quench protection heaters

In case of a quench in long magnets, only a small part of the stored energy can be extracted from the magnet system. The remaining part of energy is absorbed by the magnet itself. Since the quench propagation is not so fast (of the order of 1 s for a 10-m-long magnet [Tod2013]), quench protection heaters are used to induce a fast (of the order of 10-50 ms [Tod2013]) suppression of the superconducting state over a large fraction of the coil. Consequently, a larger portion of the coil becomes resistive, absorbing the stored energy and avoiding local damage in the windings. The magnet current decay turns out to be faster, i.e. lower MITs, and, as a consequence, hotspot temperature decreases.

The protection heaters are resistive strips powered with a capacitor bank and placed in contact with cables. An important design parameter is the heater power density (in W/cm²), P_{QH} , computed under adiabatic conditions as follows [Izq2016]:

$$P_{QH}(t) = \frac{R_{QH}I_{QH}(t)^2}{w_{QH}l_{QH}} = \frac{I_{QH}(t)^2\rho_{SS}}{w_{QH}^2d_{QH}} = \frac{\rho_{SS}I_{QH_0}^2e^{-2t/\tau}}{w_{QH}^2d_{QH}} \quad (3.10)$$

where R_{QH} is the heater strip resistance, $I_{QH}(t) = I_{QH_0}e^{-t/\tau}$ the current flowing in the heater, i.e., the heater current decay, w_{QH} the heater width, d_{QH} the heater thickness, l_{QH} the total length of the heater station, and ρ_{SS} the stainless-steel resistivity. The time constant of the heater pulse $\tau = RC$ is given by the product between the heater circuit resistance R , which is the sum of the heater strip resistance R_{QH} and the wiring resistance R_w , and the capacitance C of the heater power supply. The electrical insulation between heaters and coils is provided by a thin layer of polyimide.

The heater efficiency is determined by the quench heater delay, which is the time needed by the heaters to start a quench somewhere in the coil, typically in the high-field zone [Tod2013]. In other words, the heater delay is the time delay between the heater activation and consequent induced normal zone initiation in the coil. The delay depends on many parameters [Salmi2015c], such as the cable characteristics and energy margin to quench as well as heater heating power, heater layout and insulation scheme. In addition, another important parameter is the fraction of windings that the heaters can quench. Indeed, it is not possible to cover the entire coil surface with heaters because of voltage limits and difficulties in placing the heaters in some parts of the coil, especially in the inner surfaces. Different heater configurations are widely discussed in [Salmi2015c].

3.2.5 Heater designs

3.2.5.a Copper plated heaters in the LHC

In the LHC magnets, the quench protection heaters are typically made of stainless-steel strips in contact with the cables. Strips can be periodical plated with copper to reduce their resistance

and ensure enough heating power to the entire heating station. Quenches are assumed to start under heating stations and then the entire coil passes to the normal state by natural quench propagation. The stainless-steel heater strips are 15 mm wide and 25 μm thick, and they are sandwiched between two 75 μm layers of polyimide which electrically isolates heaters from the coil.

3.2.5.b Heaters in Nb_3Sn Magnets

In Nb_3Sn magnets, several stainless-steel and copper plated heater designs are developed. In this case heaters are mounted after the coil heat treatment because their polyimide-based insulation is not able to resist to the heat treatment of the coil. Consequently, the heaters must be placed only on the inner layer (IL) and the outer layer (OL). An issue is the detachment of inner layer heaters over time, probably because IL heaters have not a support on the bore side and they are in direct contact with superfluid helium [Amb2011]. Finally, a configuration in which heaters are placed in the gap between the layers, i.e. the inter layer (InL), has been studied for new magnets.

Heater strips are connected in the magnet in four circuits, which consist of four heaters connected in parallel and powered by a capacitor bank called Heater Firing Unit (HFU). Each circuit included a strip at each coil to ensure coverage at each coil in case of an HFU failure [Salmi2015c].

3.2.5.c Heaters in MQXFS magnet

In MQXFS quadrupole magnet, each coil is equipped impregnated stainless-steel and copper plated heater strips, four placed on the outer layer and two in the inner layer. Heater strips are connected in series and lead to twelve heater circuits per magnet. MQXFS heaters are composed by a layer of stainless-steel strips 25 μm thick plated with a layer of copper 10 μm thick, in order to reduce the overall strip resistance and limit the heater voltage for long magnets. Heaters are bonded to a 50 μm layer of polyimide, making the so-called *trace*. The trace is installed in the outer and inner layer reacted and is covered by a layer of S2-glass insulation 150 μm thick before coil impregnation. Finally, heater powering wires are soldered directly to the heater strips [Izq2018]. A schematic view of the cable, trace and coil insulation is reported in Figure 3.17.

Key parameters in heater design are temperature and maximum voltage from heater to coil, whose maximum allowed values for MQXF heaters are respectively 350 K and ± 450 V. Heaters are powered with a power density of 150-200 W/cm^2 in order to minimize the quench heater delay. For the same goal, polyimide insulation between heater and the coil was minimized to 50 μm . The outer layer heating stations are 40 mm long, 19.5 mm wide, and separated by 120 mm sections with 10 μm copper cladding. The inner layer is instead characterized by a wavy shape with heating station 25 mm long and 20.2 mm wide, which provide partial coverage to several turns [Fer2016]. A detailed description of the design and fabrication as well as quench heater performance analyses for MQXF quench heaters is reported in [Izq2018].

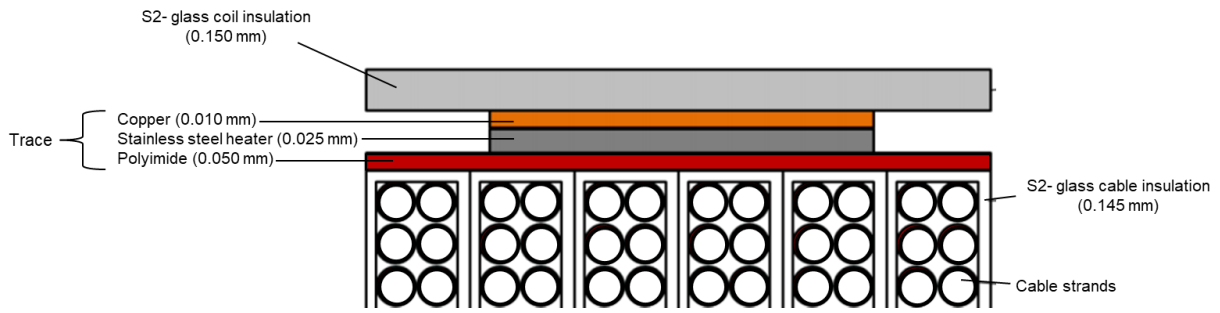


Figure 3.17: A schematic view of the cable, trace and coil insulation for MQXFS magnet [Izq2017].

A real image of the outer layer and inner layer protection heaters is shown in figure 3.18. The layout of MQXFS quench heaters for the outer layer and inner layer, as well as their location in the coil, is shown in figure 3.19. Tables 3.5-3.6 report and compare, respectively for outer layer and inner layer, the actual quench heater powering parameters for the short MQXF models and the nominal quench heater parameters for the inner triplet quadrupole magnets in the LHC.



Figure 3.18: Outer layer (a) and inner layer (b) protection heaters [Edd2017].

Table 3.5: Outer layer quench heater circuit powering parameters for MQXFS magnets and the inner triplet quadrupole magnets in LHC [Izq2018], [RepMQXFS5].

MQXF magnet ID		Outer Layer				
		S1	S3	S5	Q1/3	Q2a/b
Voltage	[V]	331	900	900	760	900
Capacitance	[mF]	19.2	7.05	7.05	7.05	7.05
Peak current	[A]	196	150	198	198	198
Total resistance heater circuit	[Ω]	1.69	6.0	4.5	2.9	4.6
RC	[ms]	32	42	32	20	32
Peak power density	[W/cm ²]	209	123	213	213	213
Energy density in the HS	[J/cm ²]	3.39	2.59	3.42	2.16	3.42

Table 3.6: Inner layer quench heater circuit powering parameters for MQXFS magnets and the inner triplet quadrupole magnets in LHC [Izq2018], [RepMQXFS5].

MQXF magnet ID		Inner Layer				
		S1	S3	S5*	Q1/3	Q2a/b
Voltage	[V]	331	900	-	565	900
Capacitance	[mF]	19.2	7.05	-	7.05	7.05
Peak current	[A]	133	150	-	134	134
Total resistance heater circuit	[Ω]	2.48	6.00	-	4.2	6.7
RC	[ms]	48	42	-	30	47
Peak power density	[W/cm ²]	97	123	-	98	98
Energy density in the HS	[J/cm ²]	2.31	2.59	-	1.45	2.32

*Inner layer quench heaters have not been powered in MQXFS5 with the aim to study the impact of powering the heaters on the bubbles formed in the inner diameter of the coils (observed in MQXFS1 and MQXFS3)

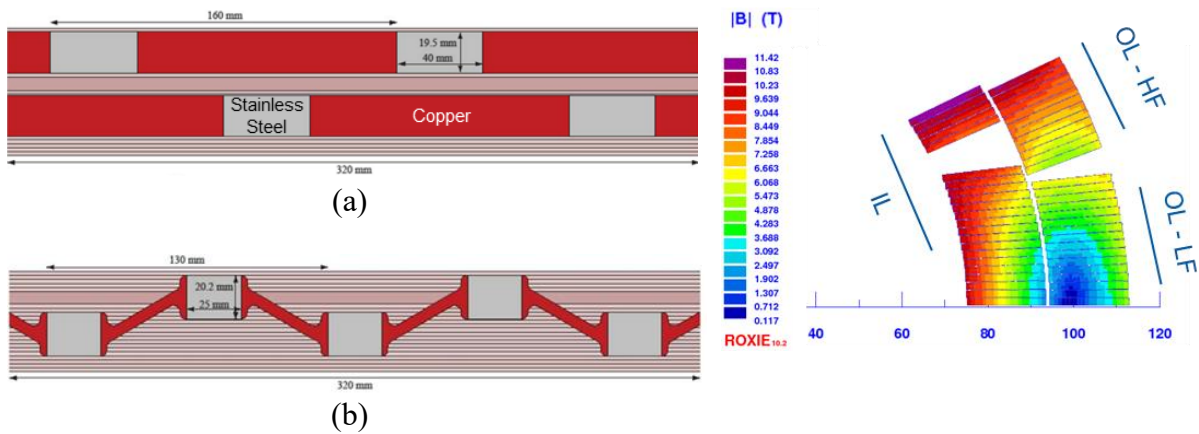


Figure 3.19: Outer layer quench heater layout (a) and inner layer quench heater layout (b) for MQXFS magnet. Location of the heaters in the coil (right) [Izq2017].

3.2.5.d Heater design in 11 T magnet

In the 11 T dipole magnet, heaters are placed only in the outer layer coil. Heaters are made of stainless-steel strips 25 μm thick and are embedded in a Kapton foil which is glued on the outer layer surface after the impregnation. Heaters are also plated with 5 μm of copper for part of length. The insulation between heater and coil consists of layer 50 μm thick of Kapton. In first short models a layer of S2-glass (0.2 mm) was installed between the heater and the insulated conductor prior to impregnation [Izq2016]. The amount of S2-glass insulation between heater and coil plays a key role on the time to initiate a quench, for this reason this layer was removed in last magnet versions by impregnating the heater directly with the coil during the manufacturing process [Izq2018a].

Each 11T quench heater circuit is composed by two strips in series powered by a 900 V, 7.05 mF power supply. Each coil contains two quench heater circuits, leading to sixteen circuits per dipole full assembly. The heating station is 50 mm length and the distance in between stations is 130 mm in the high field block and 90 mm in the low field zone. The width of the

heaters was defined to maximize the heater coverage surface in the coil; the width of the high field quench heater is 24 mm, while 19 mm for the low field quench heater to quench faster the low field zone and permit a uniform power dissipation in the coil cross-section [Izq2016, Izq2018a].

In MBHSP106 magnet, in addition to outer layer heaters, for the first time additional heaters were put in the inter layer (InL), i.e. the space between outer layer and inner layer of the coil [RepMBHSP106]. The idea was to install heaters in the inter layer to quench quickly the outer layer and inner layer cables and allow the transition to normal state for a larger fraction of the coil. The stainless-steel strips are insulated from the insulated cable by one layer of mica (FIROX[®] 80P34A) and two layers of S2-glass (11 TEX 636). The total thickness of the heaters, including insulation, is 0.5 mm. Inter layer quench heater strips have different values of width: 5 mm for InL-HF strip, 12.9 mm for InL-MF strip and 11.4 mm for the InL-LF strip. The InL-HF (Block 3 or B3) and InL-LF (Block 1 or B1) strips are connected in parallel, and in turn they are connected in series with the InL-MF strip (Block 2 or B2). Figure 3.20 shows the outer layer and inter layer quench heaters layout and their position in the coil. Figure 3.21 shows the inter layer quench heater layout and the assembly of the heaters in the coil during winding procedure. Quench heater circuit powering parameters for MBHSP106 magnet are reported in tables 3.7-3.8.

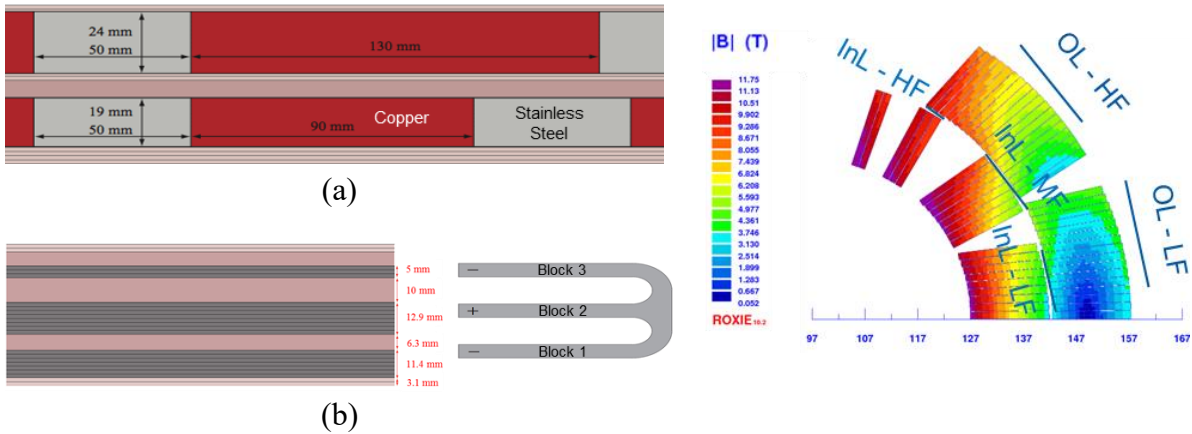


Figure 3.20: Outer layer quench heater layout (a) and inner layer quench heater layout (b) for MBHSP106 magnet. Location of the heaters in the coil (right) [Izq2018a].

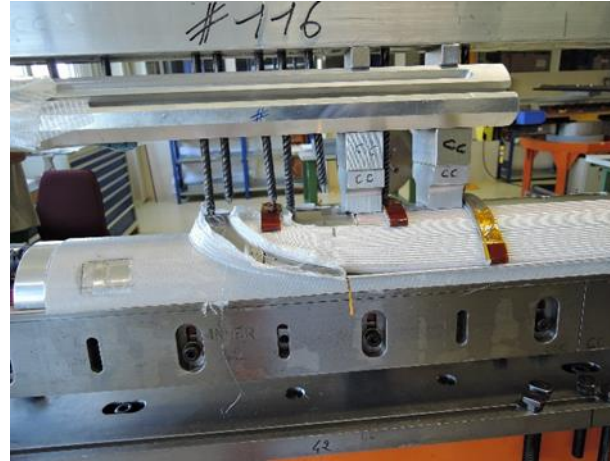
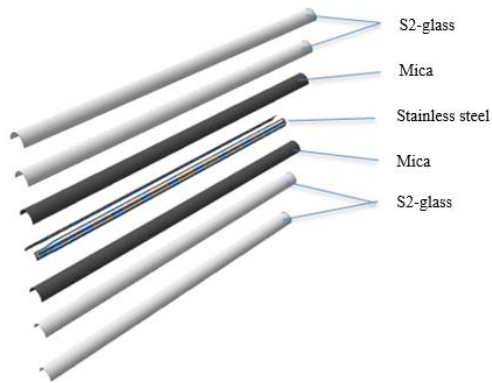


Figure 3.21: Inter layer quench heater layout (left) and assembly of the heaters in the coil during winding (right) [RepMBHSP106].

Table 3.7: Outer layer quench heater parameters for MBHSP106 magnet [RepMBHSP106].

		Outer layer heaters HF	Outer layer heaters LF
Voltage	[V]	900	900
Capacitance	[mF]	7.05	7.05
Peak current	[A]	150	150
Total resistance heater circuit	[Ω]	6	6
RC	[ms]	42	42
Peak power density	[W/cm ²]	85	136
Energy density in the HS	[J/cm ²]	1.8	2.9

Table 3.8: Inter layer quench heater actual parameters for MBHSP106 magnet [RepMBHSP106].

		Inter layer heaters
Voltage	[V]	900
Capacitance	[mF]	7.05
Peak current (B1/B2/B3)	[A]	61/88/27
Total resistance heater circuit	[Ω]	5
RC	[ms]	36
Peak power density (B1/B2/B3)	[W/cm ²]	62/101/62
Energy density in the HS (B1/B2/B3)	[J/cm ²]	1.1/1.8/1.1

Chapter 4

Quench protection heater numerical simulation

In magnet quench protection design, experiments and simulations are both used and needed. Simulations represent a faster and cheaper simplification of the real experiments and permit to estimate the impact of parameters that are not accessible experimentally. On the other hand, experiments are needed to validate simulation results and to guide the future modelling.

In this thesis, quench heater delay simulations for MQXF and 11 T magnet short models are presented. Simulations are inspired on a heater-coil adiabatic thermal model developed at CERN by J. Rysti, which allows to simulate the heater delay under different operational conditions. Thermal simulations were carried-out in COMSOL Multiphysics[®], while magnetic field maps of coil used were imported by ROXIE, a software for electromagnetic simulations created by S. Russenschuck at CERN. Results from simulations were compared with heater delay measurements performed by G. Willering at CERN SM18 magnet test facility.

4.1 Quench heater delay: from experimental procedure to numerical thermal model

4.1.1 Quench heater delay experimental procedure

The main goal of experiments is to measure the heater delay for different current levels and for power density and energy density representative to LHC machine conditions. The experimental procedure, of which a representation is shown in Figure 4.1, consists in measuring the time delay between the heater activation and quench initiation in the coil. The magnet is ramped at a specific current level, then one or more heaters are manually activated, while other heaters are protecting the magnet. The magnet current is maintained constant until the quench provoked by the heater propagates and is detected by the quench detection circuit. Then, the rest of the heaters are fired, and energy is extracted to minimize cryogenic recovery time.

In the experiments, the heater delay is defined from the recorded voltage tap signals. The criterion for the quench onset definition is the time instant when the resistive voltage signal starts to rise above the noise level prior the heater activation and keeps rising. Figure 4.2 shows real voltage signals from MBHSP106 magnet cold test for several coil turns.

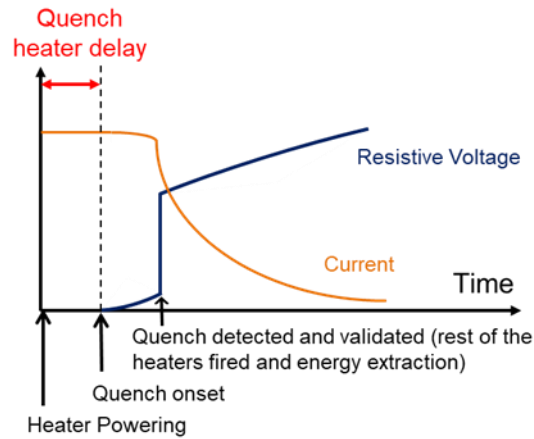


Figure 4.1: Representation of the experimental procedure to measure the quench heater delay [Izq2017].

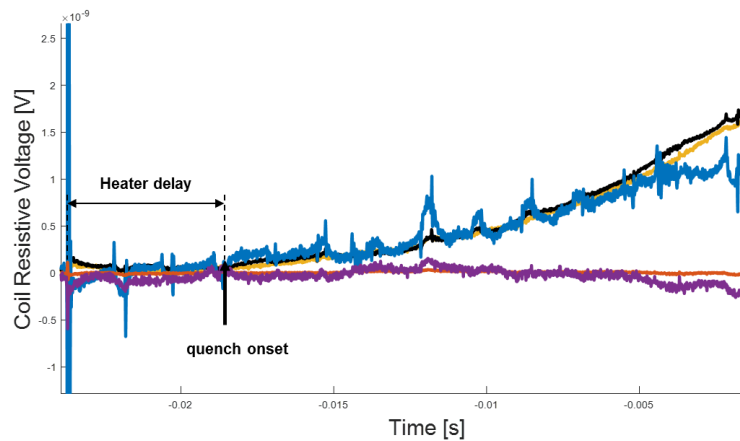


Figure 4.2: Real coil resistive voltage signals from tests on MBHSP106 magnet.

4.1.2 Domain modelling

In quench protection the goal of the heater is to increase the coil temperature above the critical temperature of the used superconductor to quench the whole coil. The logic inside the presented thermal model is to numerically simulate the heater powering and the heat transfer from the heater to the superconducting coil, and then compare the cable temperature with its critical surface to evaluate the time needed to provoke the normal zone initiation in the coil, i.e. heater delay. A scheme of protection heater circuit (heaters and dump resistor) showing the heater connection is represented in figure 4.3. A dump resistor was used in magnets presented in this chapter.

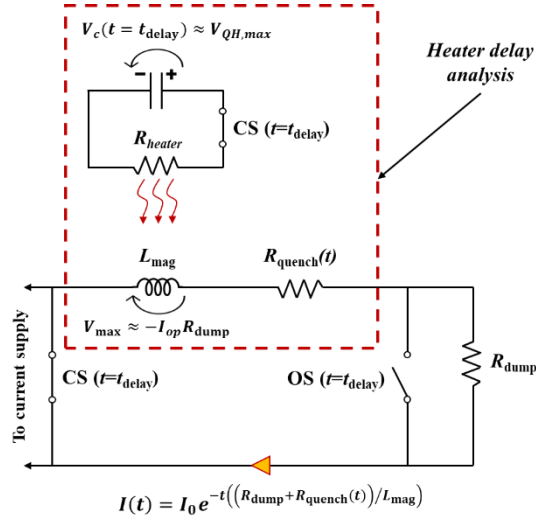


Figure 4.3: A scheme of protection heater circuit [Salmi2015c].

Heater warms up the coil and switches it to the normal state increasing its resistance. The t_{delay} is the time instant when the quench is detected by the instrumentations, i.e., the delay time between quench initiation and protection activation, and the switches opened (OS) or closed (CS). When a quench is detected, the switch of magnet electrical power circuit is opened and the current is forced to flow through the resistor R_{dump} . The current in the magnets starts to decrease as follows:

$$I(t) = I_0 e^{-t(R_{\text{dump}} + R_{\text{quench}}(t))/L_{\text{mag}}} \quad (4.1)$$

where $R_{\text{quench}}(t)$ is the total resistance of the normal zone and L_{mag} magnet inductance. The heater delay analysis in this thesis focuses on the dotted red area in indicated in figure 4.3.

Figure 4.4 shows the schematic view of a generic quench heater on the coil surface. The heater geometry is expressed in terms of periodical heater coverage at different turns. The modelling domain inclusive of a detailed description of input parameters, assigned materials and border conditions is shown in figure 4.5.

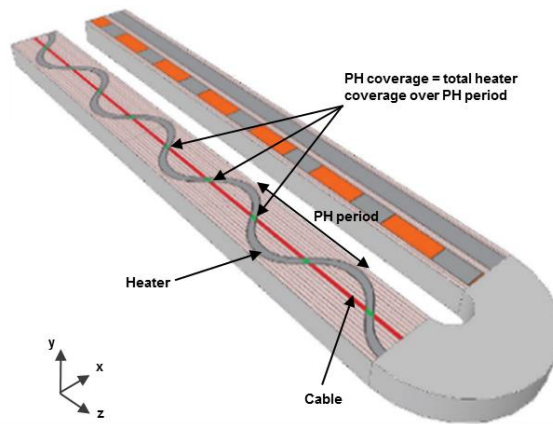


Figure 4.4: Schematic view of the heater on the coil surface [Salmi2014].

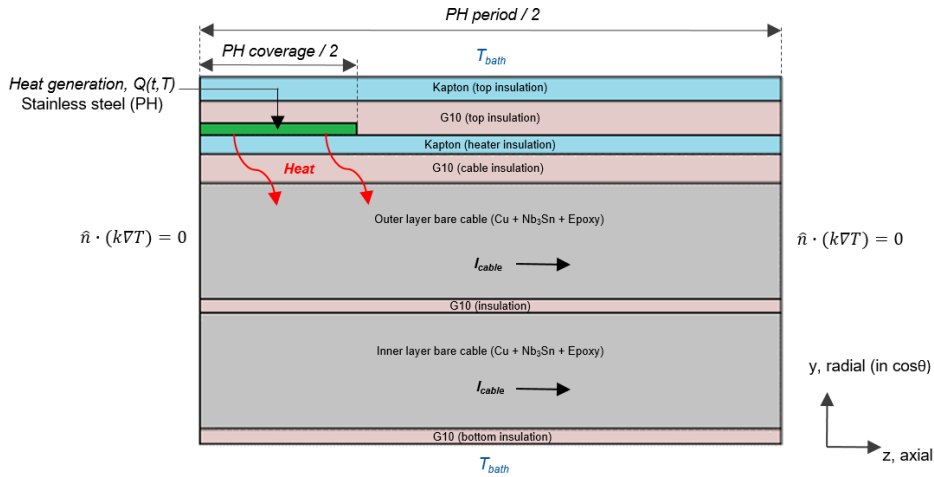


Figure 4.5: 2-D thermal model for half period of the protection heater geometry. Not in scale [Salmi2014].

The geometry of the thermal model was totally coded in COMSOL. It consists of thin layers of materials with very different thermal conductivities which require fine discretization for an accurate numerical solution. The symmetry of the periodical geometry of the heater permits to reduce the modelling to one period (PH_{period}), and it turns out that if the period is symmetric at its center, it is possible to reduce further the computational domain to half of the period ($PH_{\text{period}}/2$). This strategy permits to save computational time. Finally, as commonly done in quench simulation codes, strands were not modeled and homogeneous material properties were considered for the bare cables.

We also assumed that cooling provided by helium can be considered neglected in an impregnated winding to reduce the thermal model to heat generation in the quench heater and heat diffusion to the cable. Furthermore, the heat transfer between coil turns is neglected since we assumed that the adjacent turns are enough uniformly warmed up. Magnetic field and current distribution are assumed uniform in the cable by default. The model permits also simulating variable magnetic field profile across the cable. In this case, the current sharing temperature varies along the cable, and the average field is used to compute material thermal properties.

A quench occurs when in simulation the cable temperature exceeds $T_{\text{cs}}(I, B)$. The criterion used to determine the quench heater delay is the monitoring of maximum temperature (T_{max}) in the cable and the continuous comparison in each time step with the current sharing temperature (T_{cs}) during the simulation. When $T_{\text{max}} = T_{\text{cs}}$, a stop-condition implemented in the time-dependent solver stops the simulation and provides the quench heater delay for the considered operational conditions.

4.1.3 Governing equation

Thermal simulations consist in solving the two-dimensional heat balance equation in transient conditions:

$$\gamma c_p \frac{\partial T}{\partial t} = \frac{\partial}{\partial y} \left(k \frac{\partial T}{\partial y} \right) + \frac{\partial}{\partial z} \left(k \frac{\partial T}{\partial z} \right) + q_{\text{gen,ss}} \quad (4.2)$$

where $T = T(z, y, t)$ (in K) is the temperature, $\gamma = \gamma(z, y)$ (in kg/m³) the mass density and $c_p = c_p(z, y, T, B)$ (in J/(kg·K)) the specific heat. The space dependence of material properties is included because of the presence of different materials modelled domains. The term $q_{\text{gen,ss}} = q_{\text{gen,ss}}(z, y, t, T)$ (in W/m³) is the internal volumetric heat source applied in stainless-steel heater which simulates heater powering. The volumetric heat generation in the heater could be defined as follows [Salmi2014]:

$$q_{\text{gen,ss}}(t, T) = \rho_{\text{ss}}(T) J_{\text{ss}}^2(t) \quad (4.3)$$

where $\rho_{\text{ss}}(T)$ (in Ω·m) is the stainless-steel electrical resistivity and $J_{\text{ss}}^2(t)$ (in A/m²) is the heater current density, or using the following relation:

$$q_{\text{gen,ss}}(t) = \frac{P_{\text{QH}}(0)}{d_{\text{QH}}} e^{-\frac{2t}{\tau}} \quad (4.4)$$

where $P_{\text{QH}}(0)$ in (W/m²) is the heater peak power density obtained dividing the heater power by the heating surface area, d_{QH} is the heater thickness and τ the time constant of an exponential heater current decay.

4.1.4 Boundary conditions

With reference to the 2-D model presented in figure 4.5, adiabatic boundary conditions were set on the symmetry boundaries, at $z=0$ and $z=PH_{\text{period}}/2$:

$$k \frac{\partial T}{\partial z} \Big|_{z=0, z=PH_{\text{period}}/2} = 0 \quad (4.5)$$

which means the heat flow in z -direction at $z=0$ and $z=PH_{\text{period}}/2$ is zero. The temperature at the top and bottom of the system were fixed at T_{bath} , which is the helium bath temperature, and it is equal to 1.9 K in our simulations.

In the computation, we assumed a perfect thermal contact at the interfaces between the different materials. Using this assumption, the temperature is continuous and the heat equation is unchanged at the interfaces between materials. Implementation of thermal contact resistances

could improve the model and give more accurate results; however, the experimental characterization of interface parameters of materials requires a large effort.

4.1.5 Material properties

The temperature and magnetic field dependency were considered for all material properties. To analyze the heat transfer from heater to superconducting cable in transient conditions, the thermal conductivity k (in $W/(m \cdot K)$) and volumetric heat capacity $S = \gamma c_p$ (in $J/(K \cdot m^3)$) for each material are required. Material properties were extracted from literature [NIST] and coded in MATLAB following the NIST parametrization described in [Man2018].

To compute the cable material properties, we considered Cu/non-Cu ratio, filling factor (fraction of bare cable cross-section occupied by the strands) and RRR. Since the bare cable is composed by Nb_3Sn , copper and epoxy (and/or G10) thermal properties were averaged according to cable components volume fractions. Thermal conductivity and volumetric heat capacity for cables are shown in Figure 4.4, while curves of single materials used in the model are plotted in figures 4.6-4.11.

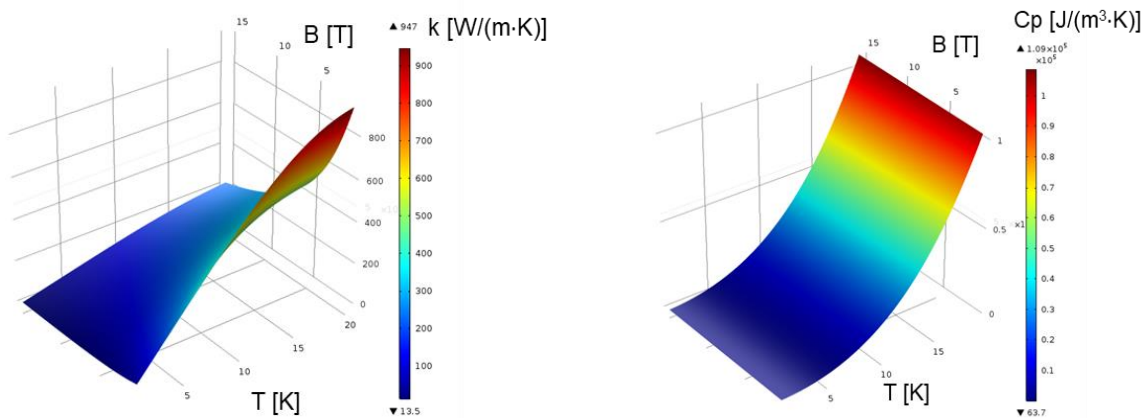


Figure 4.6: Thermal conductivity (left) and volumetric heat capacity (right) for the cables as a function of temperature and magnetic field for MQXF magnet.

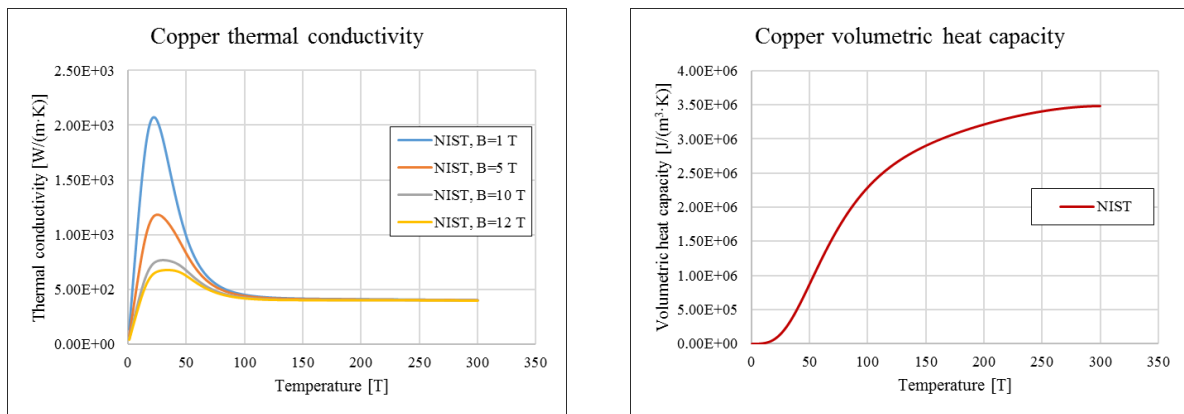


Figure 4.7: Thermal conductivity of copper (left) as a function of temperature and magnetic field. Volumetric heat capacity of copper (right) as a function of temperature [NIST]. Properties are computed using RRR=100.

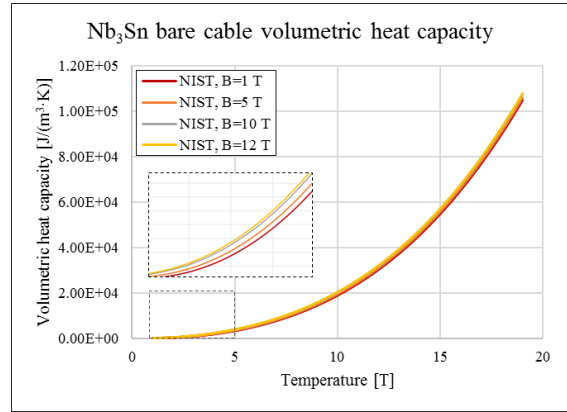
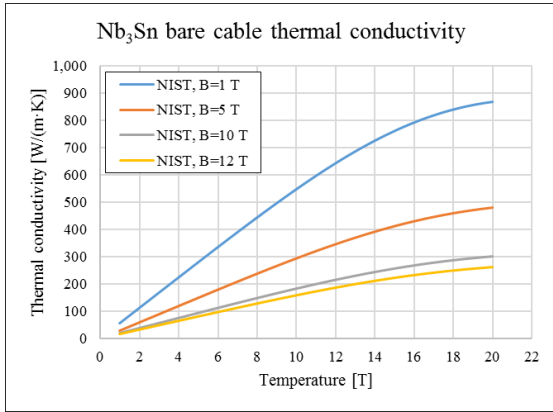


Figure 4.8: Thermal conductivity (left) and volumetric heat capacity (right) of Nb₃Sn bare cable as a function of temperature and magnetic field. Volumetric heat capacity of copper (right) as a function of temperature [NIST].

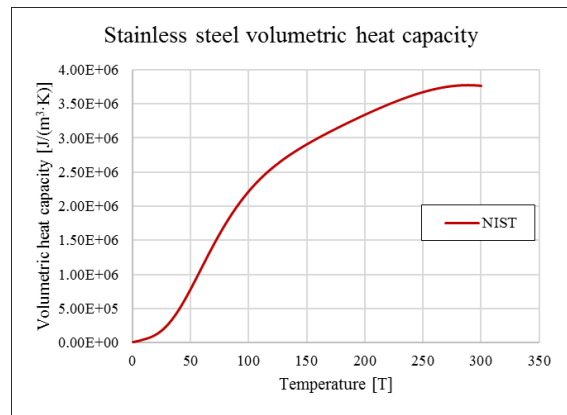
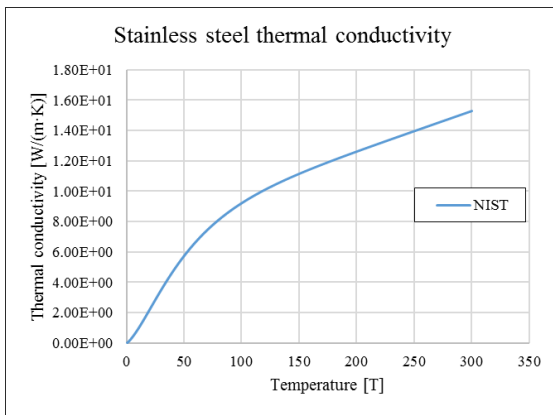


Figure 4.9: Thermal conductivity (left) and volumetric heat capacity of stainless-steel (right) as a function of temperature [NIST].

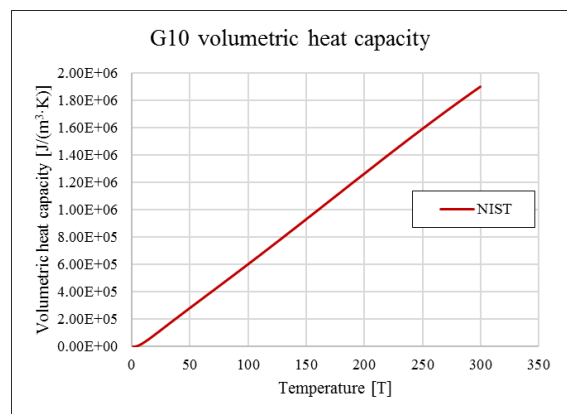
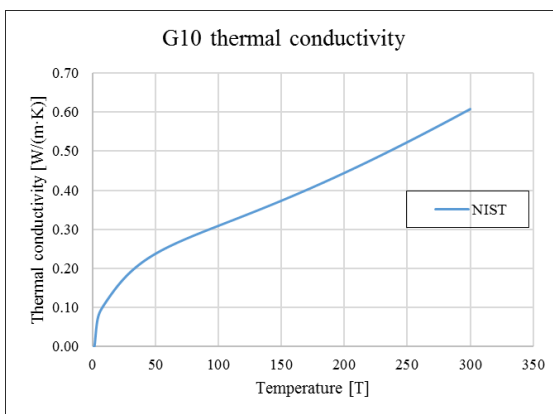


Figure 4.10: Thermal conductivity (left) and volumetric heat capacity (right) of G10 as a function of temperature [NIST] (right).

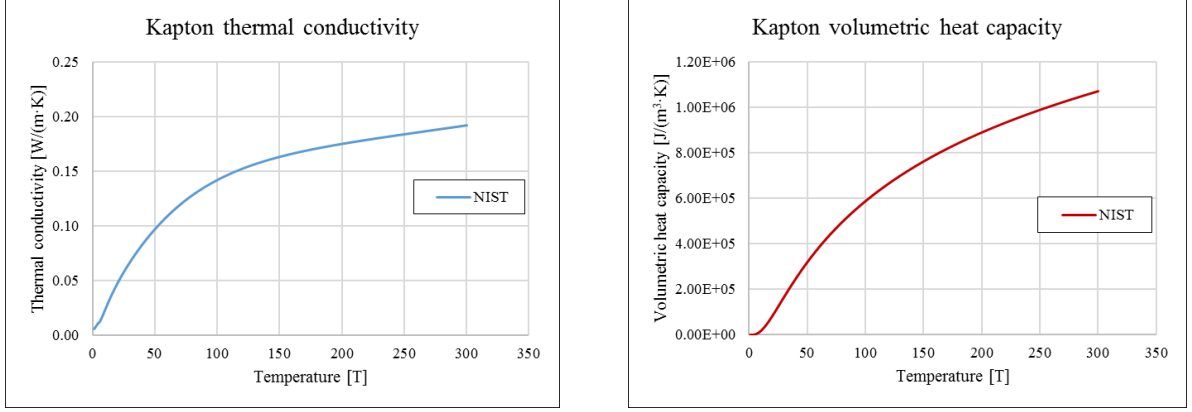


Figure 4.11: Thermal conductivity (left) and volumetric heat capacity (right) of Kapton as a function of temperature [NIST] (right).

4.1.6 Current sharing temperature

The current sharing temperature T_{cs} was computed taking into account the dependency of magnetic field B and the ratio between the load line fraction x_i , i.e., the ratio between the operational current and the short sample current. Intrinsic longitudinal strain ε was neglected in our model. The computation of the critical temperature T_c comes from the calculation of the critical current density $J_c(T, B, \varepsilon)$ using the ITER-2008 parametrization [Bot2009], whose equations are reported as follows:

$$J_c(B, T, \varepsilon) = \frac{C_0}{B} s(\varepsilon) (1 - \tilde{t}^{1.52}) (1 - \tilde{t}^2) \tilde{b}^{0.5} (1 - \tilde{b})^2 \quad (4.6)$$

$$B_{c2}(T, \varepsilon) = B_{c20} s(\varepsilon) (1 - \tilde{t}^{1.52}) \quad (4.7)$$

$$T_c(B, \varepsilon) = T_{c0} [s(\varepsilon)]^{\frac{1}{3}} \left(1 - \frac{B}{B_{c2}(0, \varepsilon)}\right)^{\frac{1}{1.52}} \quad (4.8)$$

where C_0 (in AT) is the normalization constant, $s(\varepsilon)$ a strain function, $B_{c2}(T)$ and B_{c20} (in T) respectively the upper critical field and the upper critical field at zero temperature and strain, and T_{c0} (in K) the maximum critical temperature at zero field and strain. Furthermore, the parameters \tilde{t} and \tilde{b} are expressed as:

$$\tilde{t} = \frac{T}{T_{c0}} \quad (4.9)$$

$$\tilde{b} = \frac{B}{B_{c2}(T, \varepsilon)} \quad (4.10)$$

The critical surface and $T_{cs}=T_{cs}(B, x_i)$ for MQXFS magnet are respectively shown in figures 4.12 and 4.13.

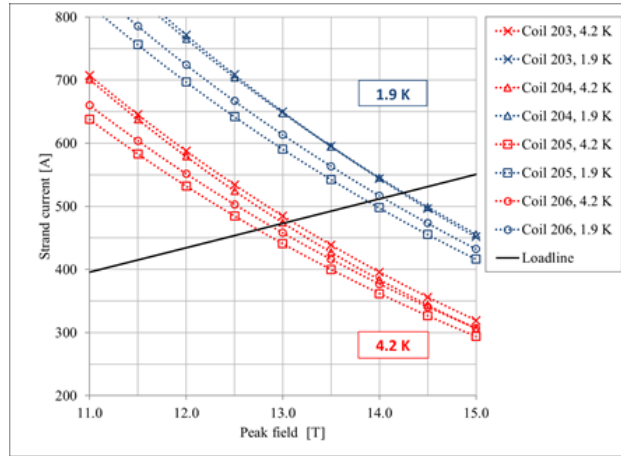


Figure 4.12: Critical surface for MQXFS coils at 1.9 K and 4.2 K.

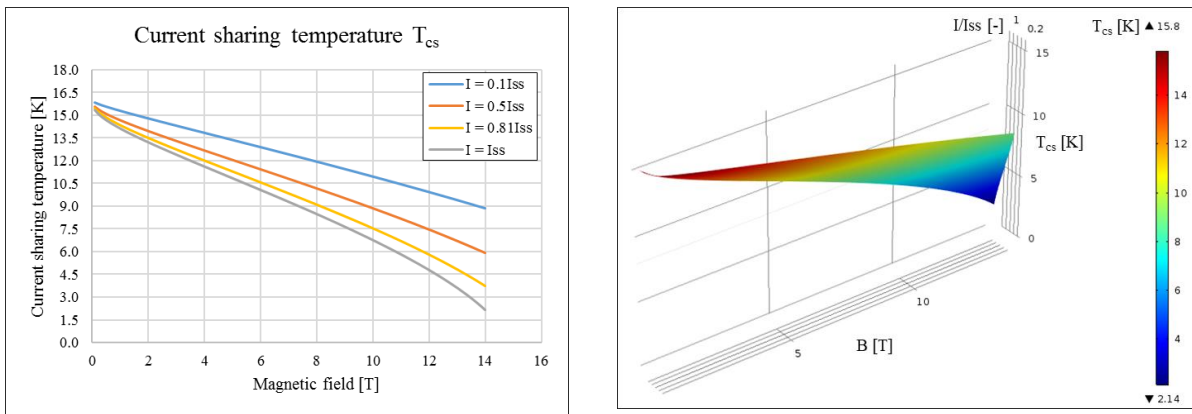


Figure 4.13: Current sharing temperature for MQXFS magnet as a function of the magnetic field and load line fraction (left). Current sharing temperature surface used in COMSOL model (right).

4.1.7 Numerical solution

Continuous equations were spatially discretized by a Finite Element approach based on the Galerkin method on computation grid made of quadrilateral elements. Influence of spatial discretization was preliminary studied in order to assure mesh-independent results. A computational grid made 5,100 elements was retained for computations. The mesh has a maximum relative error of 2% with respect to the finer grid used for the initial mesh test. For time-marching simulations we used an Implicit Differential-Algebraic (IDA) solver based on a variable-order and variable-step-size Backward Differentiation Formulas (BDF) [Hin2005].

4.2 Quench heater delay analysis for MQXFS5 magnet

4.2.1 Quench heater delay simulations results

The aim of the simulations is to verify the quench protection of MQXFS5 magnets in machine relevant conditions up to ultimate current. We simulated the quench heater delays for the MQXFS5 quadrupole firing only outer layer (OL) quench heaters. Inner layer (IL) quench heaters were not powered with the aim to study the impact of powering the heaters on the bubbles formed in the inner diameter of the coils, observed in previous versions of the magnet (MQXFS1 and MQXFS3) [RepMQXFS5]. The nominal quench heater circuit and magnet parameters used in simulations are respectively listed in table 4.1 and table 4.2. The time constant RC and peak current on the heater circuit is adjusted to machine relevant conditions adding in series a resistance to the quench heater circuit (see Figure 4.14). Figure 4.15 shows quench heater wiring layout with the position of the heater firing units in the coil.

Table 4.1: Nominal quench heater parameters for OL simulations of MQXFS5 magnet [RepMQXFS5].

Outer layer heaters		
Voltage	[V]	900
Capacitance	[mF]	7.05
Peak current	[A]	200
Total resistance heater circuit	[Ω]	4.5
RC	[ms]	32
Peak power density	[W/cm ²]	218
Energy density in the HS	[J/cm ²]	3.46

Table 4.2: Nominal MQXFS5 magnet parameters [RepMQXFS5].

Nominal magnet current	[kA]	16.47
Ultimate magnet current	[kA]	17.79
$I_{\text{nom}}/I_{\text{ss}}$ at 1.9 K	[-]	0.77
Peak magnetic field at I_{nom}	[T]	11.40
Nominal gradient	[T/m]	132.60
Operational temperature T_{op}	[K]	1.9

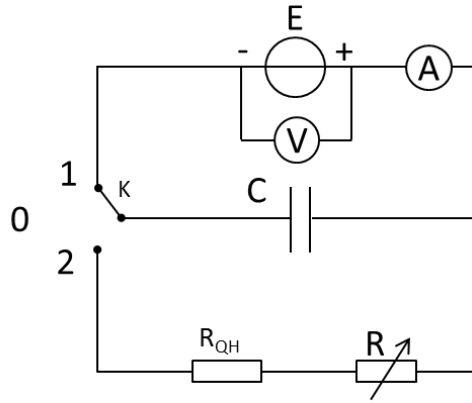


Figure 4.14: Outer layer quench heater circuit [RepMQXFS5].

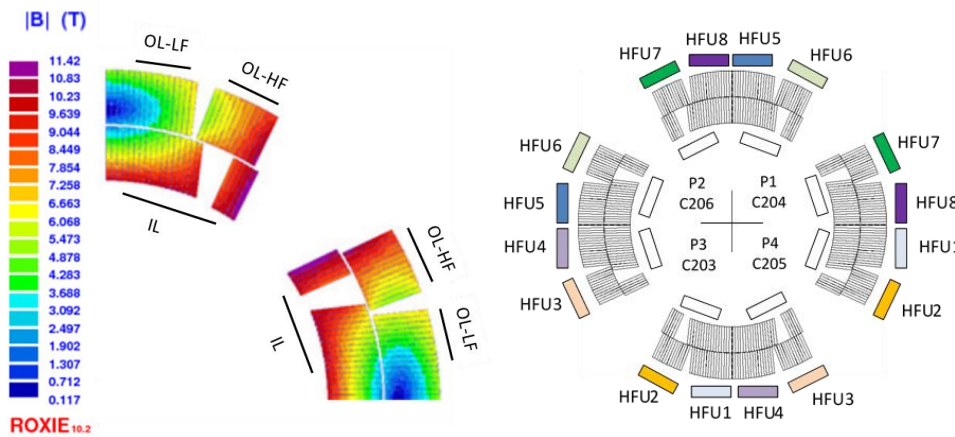


Figure 4.15: Cross-section of one MQXFS5 coil with protection heaters position (left) [Izq2018]. Quench heater wiring layout for MQXFS5 magnet (right) [RepMQXFS5].

Heater performance studies are carried out for the coil outer layer in the following cases:

- Quench heater delays as a function of the magnet current firing the high field heaters (OL-HF);
- Quench heater delays as a function of the magnet current firing low field heaters (OL-LF);
- Sensitivity analyses at nominal magnet current on quench heater delays changing the normalization constant C_0 , heater station voltage and resistance, and G10 insulation thickness between heater and coil.

4.2.1.a Protection heater delays, outer layer high field and outer layer low field

Figure 4.16 shows measured and computed quench heater delays for OL-HF block and OL-LF block as a function of magnet current. Considering nominal quench heaters parameters listed

in table 4.1, values of simulated delays at nominal magnet current are 9.6 ms for the OL-HF block and 13.4 ms for the OL-LF block. Simulated delays are in good agreement with measurements carried out at by G. Willering et al. at SM18 test facility, with a good reproducibility at high current. The large spread at lower current does not critical because of the wide margin in terms of quench protection. Furthermore, at low current is not very easy to identify the heater delay basing on the experimental voltage signals. Tables 4.3-4.4 summarize experimental results for outer layer high field and outer layer low field quench heater tests respectively.

Table 4.3: OL-HF quench heater test results for MQXFS5 magnet [RepMQXFS5].

Type	I_{mag} [A]	Quench heater delay [ms]
ALL OL fired	1640	194
ALL OL fired	4940	86
ALL OL fired	8240	46
ALL OL fired	13180	22
ALL OL fired	16470	12
OL-HF heaters fired in coil 204	3300	81
OL-HF heaters fired in coil 204	8240	20
OL-HF heaters fired in coil 205	3300	142
OL-HF heaters fired in coil 205	8240	31
OL-HF heaters fired in coil 205	4940	63

Table 4.4: OL-LF quench heater test results for MQXFS5 magnet [RepMQXFS5].

Type	I_{mag} [A]	Quench heater delay [ms]
OL-LF heater fired in coil 206 and coil 204	1652	168
OL-LF heater fired in coil 206 and coil 204	3300	130
OL-LF heater fired in coil 206 and coil 204	8240	27
OL-LF heater fired in coil 206 and coil 204	13180	21
OL-LF heater fired in coil 206 and coil 204	16470	8.8
OL-LF heater fired in coil 204	3300	96
OL-LF heater fired in coil 204	8240	30
OL-LF heater fired in coil 205	3300	147
OL-LF heater fired in coil 205	8240	31

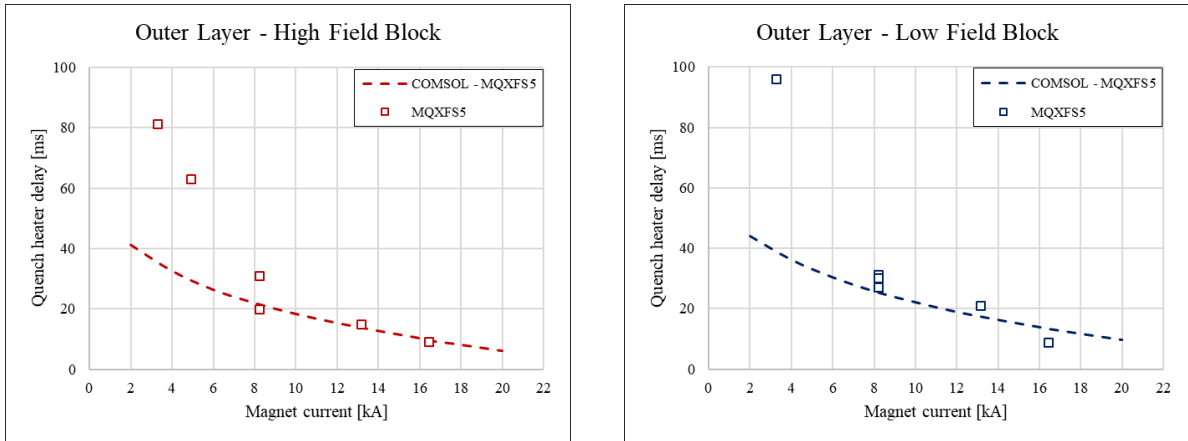


Figure 4.16: Computed and measured heater delay as a function of the magnet current for MQXFS5 magnet. The left figure corresponds to the delay in the outer layer high field block and the right figure the outer layer low field block.

Figure 4.17 shows the thermal map for the OL-HF block for the investigated nominal case. The maximum temperature reached in the model at quench onset instant is 171 K in the stainless-steel heater.

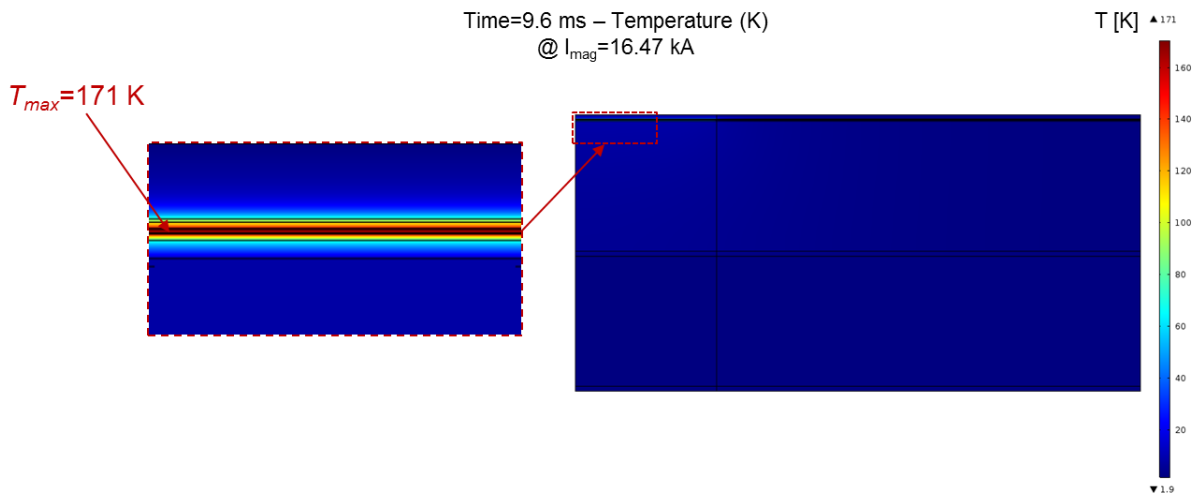


Figure 4.17: Thermal map of the coil and enlargement near the heater zone for the nominal case.

The quench in the outer layer cable occurs when the maximum temperature of the cable is equal to the current sharing temperature, in other words, when their difference called *temperature margin* is null. Figure 4.18 shows the temperature evolution in the cables and in the stainless-steel heater until the current sharing temperature is reached in the coil. In this case, after a time delay of 9.6 ms, the maximum temperature reached in the outer layer cable is 8.6 K and quench location is near the outer layer quench heater, as shown in Figure 4.19.

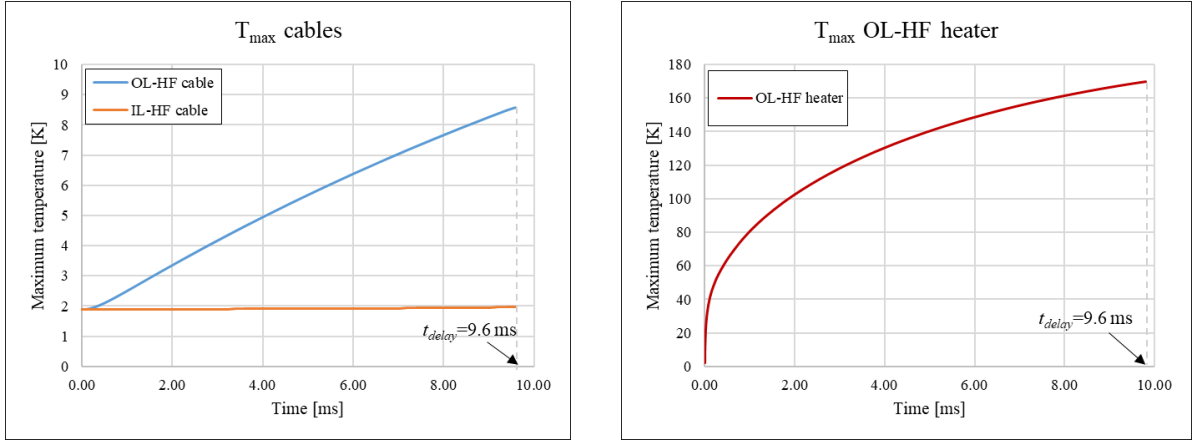


Figure 4.18: Temperature evolution in OL-HF and OL-LF cables (left) and in the OL heater (right) until the quench onset for the nominal case.

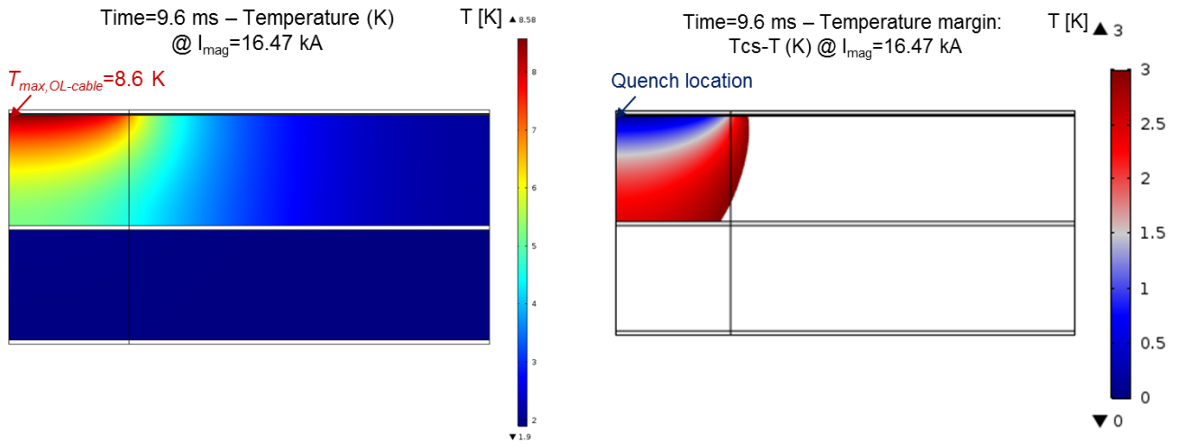


Figure 4.19: Maximum temperature in the OL and IL cables (left) and temperature margin map until 3 K (right) for the nominal case.

4.2.1.b Protection heater delays, sensitivity analysis on heater delays changing the normalization constant C_0

Figure 4.20 shows measured and computed quench heater delays for MQXFS5 outer layer as a function of the magnet current in case the normalization constant C_0 is varied by $\pm 10\%$ of the nominal standard value. Results show that there is not a significant impact on quench heater delay values for the investigated case. Table 4.5 shows the standard values of ITER-2008 critical surface parametrization for HiLumi magnets.

Table 4.5: Critical surface parameters for HiLumi magnets.

Upper critical field B_{c20}	[T]	30
Maximum critical temperature T_{c0}	[K]	16
Normalization constant C_0	[AT/mm ²]	1.61E+05
α exponent	[-]	0.96

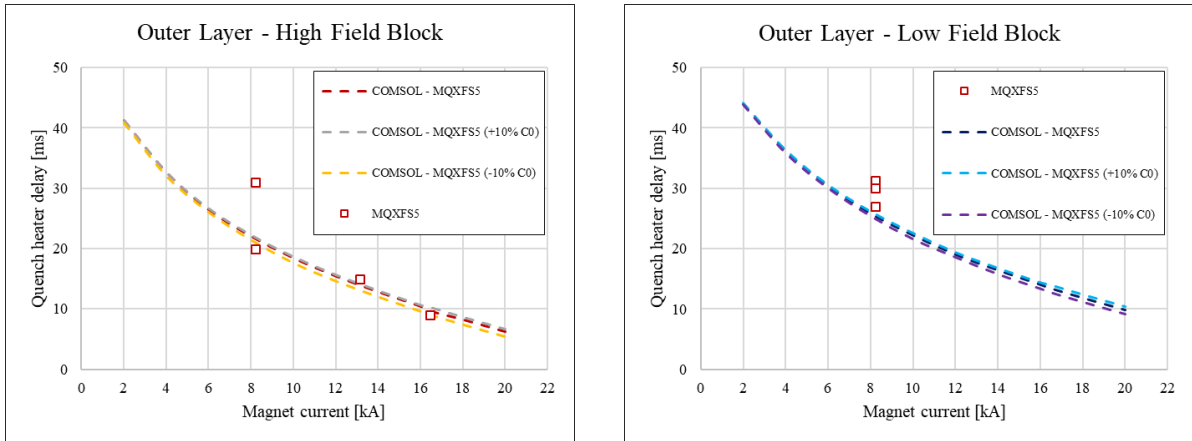


Figure 4.20: Sensitivity analysis on the normalization constant C_0 : computed and measured heater delay as a function of the magnet current for MQXF55 magnet.

4.2.1.c Protection heater delays, sensitivity analysis on heater delays changing heater station voltage and resistance

Sensitivity analyses on heater delays were performed for coil outer layer at nominal magnet current changing heater station powering parameters. In the first analysis, the total resistance and the capacitance of the heater station were kept at nominal values, respectively 4.5Ω and 7.05 mF , and voltage was changed in the range of 300 V to 900 V . Secondly, we decided to keep constant the nominal heater current, i.e. 200 A , and the capacitance (7.05 mF) changing the total resistance in the range of 1Ω to 4.5Ω . From the first analysis, quench heater delays as a function of the heater current were computed, as shown on the left in Figure 4.21. As results of the second analysis, we obtained quench heater delays as a function of the heater time constant, as shown on the right in Figure 4.21.

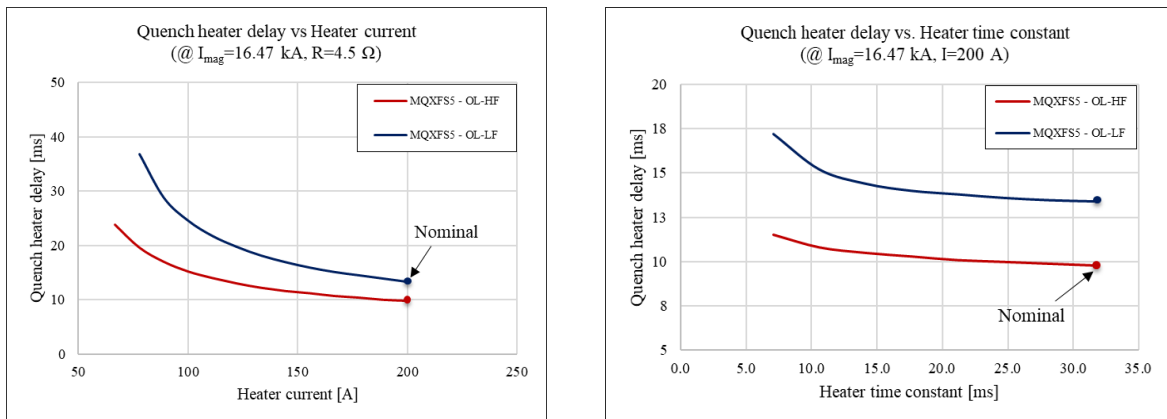


Figure 4.21: Sensitivity analysis changing heater station powering parameters: computed heater delay as a function of the heater current (left) and heater time constant (right) for MQXF55 magnet.

4.2.1.d Protection heater delays, sensitivity analysis on G10 insulation thickness

An additional analysis was performed on the sensitivity of the heater delay to the amount of insulation between the heater and the coil. The standard insulation configuration between the heater and the insulated cable is composed by an insulated layer of Kapton and glue. We decided to add in the model an additional layer of G10 insulation between heater and coil varying the thickness of this layer in the range of 0 mm to 0.2 mm. Figure 4.22 shows the quench heater delays as a function of the additional G10 insulation thickness, in case of outer layer quench heater are fired. Heater delays increases of a factor 3 when we consider an additional layer of 0.2 mm between heater and insulated cable.

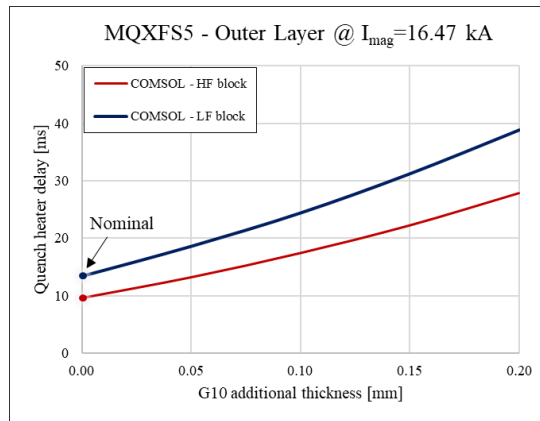


Figure 4.22: Sensitivity analysis changing G10 insulation thickness between heater and coil: computed heater delay as a function of the G10 insulation thickness for the OL-HF and OL-LF for MQXFS5 magnet.

4.2.2 Heater temperature profile

Figure 4.23 shows temperature profile of the outer layer high field heater as a function of time for the two sensitivity analyses performed changing heater voltage (on the left) and resistance (on the right) and discussed in section 4.2.2.c.

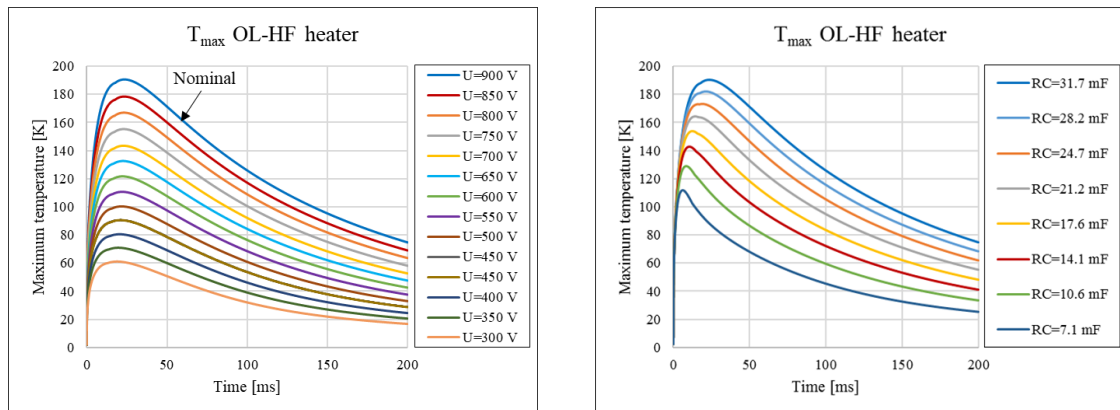


Figure 4.23: Heater temperature as a function of time changing voltage (left) and resistance (right) for MQXFS magnet.

4.2.3 Heat diffusion in the coil

The knowledge of the thermal properties of coil materials is of fundamental importance for the quench heater delay analysis of Nb₃Sn magnets. The heat transfer phenomena inside the coil during a quench is dominated principally by the value of the thermal conductivity, as discussed in the section 5. Figure 4.24 shows for different time instant the temperature evolution as a function of the coil height for coil section in which the maximum temperature has been detected. The heat generated in the heater is spread following a bell-shaped curve which becomes flat along the outer layer cable. The change on the slope of the temperature curves underlines the different values of thermal conductivity of coil materials.

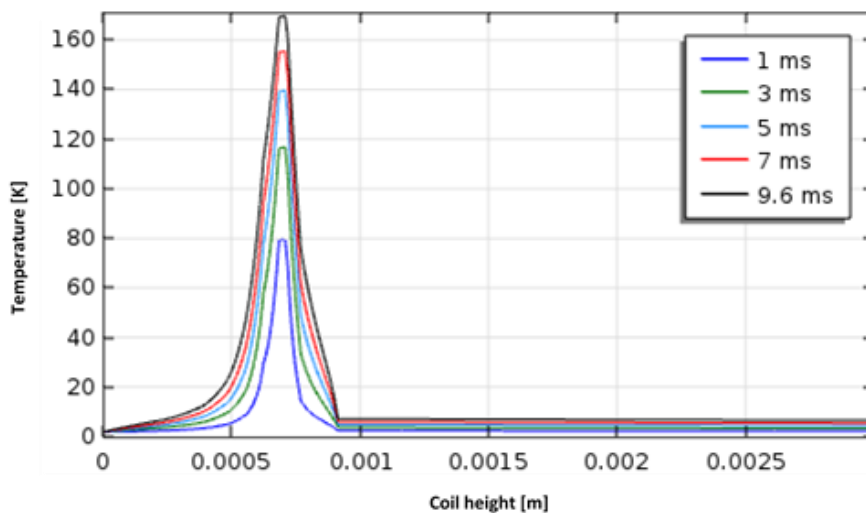


Figure 4.24: Heat diffusion along the coil height for different time instants for nominal case.

4.3 Quench heater analysis results and for 11 T magnet

4.3.1 Quench heater delay simulations results

Quench protection was verified also for 11 T magnet. Simulations were carried out for MBHSP106 version with the aim to prove the quench protection of magnet in machine relevant conditions up to ultimate current [RepMBHSP106]. In addition to the standard tests of the Outer Layer (OL) quench heaters, for the first time a set of tests were performed to characterize the behavior of the Inter Layer (InL) quench heaters under development. The nominal outer layer and inter layer quench heater parameters for MBHSP106 magnet used during experimental tests and in simulations are respectively listed in table 4.6 and table 4.7, while main magnet parameters are reported in table 4.8.

Table 4.6: Outer layer quench heater parameters for MBHSP106 magnet.

		Outer layer heaters HF	Outer layer heaters LF
Voltage	[V]	900	900
Capacitance	[mF]	7.05	7.05
Peak current	[A]	150	150
Total resistance heater circuit	[Ω]	6	6
RC	[ms]	42	42
Peak power density	[W/cm ²]	85	136
Energy density in the HS	[J/cm ²]	1.8	2.9

Table 4.7: Inter layer quench heater parameters of MBHSP106 magnet used in simulations.

		Inter layer heaters
Voltage	[V]	450
Capacitance	[mF]	7.05
Peak current (B1/B2/B3)	[A]	61/88/27
Total resistance heater circuit	[Ω]	5
RC	[ms]	36
Peak power density (B1/B2/B3)	[W/cm ²]	62/101/62
Energy density in the HS (B1/B2/B3)	[J/cm ²]	1.1/1.8/1.1

Table 4.8: MBHSP106 magnet parameters.

Nominal magnet current	[kA]	11.85
Ultimate magnet current	[kA]	12.85
I_{nom}/I_{ss} at 1.9 K	[-]	0.79
Peak magnetic field at I_{nom}	[T]	11.76
Operational temperature T_{op}	[K]	1.9

Heater performance studies are carried out for the following cases using powering parameters listed in table 4.6 for outer layer quench heaters and table 4.7 parameters for inter layer quench heaters:

- Quench heater delays as a function of the magnet current firing the outer layer high field heaters (OL-HF);
- Quench heater delays as a function of the magnet current firing only inter layer quench heaters (InL-HF, InL-MF, InL-LF);
- Quench heater delays as a function of the magnet current firing at the same time outer layer and inter layer quench heaters (OL+InL);

- Sensitivity analyses at nominal magnet current on quench heater delays changing heater station voltage and resistance of the inter layer heater station, in case we fired only OL heaters or OL+InL heaters;
- Sensitivity analyses at nominal magnet current on quench heater delays changing G10 insulation thickness between outer layer heater and coil for the coil outer layer, in case only OL heaters are fired.

4.3.1.a Protection heater delays, outer layer quench heaters high field

Results for OL-HF quench heater delay tests are summarized in Table 4.9 and compared to the simulated model in Figure 4.25. Simulated delays are in good agreement with experimental data.

Table 4.9: OL-HF quench heater tests results for MBHSP106 magnet.

Type	I_{mag} [A]	Quench heater delay [ms]
1 OL-QH fired – Coil 116	6000	30
1 OL-QH fired – Coil 116	8000	23
1 OL-QH fired – Coil 116	10000	17
1 OL-QH fired – Coil 116	11850	13
1 OL-QH fired – Coil 117	6000	27
1 OL-QH fired – Coil 117	8000	24
1 OL-QH fired – Coil 117	10000	17
1 OL-QH fired – Coil 117	11850	13

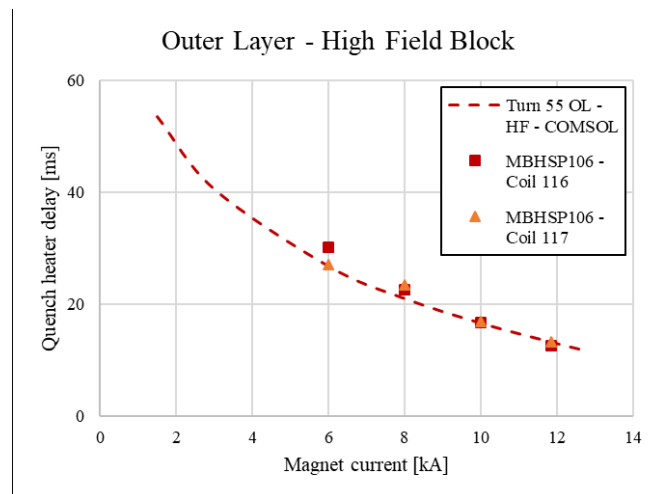


Figure 4.25: Measured and computed heater delays for MBHSP106 magnet (outer layer high field block).

Figure 4.26 shows the thermal map of the turns 55-19 (OL-HF block) for the investigated nominal case. The maximum temperature reached in the model at quench onset instant is 113 K in the stainless-steel heater.

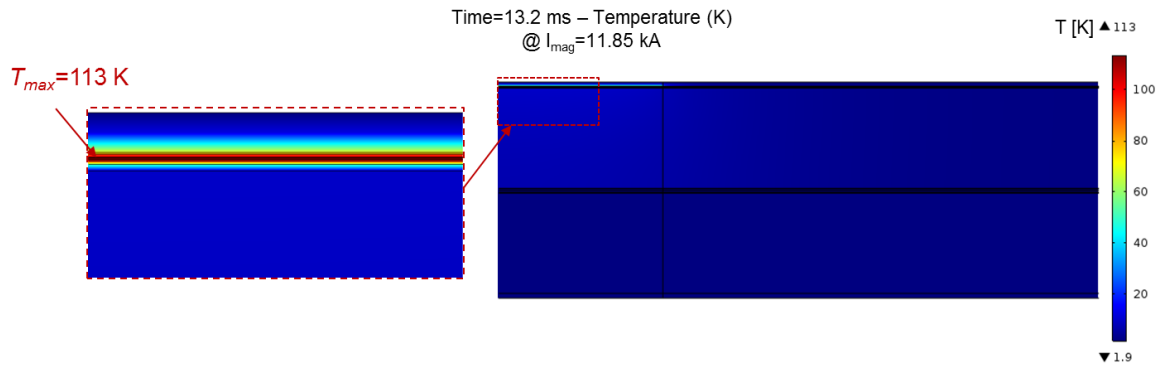


Figure 4.26: Thermal map of the coil and enlargement near the heater zone for turn 55 (nominal case).

Figure 4.27 shows the temperature evolution in the two turns of high field block, i.e. turns 55-19, and in the stainless-steel heater of the same block until the current sharing temperature is reached in the coil. In this case, after a time delay of 13.2 ms, the maximum temperature reached in the outer layer cable is 9.9 K and quench location is near the outer layer quench heater, as shown in Figure 4.28.

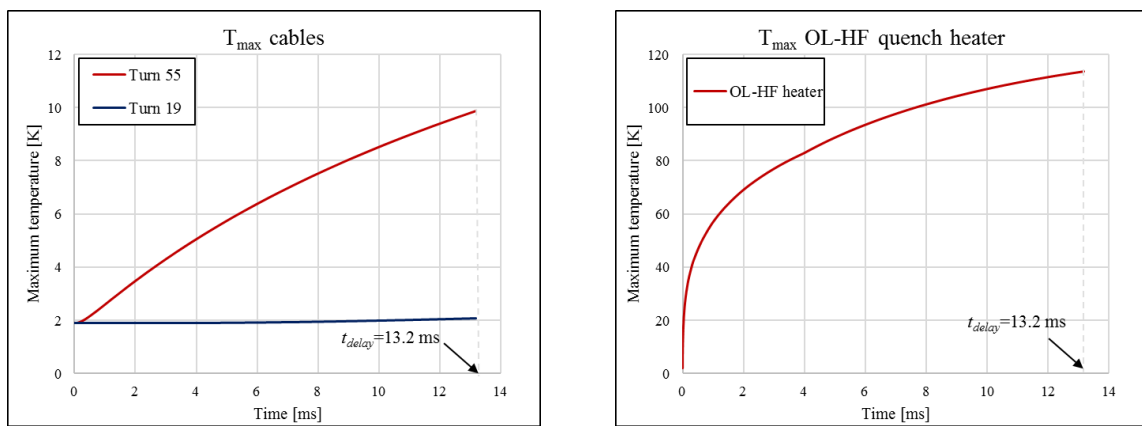


Figure 4.27: Temperature evolution in OL-HF and OL-LF cables (left) and in the OL heater (right) until the quench onset for the nominal case.

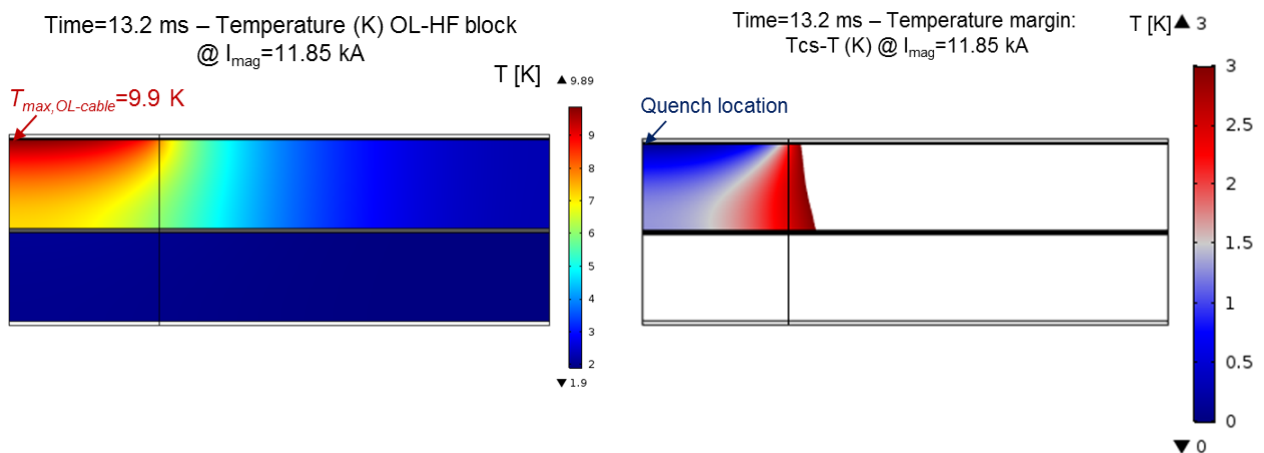


Figure 4.28: Maximum temperature for turns 55-19 HF block (left) and temperature margin map until 3 K (right) for the nominal case.

4.3.1.b Protection heater delays, inter layer quench heaters

Figure 4.29 show the magnetic field map for MBHSP106 coil with the positions of inter layer quench heaters. We simulated the behavior of 8 turns, shown in Figure 4.29, in case we fired only inter layer quench heaters:

- Turn 55 and turn 19 for the HF zone of the coil (i.e. Block 3);
- Turn 44 and turn 16 for the MF zone of the coil (i.e. Block 2);
- Turn 31 and turn 8 for the LF zone of the coil (i.e. Block 1).

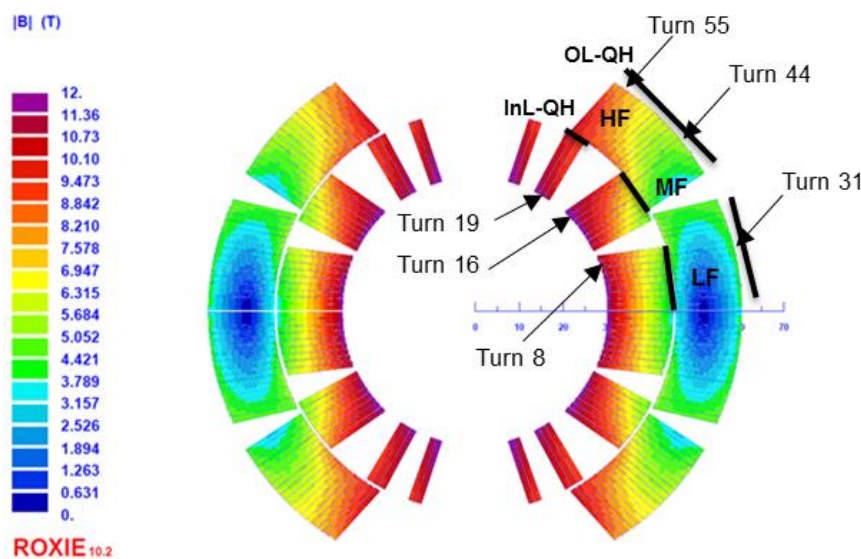


Figure 4.29: Cross-section of MBHSP106 coil with turns investigated and protection heaters position.

Measured and computed delays are reported in Figure 4.30. Table 4.10 summarizes inter layer quench heater test results. In coil 117 delays are in agreement with expectations. We have noticed a faster quench than expected in coil 116. This is probably due the fact that is not easy to identify the heater delay basing on the experimental voltage signals (see voltage signals in Section 1 of Annex 1), especially at low current. However, it seems that turn 8 and turn 44 well represent measurements. In the experimental data the quench starts in Block 1, which would correspond to turn 8 in the simulations.

Table 4.10: InL quench heater tests results for MBHSP106 magnet.

Type	I_{mag} [A]	Quench heater delay [ms]
1 IL-QH fired – Coil 116	6000	No quench visible
1 IL-QH fired – Coil 116	8000	27
1 IL-QH fired – Coil 116 (left)	6000	No quench visible
1 IL-QH fired – Coil 116 (left)	8000	20
1 IL-QH fired – Coil 116 (left)	10000	8
1 IL-QH fired – Coil 116 (left)	11850	6
1 IL-QH fired – Coil 117 (left)	10000	31
1 IL-QH fired – Coil 117 (left)	11850	25

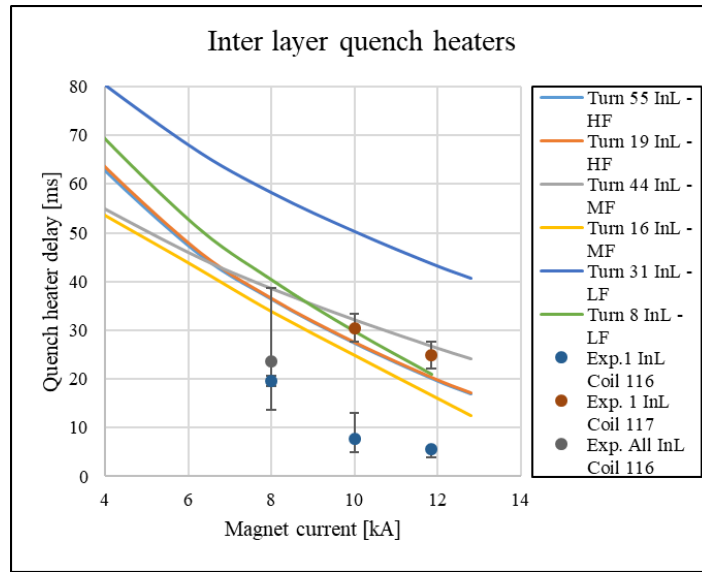


Figure 4.30: Measured and computed heater delays for MBHSP106 (inter layer).

4.3.1.c Protection heater delays, inter layer and outer layer quench heaters

We simulated also the behavior of the 8 turns investigated in section 4.4.2.b in case we fired both outer layer and inter layer quench heaters. Simulated delays for the three investigated blocks are reported in Figures 4.31-4.33. From results, it seems that only outer layer cable benefits in term of quench delay when both heaters (outer layer and inter layer quench heaters) are activated, especially at low current. Inner layer cable, instead, is not affected of the activation of both heaters, principally because heat generated in the inter layer quench heater is spread towards both cables.

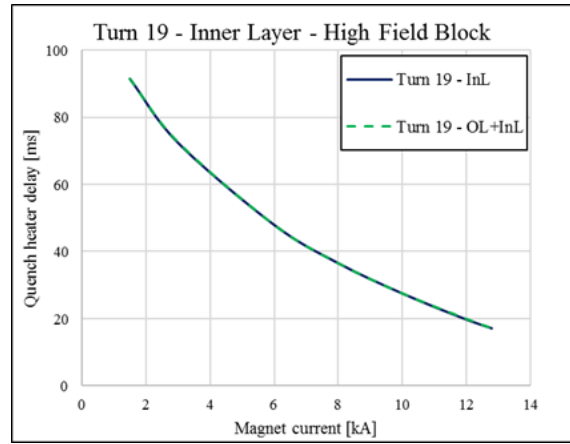
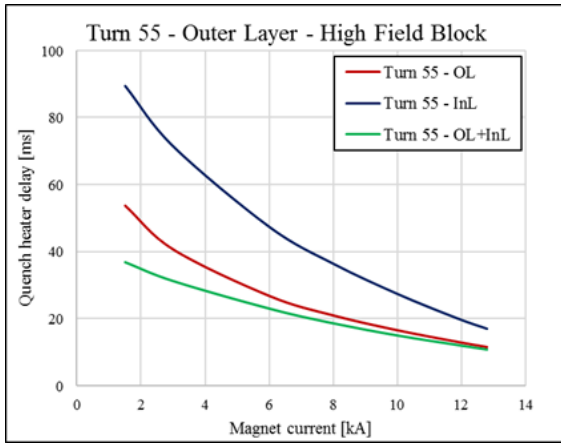


Figure 4.31: Computed heater delays as a function of the magnet current for turns 55 and 19.

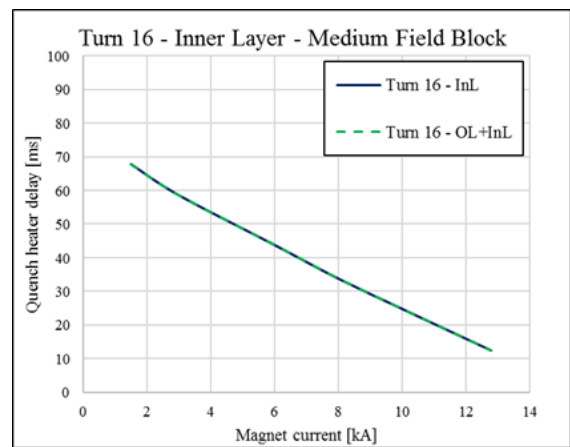
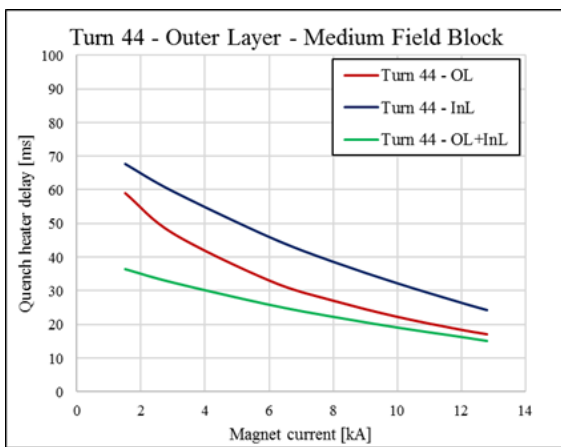


Figure 4.32: Computed heater delays as a function of the magnet current for turns 44 and 16.

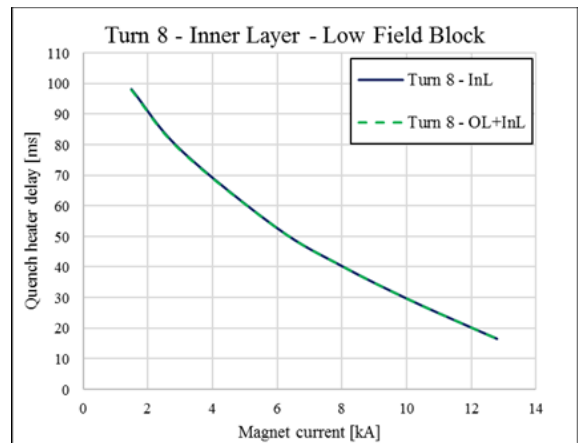
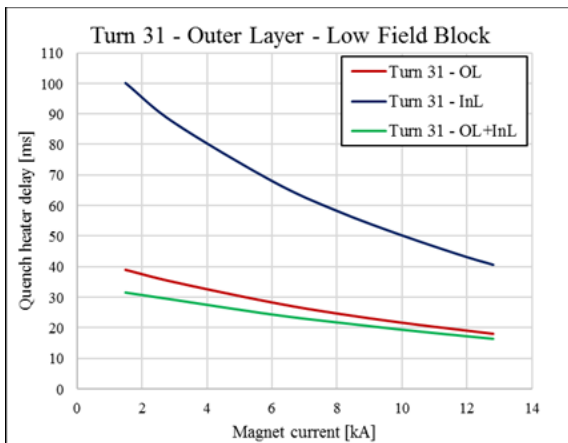


Figure 4.33: Computed heater delays as a function of the magnet current for turns 31 and 8.

Figures 4.34-4.36 show for the three heater configurations (OL-QH, InL-QH and OL-QH+InL-QH) the thermal map of turns 55-19 with heat flux lines and the temperature margin in the range 0-3 K after 12 ms from heater activation, which corresponds to the minimum heater delay among the three cases.

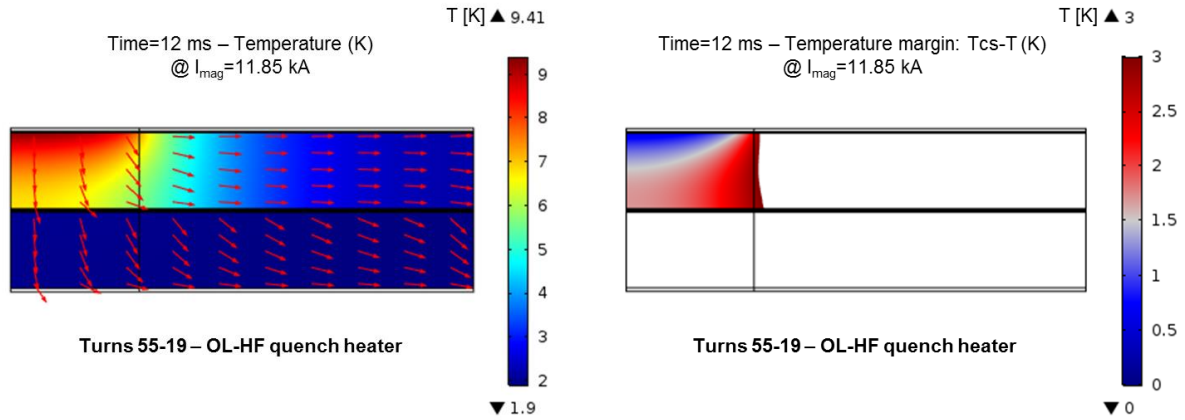


Figure 4.34: Thermal map for turns 55-19 with heat flux lines (left) and temperature margin in the range 0-3 K (right) after 12 ms from outer layer quench heater activation.

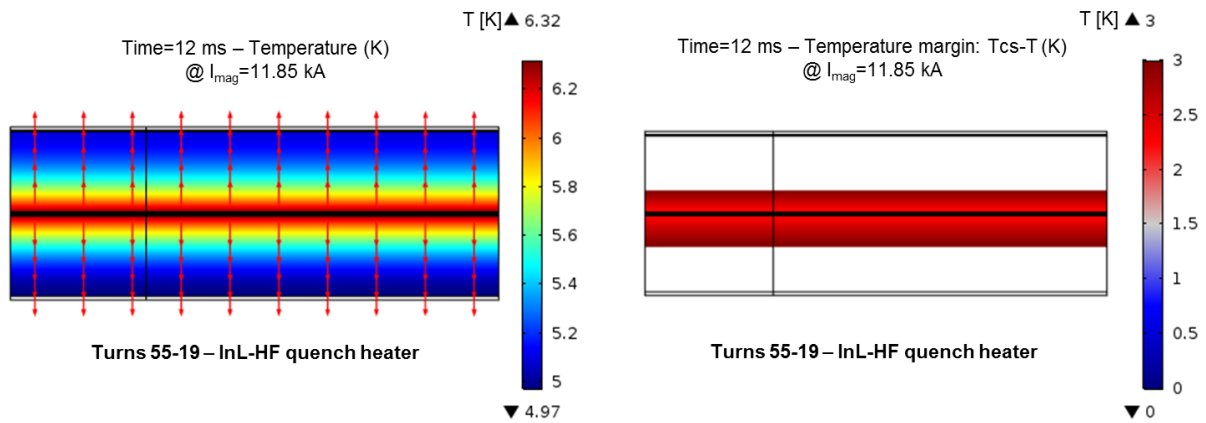


Figure 4.35: Thermal map for turns 55-19 with heat flux lines (left) and temperature margin in the range 0-3 K (right) after 12 ms from inter layer quench heater activation.

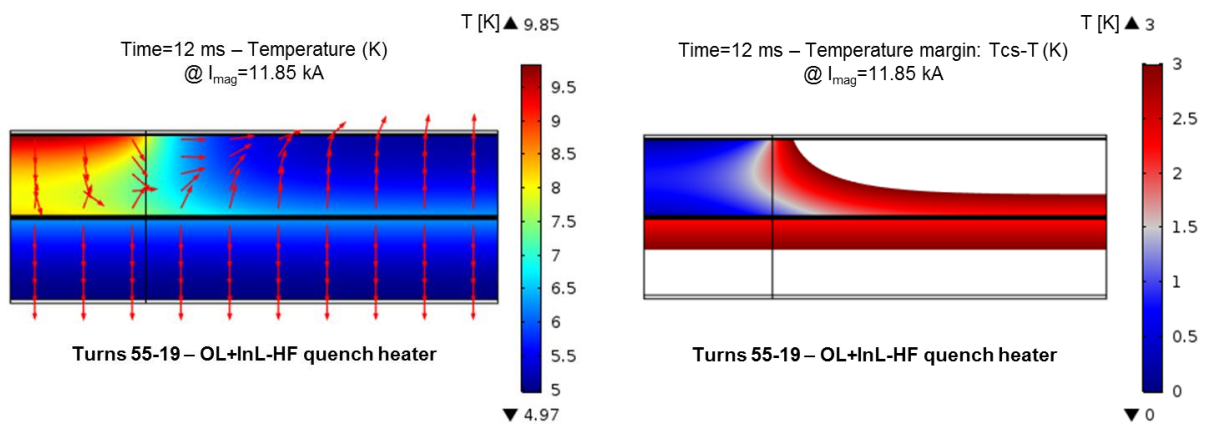


Figure 4.36: Thermal map for turns 55-19 with heat flux lines (left) and temperature margin in the range 0-3 K (right) after 12 ms from outer layer and inter layer quench heaters activation.

When only outer layer quench heater is fired (OL-QH case), the heat flux lines go from the heater to cables following a curved path. Heat flux follows a vertical path in two opposite directions from the inter layer to cables when only inter layer quench heater is fired (InL-QH case). Both heat flux contributions are presented when both heaters are fired (OL-QH + InL-QH). This combined configuration already permits at 12 ms to quench the outer layer cable and a large fraction of outer layer cable results resistive. However, at nominal magnet current the difference in terms of delay with the OL-QH configuration is very modest. This is also confirmed by the quench integral analysis at nominal current. Figure 4.37 shows the current decay and quench integral for the two investigated cases, where $t=0$ corresponds to protection triggering time. From the plot, the reduction of the quench load due to the use of inter layer quench heaters is very modest (OL only=12.1 MA²s, OL+InL=11.4 12.1 MA²s).

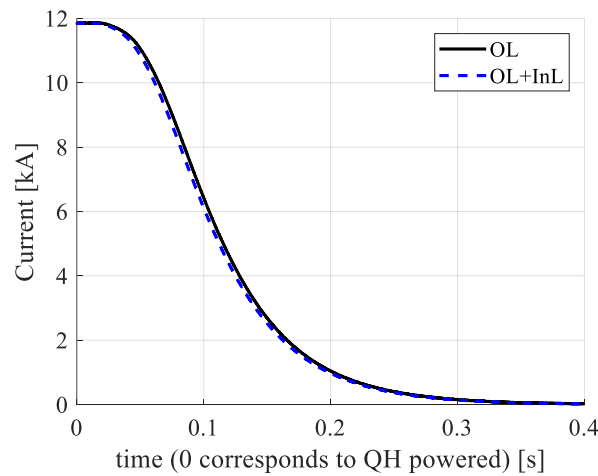


Figure 4.37: Current decay for the case where only outer layer heater are fired (OL) and the case where outer layer + inter-layer heaters (OL + InL) are both fired.

4.3.1.d Protection heater delays, sensitivity analysis on heater delays changing inter layer heater station voltage and resistance

Sensitivity analyses on heater delays were performed for the 8 turns investigated at nominal magnet current changing only powering parameters of the inter layer heater station. In the first analysis we varied the inter layer heater station voltage of $\pm 20\%$ with respects to the nominal value. In the second analysis we varied in the same way the inter layer heater station resistance. Figures 4.38-4.39 show the quench heater delays for the high field turns (55 and 19) as a function of the heater current in case we change voltage of the inter layer heater station. Figures 4.40-4.41 report delays for the same turns in case we change resistance of the inter layer heater station. From results, it seems that in both analyses there is a significant impact on delays at low field for outer layer and inner layer cable when only inter layer quench heaters are fired. When both heaters are fired, there is not a strong impact on outer cable delay, but only for inner layer cable.

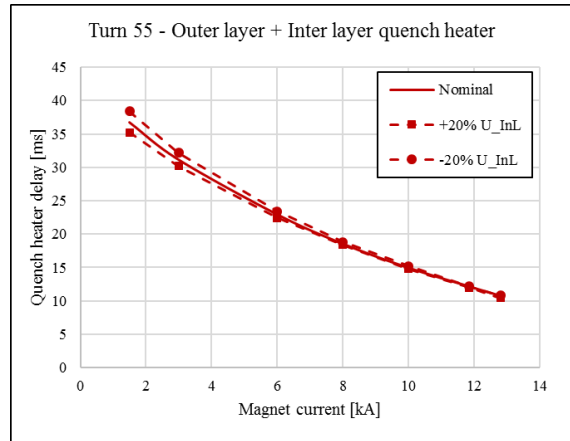
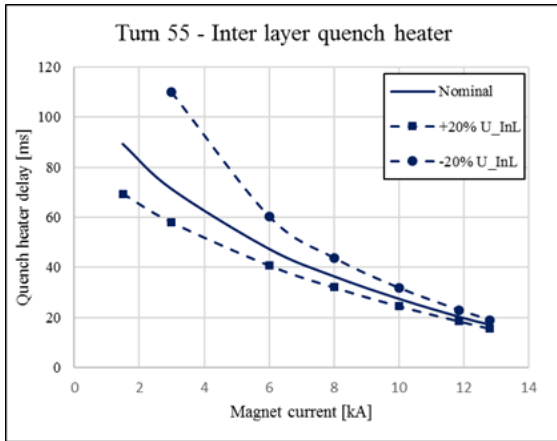


Figure 4.38: Computed heater delays as a function of the magnet current for turns 55 – voltage case.

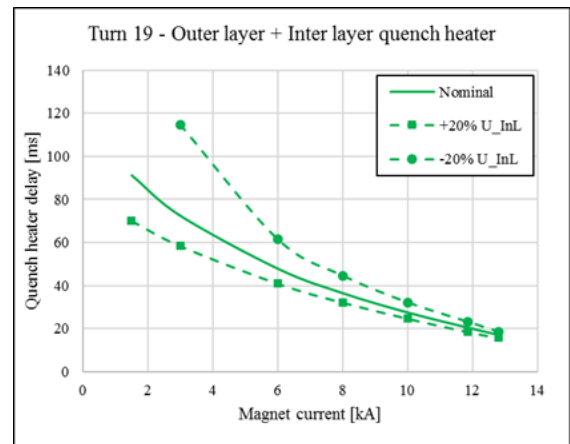
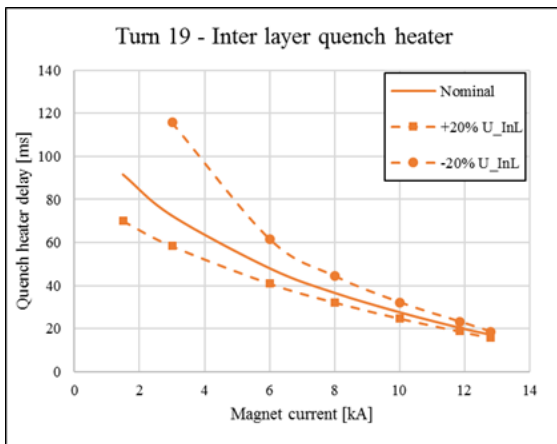


Figure 4.39: Computed heater delays as a function of the magnet current for turns 19 – voltage case.

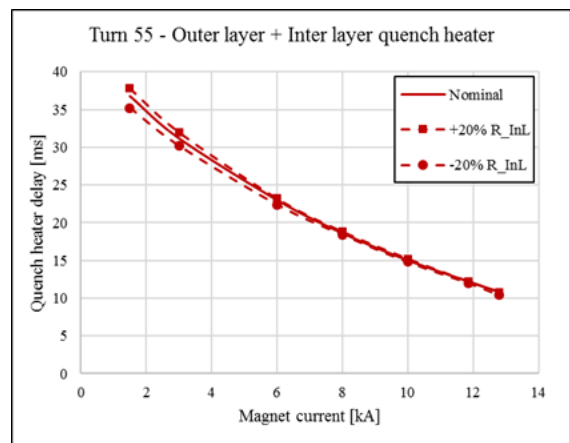
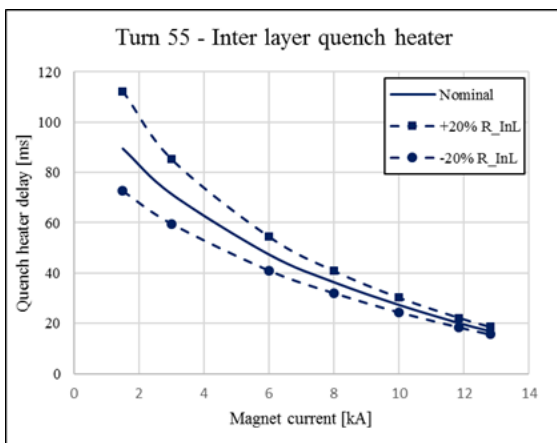


Figure 4.40: Computed heater delays as a function of the magnet current for turns 55 – resistance case.

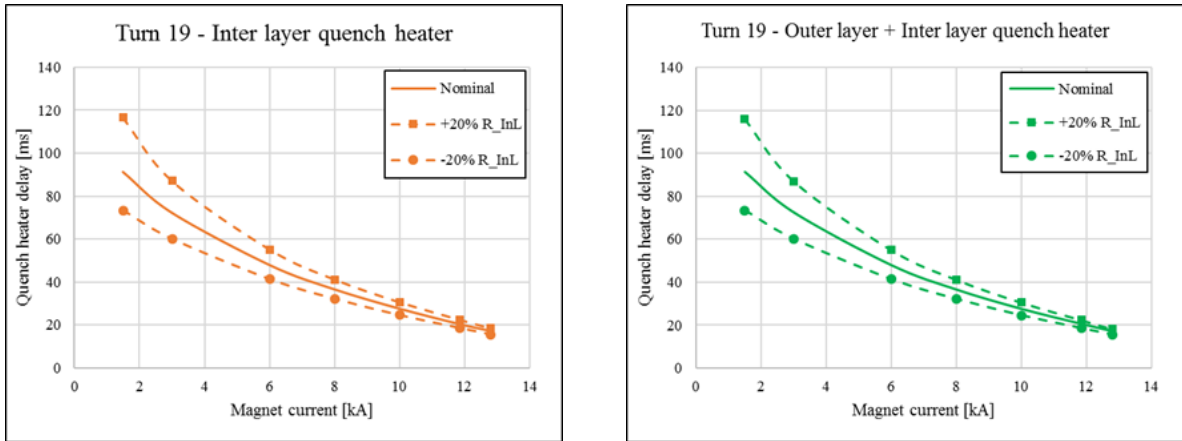


Figure 4.41: Computed heater delays as a function of the magnet current for turns 19 – resistance case.

4.3.1.e Protection heater delays, sensitivity analysis on G10 insulation thickness

Finally, an additional analysis was performed on the sensitivity of the heater delay to the amount of insulation between the outer layer heater and the coil. We decided to add in the model an additional layer of G10 insulation between heater and coil varying the thickness of this layer in the range of 0 mm to 0.2 mm. Figure 4.42 shows the quench heater delays as a function of the additional G10 insulation thickness, in case only outer layer heaters are fired. Heater delays increases of a factor 3 when we consider an additional layer of 0.2 mm between heater and insulated cable.

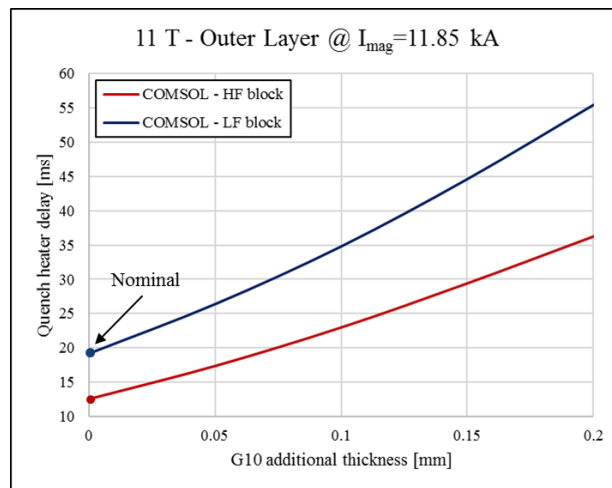


Figure 4.42: Sensitivity analysis changing G10 insulation thickness between heater and coil: computed heater delay as a function of the G10 insulation thickness for the OL-HF and OL-LF block for MBHSP106 magnet.

4.4 Estimation of the heater adiabatic temperature

4.4.1 Analytical approach

The adiabatic temperature of the heater can be estimated following an analytical approach based on measured heater current. The analysis was performed only for the outer layer heater of MQXFS5 magnet, but it can be replicated also for other magnets. The differential heat dissipation dE_{QH} associated to the current I_{QH} flowing in the heater is given by:

$$dE_{QH} = \frac{\rho_{SS} l_{QH} I_{QH}^2}{w_{QH} d_{QH}} dt \quad (4.12)$$

where $\rho_{SS}=5.45E-07$ (in $\Omega \cdot m$) is the stainless-steel electrical resistivity, l_{QH} the heater length, w_{QH} the heater width, d_{QH} the heater thickness and t the time. The current in the heater decays according the following formula:

$$I_{QH} = I_{QH_0} e^{-t/\tau} \quad (4.13)$$

where I_{QH_0} is the heater current at $t=0$ and $\tau=RC$ the heater time constant. The change in internal energy in the stainless-steel heater is proportional to the change in temperature dT :

$$dE_{QH} = C_{p,ss}(T) V_{QH} dT \quad (4.14)$$

where $C_{p,ss}(T)$ (in $J/(m^3 \cdot K)$) is the volumetric heat capacity of stainless-steel and V_{QH} the heater volume. Equating and integrating equations (4.12) and (4.14), the adiabatic increase of temperature can be estimated by:

$$\int_{T_{op}}^{T_{fin.}} C_{p,ss}(T) dT = \int_0^{\infty} \rho_{SS} \frac{I_{QH_0}^2}{w_{QH}^2 d_{QH}^2} e^{-2t/\tau} dt \quad (4.16)$$

where $T_{fin.}$ is the final temperature reached by the heater. Figure 4.43 shows the heater current decay and the related adiabatic increase of temperature in the heater as a function of time for MQXFS5 magnet. Table 4.11 shows values used in the analytical analysis.

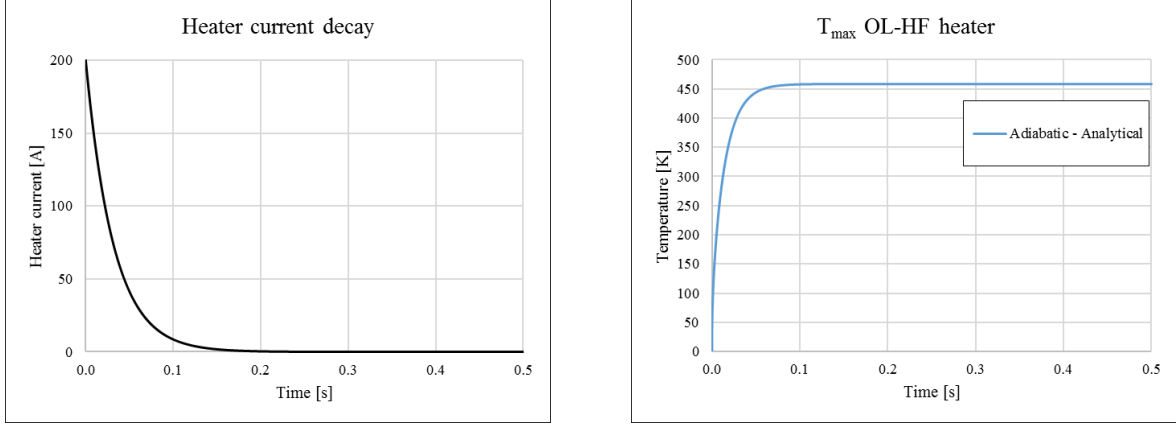


Figure 4.43: Heater current decay (left) and adiabatic increase of temperature as a function of time (right) for OL-HF quench heater of MQXFS5 magnet.

Table 4.11: Parameters used in adiabatic heater temperature analysis for MQXFS5 magnet.

Stainless-steel electrical resistivity ρ_{SS}	$[\Omega \cdot m]$	5.45E-07
Stainless-steel volumetric heat capacity $C_{p,ss}(T)$	$[J/(m^3 \cdot K)]$	See Fig. 4.6
Heater length l_{QH}	$[mm]$	40
Heater width w_{QH}	$[mm]$	20
Heater thickness d_{QH}	$[\mu m]$	25
Peak heater current I_{QH0}	$[A]$	200
Circuit time constant τ	$[ms]$	32

4.4.2 FE heater model approach

A 2-D finite element model of the heater was built in COMSOL to compare the computed numerical heater temperature with the analytical one. The problem consists in solving the two-dimensional heat balance equation (see equation (4.2)) in transient conditions in a rectangular domain representative of the heater geometry. Adiabatic conditions were applied in all the boundaries and the same heater power density of the analytical case (218 W/cm^2) was applied in the model as heat source. Figure 4.44 shows the adiabatic heater temperature as a function of time compared with the analytical adiabatic temperature. The analytical adiabatic temperature curve approaches the numerical one with a gap of 2.7% in regime zone i.e. 0.3 s. In the same figure, a comparison on the heater temperature evolution between the adiabatic numerical model of the heater and the temperature evolution coming from the 2-D model of the coil analyzed in section 4.2 is shown. Table 4.12 shows maximum temperature values of the heater reached after 25 ms in the three investigated cases.

Table 4.12: Parameters used in adiabatic temperature analysis for MQXFS5 heater.

Maximum heater temperature (adiabatic) – Analytical model	$[K]$	458.5
Maximum heater temperature (adiabatic) – COMSOL model	$[K]$	471.1
Maximum heater temperature – COMSOL coil model	$[K]$	190.7

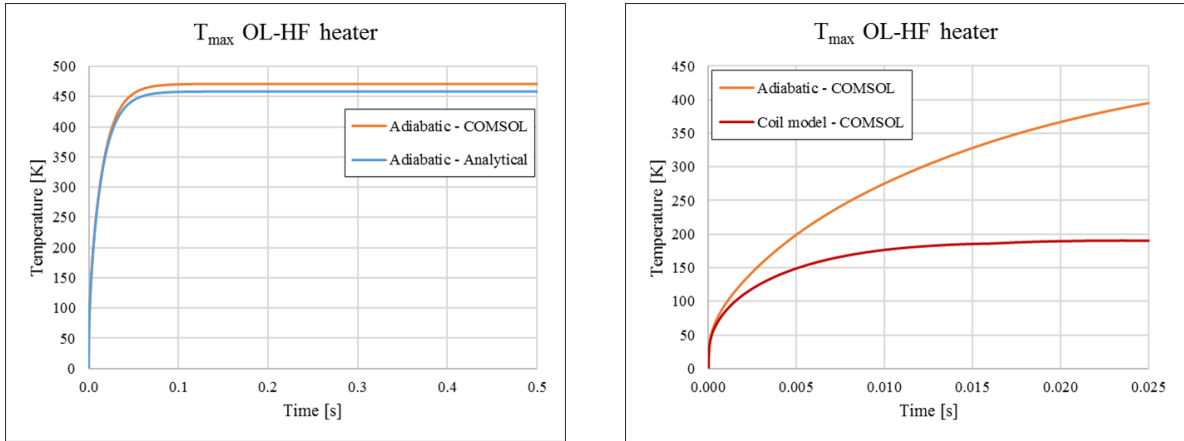


Figure 4.44: MQXFS5 heater temperature as a function of time for the adiabatic COMSOL model and the analytical model (left). Comparison between heater temperature in the adiabatic model and in the coil model (right).

4.5 Concluding remarks on quench heater analysis

This chapter described the numerical model used at CERN for quench heater delay simulations in high-field accelerator magnets. The model, developed in COMSOL, permits to evaluate the heater delays as a function of a large number of parameters as well as to perform different sensitivity analyses on quench heater delays. The computation is based on solving the heat diffusion equation from the heater to the cable in two dimensions, in order to estimate the time that the cables takes to reach the current sharing temperature from the heater activation. The stability of the model has been well verified. Simulated delays are in agreement with expectations. The model could be improved by considering thermal contacts between layers and including AC losses. Finally, an analytical estimation of the heater adiabatic temperature was carried-out and compared with the 2-D FE-model of a quench heater and the 2-D FE-model of the coil in COMSOL.

Chapter 5

Steady-state measurements and numerical modelling of thermal conductivity of impregnated Nb₃Sn cable stacks

Nowadays, Nb₃Sn represents the state-of-the-art of superconductor for high field accelerator magnets. In service, accelerator magnets are subjected to overheating caused by hysteretic losses and continuous heat deposition near the interaction regions. The performance of epoxy-impregnated coils is sensitive to thermal conductivity value, which plays a crucial role on the heat extraction from magnet coils and dominates quench propagation [Hil2009]. For this reason, thermal design and the knowledge of thermal properties, especially of the thermal conductivity of epoxy-impregnated coils, represent an unavoidable step for the design of these magnets [Imb2003].

In this chapter, we discuss about the thermal conductivity of epoxy impregnated Nb₃Sn cable and samples of different insulating materials. After a brief overview on the experimental procedure and setup used to determine the thermal conductivity of coil and single component samples, we will describe the numerical model carried-out in COMSOL to predict the thermal conductivity of a coil sample in the range from 5 K – 100 K. At the end, a comparison between results from numerical model and data from measurements campaign performed at CERN Cryolab is presented and discussed.

5.1 Thermal conductivity of single components

A measurement campaign to measure thermal conductivity of 11 Tesla dipole samples has been lunched at CERN Cryolab. Thermal conductivity measurements were carried-out for eight samples with different geometry and insulation layout, in order to understand the influence of each component on the total thermal conductivity of a sample. The procedure used to measure samples thermal conductivity is described in [Borg2016a, b, c]. Measurements have been compared with findings in literature and reported in this section. Main characteristics and geometrical parameters of 11 Tesla dipole samples are listed respectively in table 5.1 and table 5.2.

Samples #1 and #2 aimed at the characterization of the thermal properties of the CTD-101K resin. Samples #3-#4 were made to characterize the thermal properties of the impregnated S2-glass. Both samples consist of five layers of glass fiber (AGY 636 S-2 glass fiber [AGY]) reacted at 650 °C for 48 hours and impregnated in CTD-101K epoxy resin; samples are directly molded between two blocks of OFHC copper. The difference between the two samples is that sample #3 has not binder, while sample #4 contains the ceramic binder CTD-1202. In this way it was possible to study the thermal conductivity of glass fiber, even in case ceramic binder CTD-1202 is considered. In order to study the thermal conductivity contribution of mica, sample #5 was made with the same characteristics of sample #4 but adding mica sheets. After the

first set of measurements, it was understood that the interface contact resistance between the sample itself and copper blocks could be considered insignificant for thin samples, therefore a set of samples with different thickness were made in order to derive the contribution of the contact resistance (samples #6, #7 and #8). Figures 5.1-5.3 show the geometry of the different samples.

Table 5.1: Characteristics of different 11 Tesla dipole samples [Borg2016a].

Sample	Type	Resin type	Insulation	Binder	Reacted?
1	1 mm slab	CTD-101K	none	none	no
2	bulk	CTD-101K	none	none	no
3	1 mm slab	CTD-101K	S-2 glass 636 11 TEX	none	yes
4	1 mm slab	CTD-101K	S-2 glass 636 11 TEX	CTD-1202	yes
5	1 mm slab	CTD-101K	S-2 glass 636 11 TEX + mica	CTD-1202	yes
6*	5 mm slab	CTD-101K	none	none	no
7 ⁺	5 mm slab	CTD-101K	S-2 glass 636 11 TEX	none	yes
8 ⁺	7 mm slab	CTD-101K	S-2 glass 636 11 TEX	none	yes

*sample #6 was damaged during cooldown and measurement.

⁺samples #7 and #8 had to be reglued to the copper blocks after the initial manufacturing, due to one of the copper ends detaching from the sample prior to cooldown.

Table 5.2: Main geometrical parameters of different 11 Tesla dipole samples [Koe2017, Borg2016a, Borg2016b, Borg2016c].

Sample	a[mm]	b[mm]	L[mm]	A[mm ²]
1	8.00	7.50	1.00	60.00
2	9.97	4.00	33.00	39.88
3	8.07	8.09	1.19	65.29
4	8.23	8.24	1.12	67.82
5	8.01	8.04	0.94	64.40
6	7.95	7.93	4.93	63.04
7	8.12	8.17	5.00	66.34
8	8.12	8.17	7.00	66.34

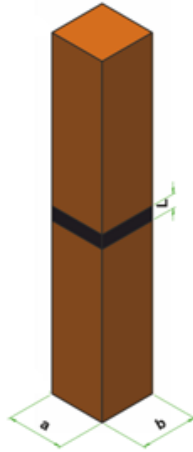


Figure 5.1: CAD design of sample #1 with characteristic dimensions [Mac2014].

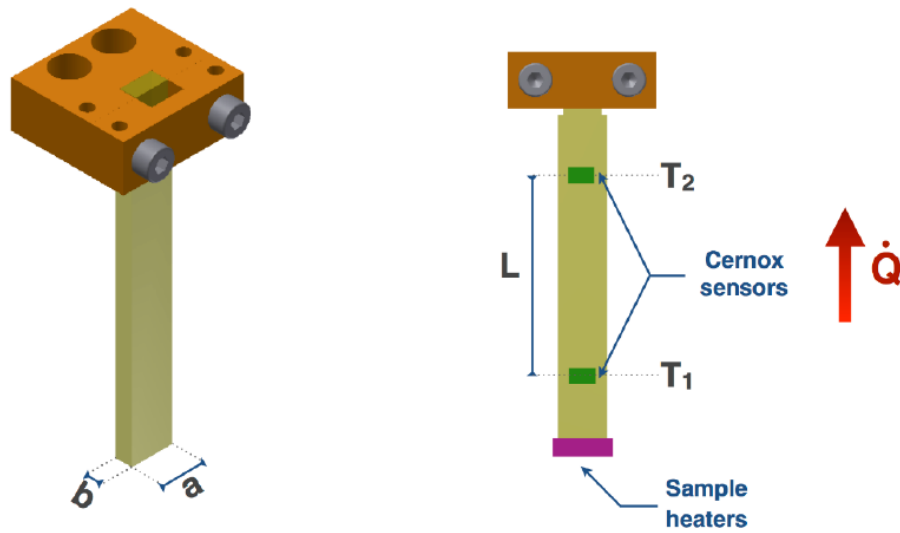


Figure 5.2: Sample holder and characteristic dimensions of sample #2 [Borg2016b].

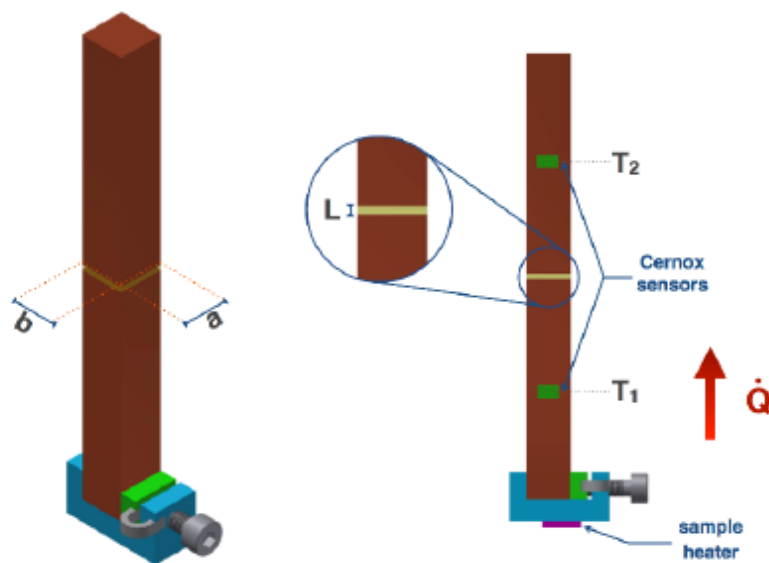


Figure 5.3: Sample holder and characteristic dimensions of samples #3, #4, #5, #6, #7 and #8 [Borg2016a, Borg2016c].

Figure 5.4 shows the thermal conductivity measurements of 11 Tesla dipole samples, compared also to literature curves of epoxy resin [CRYO] and G10 fiberglass epoxy [NIST]. Thermal conductivity curve of sample #8 closely matches that one of G10 when measured in the normal direction. Thermal conductivity of samples #7 and #8, which have also identical composition of sample #3, approaches that of the bulk CTD-101K sample (sample #2). This evidence may mean that the interface contact resistance between the sample itself and copper blocks could be considered insignificant for samples with long thermal pathway, as in the case of samples #7 and #8 [Borg2016a]. In the following sections, the results for the different samples will be discussed and compared to expected values from literature. Tables summarizing single components measurements are provided in Section 1 of Annex 2.

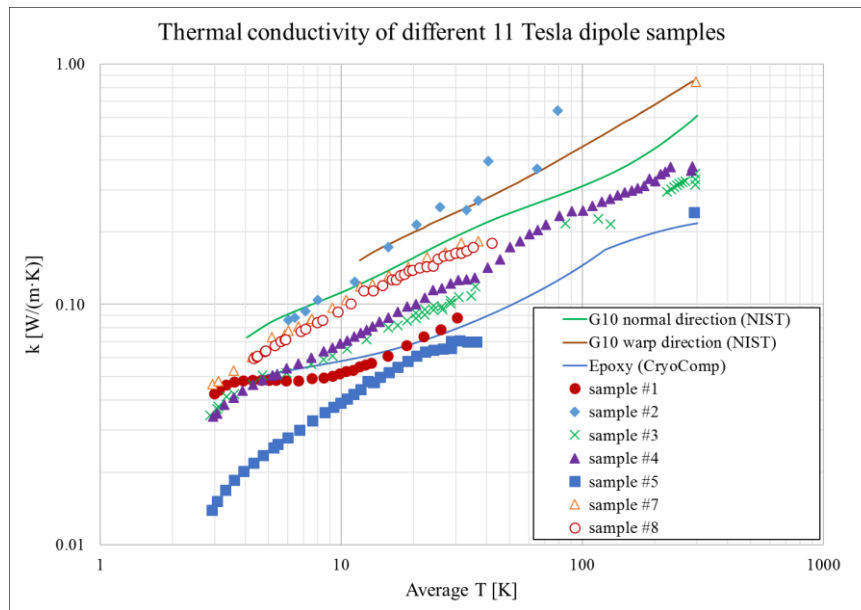


Figure 5.4: Thermal conductivity of 11 Tesla dipole measured at Cryolab and comparison with the thermal conductivity of epoxy resin [CRYO] and G10 [NIST] in both normal and warp directions.

5.1.1 Evaluation of the interface resistance

The evaluation of thermal contact resistance for the interfaces copper-to-sample represents a fundamental step to understand the influence of interfaces on thermal conductivity of analyzed samples. To do that, samples #3, #7 and #8 were used to estimate the interface resistance; these samples are identical in composition, but different in their active length (see table 5.1). The interface thermal resistance was estimated by considering the thermal conductivity results of samples #3 and #8. Sample #7 was reglued several times before cooldown and measurement; for this reason, it was not considered for the estimation of interface resistance [Borg2016a]. Nevertheless, since the thermal conductivity of sample #7 and sample #8 is very close, a 5 mm sample is considered long enough to neglect the impact of the thermal contact copper-to-sample. Figure 5.5 presents the measured thermal conductivity of sample #3, #7 and #8 as a function of temperature.

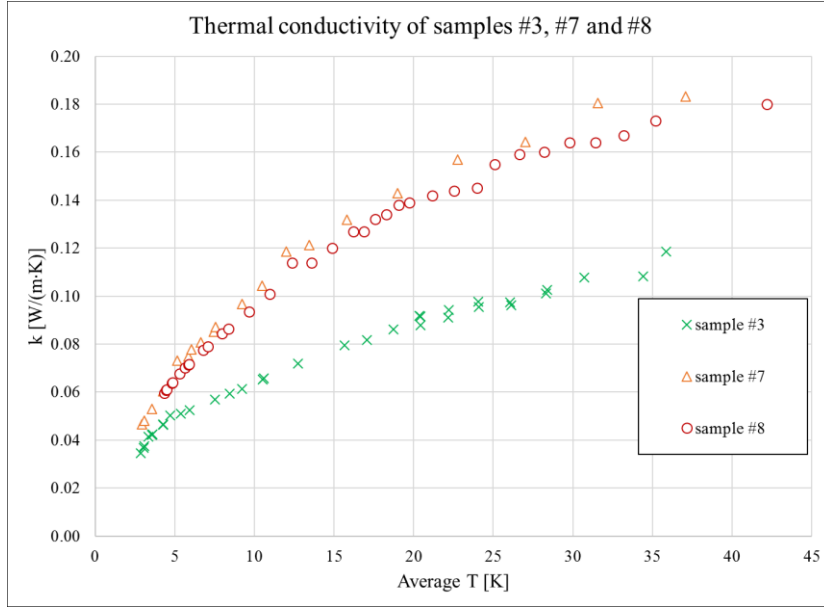


Figure 5.5: Thermal conductivity of samples #3, #7 and #8 as a function of temperature.

The total measured thermal resistance R_{tot} of a sample can be written as follows:

$$R_{\text{tot}} = R_{\text{bulk}} + 2R_{\text{int}} \quad (5.1)$$

where R_{bulk} is the resistance of the bulk material (i.e. the resin-impregnated glass fiber) and $2R_{\text{int}}$ the resistance of the two copper-to-resin interfaces. The bulk resistance is considered a function of both temperature and active length ($R_{\text{bulk}} = R_{\text{bulk}}(T, L)$), while the interface resistances was considered the same whichever the sample length and a function of temperature only ($R_{\text{int}} = R_{\text{int}}(T)$).

The total thermal resistance R_{tot} as a function of sample length can be represented as:

$$R_{\text{tot}} = R_{\text{bulk}}L + 2R_{\text{int}} \quad (5.2)$$

R_{tot} for samples #3 and #8 was directly obtained from measurements of thermal conductivity ($R_{\text{tot}} = L/k$) and plotted as shown in figure 5.6. The constant term $2R_{\text{int}}$, whose values are listed in Table 5.3, was extracted from the linear fits of curves $R_{\text{tot}}(L)$, and plotted in Figure 5.7. The thermal interface resistance increases with decreasing of temperature in the range between 5 K and 35 K.

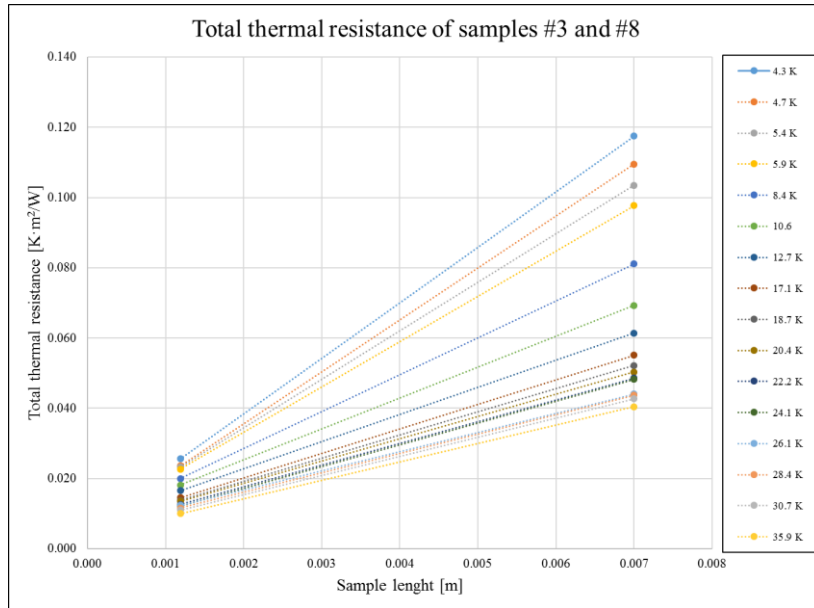


Figure 5.6: Total thermal resistance of samples #3 and #8 as a function of sample length for different temperatures.

Table 5.3: Interface resistance $2R_{int}$.

Temperature [K]	$2R_{int}$ [K·m ² /W]
4.3	0.0068
4.7	0.0060
5.4	0.0068
5.9	0.0073
8.4	0.0075
10.6	0.0077
12.7	0.0074
17.1	0.0063
18.7	0.0060
20.4	0.0060
22.2	0.0052
24.1	0.0048
26.1	0.0059
28.4	0.0050
30.7	0.0046
35.9	0.0038

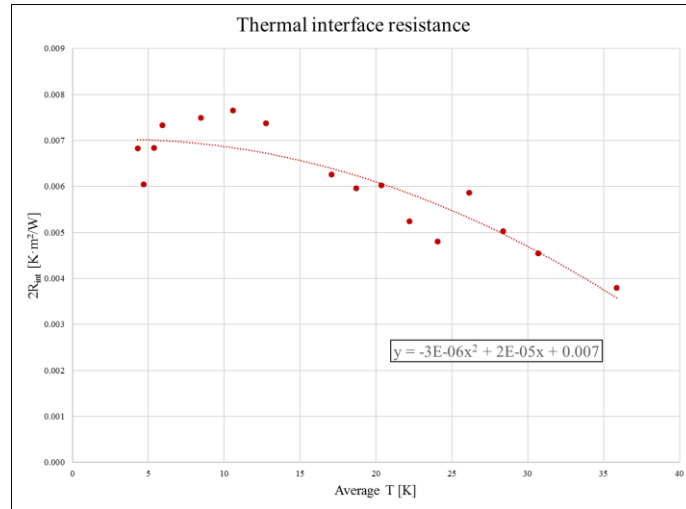


Figure 5.7: Total contact resistance of interfaces copper-to-sample.

Since with this procedure we obtained the value of thermal contact resistance of interfaces copper-to-sample, we can subtract this value from the total resistance one in order to obtain the resistance value of the bulk material, free of the influence of interfaces to copper parts. Results of thermal contact resistance were fitted as function of temperature and the resistance of the bulk material was calculated as follows:

$$R_{\text{bulk}}(T) = R_{\text{tot}}(T) - 2R_{\text{int}}(T) \quad (5.3)$$

From $R_{\text{bulk}}(T)$ results, we calculated for the three samples (#3, #7 and #8) the thermal conductivity corrected for the interfaces, i.e. of the bulk resin materials. Results of corrected thermal conductivity, i.e. free of the influence of interfaces, for the three samples as function of temperature are reported in figure 5.8.

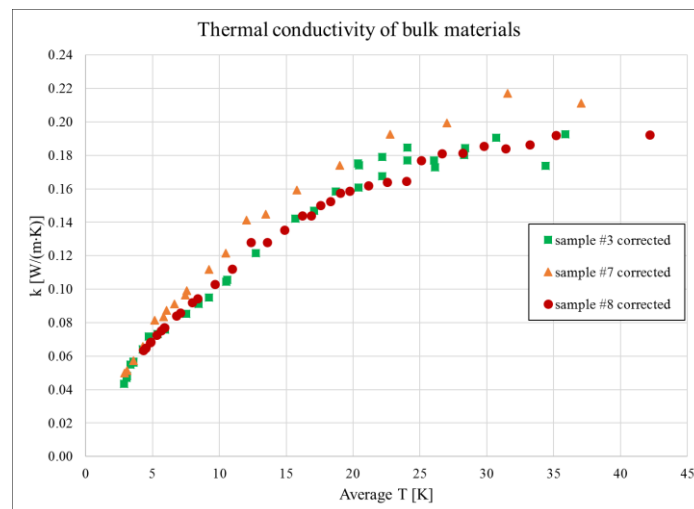


Figure 5.8: Thermal conductivity of samples #3, #7 and #8 as a function of temperature, corrected for the interfaces, i.e. of the bulk resin.

5.1.2 Epoxy resin thermal conductivity

Figure 5.9 compares the measured thermal conductivity of samples #1, #1 corrected and #2 to the epoxy resin thermal conductivity from CryoComp database. A good agreement was found with sample #1.

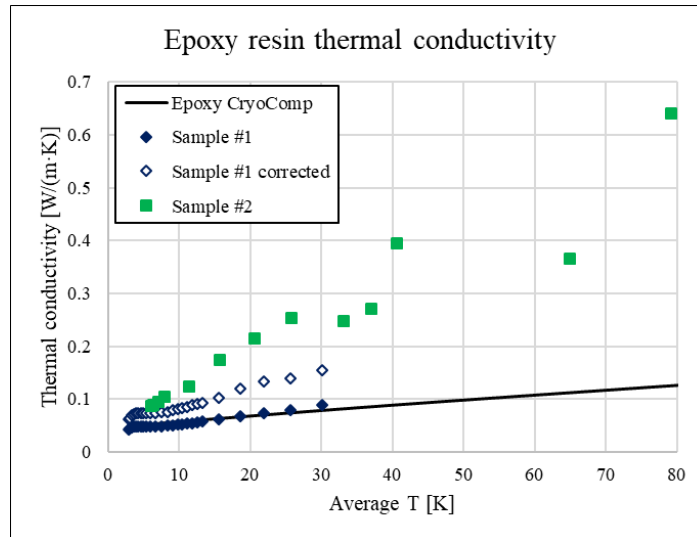


Figure 5.9: Comparison between Epoxy thermal conductivity [CRYO] and thermal conductivity of Sample #1, Sample #1 corrected and Sample #2.

5.1.3 Impregnated S2-glass thermal conductivity

Figure 5.10 compares the measured thermal conductivity of samples #3, #7 and #8 corrected to the G10 thermal conductivity in the transverse direction using NIST database. A good agreement was found between the corrected thermal conductivity curves of the samples and G10.

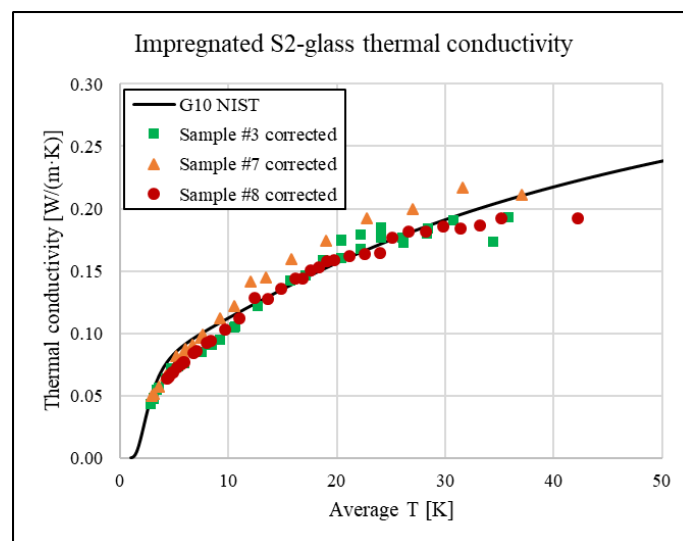


Figure 5.10: Comparison between G10 thermal conductivity [NIST] and thermal conductivity of Sample #3, #7 and #8 corrected.

5.1.4 Impregnated S2-glass with binder thermal conductivity

Figure 5.11 shows the comparison between the thermal conductivity of samples #3, #3 corrected, #4, #4 corrected and the thermal conductivity of G10 in the transverse direction using NIST database. The curve of G10 thermal conductivity approaches the curve of sample #3 corrected.

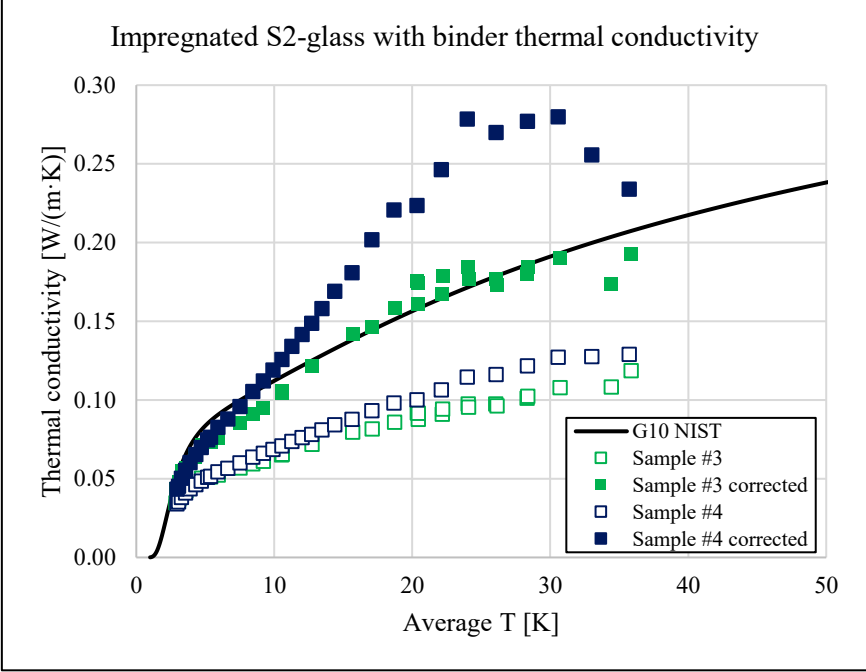


Figure 5.11: Comparison between G10 thermal conductivity [NIST]

5.1.5 Impregnated S2-glass-mica with binder thermal conductivity

The 11 T cable insulation consists of a C-shaped mica foil folded around the cable, and braided S-2 11-TEX glass fibre, with a target insulation thickness of 100 μm . Figure 5.12 shows a schematic view of the cable insulation layout. The main technical characteristics of the mica tape are summarized in table 5.4.

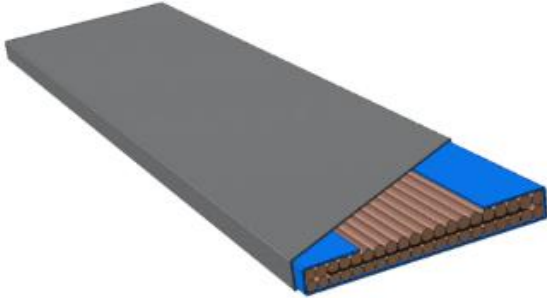


Figure 5.12: Schematic view of the cable insulation layout [MICA].

Table 5.4: Characteristics of the mica sheets in 11 T (COGEBI FIROX[®] P 63P24A) [MICA]

	63P24A
Nominal thickness [mm]	0.080±0.015
Total substance [g/m ²]	91-105
Mica content [g/m ²]	63±4
Glass content [g/m ²]	24±3
Bond content [g/m ²]	9-13
Tensile strength [N/cm]	>60
Stiffness [N/m]	<35
Dielectric constant 200 °C [-]	1.2
Dielectric strength [KV/layer]	>10
Thermal conductivity [W/(m·°C)]	0.20-0.25

Sample #5 was produced piling up several layers of S2-glass and mica tape, in order to have an insulation layout as close as possible to the 11 T case. Figure 5.13 compares the measured thermal conductivity with samples investigated by A. den Ouden et al. [Oud1994] consisting of different combination of mica/glass and glass sheet, whose main characteristics are reported in table 5.5. 11 T measurements are close to GM samples, where the mica-glass layers have not been heat treated. The effect of the thermal contact resistance between the sample and the sample holder is not treated in [Oud1994], so the different thickness of samples GM and GMHT might have an impact on the measured thermal conductivity. Finally, thermal conductivity of sample #5 corrected, which contains S-2 glass and mica sheets, is lower of 40% than the G10 one.

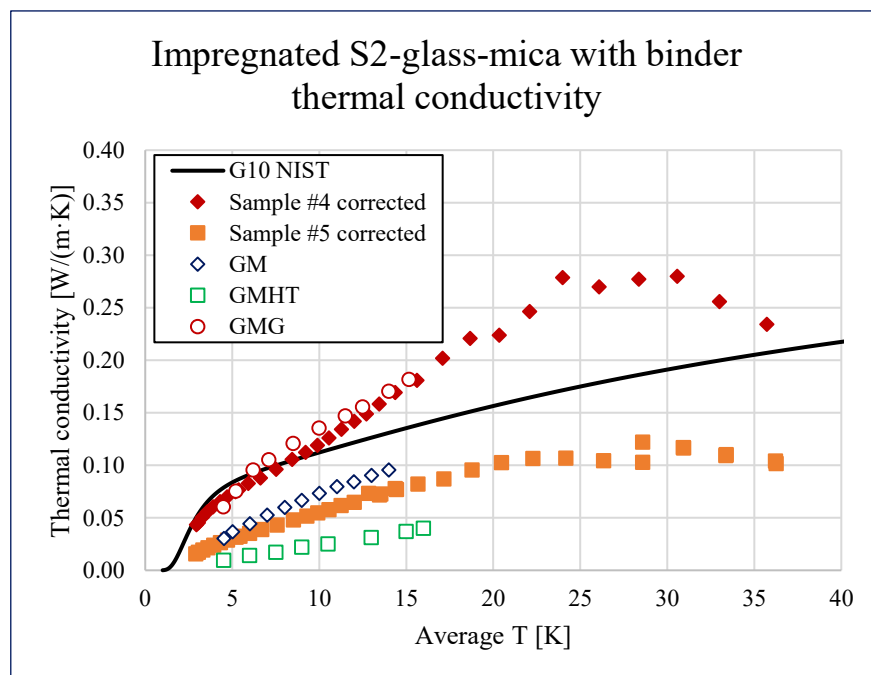


Figure 5.13: Thermal conductivity of the G10 as a function of temperature compared with thermal conductivity of samples #4 corrected, #5 corrected, and mica-glass/glass sheets samples.

Table 5.5: Composition of samples investigate by A. den Ouden et al. [Oud1994].

Sample	Type	Heat treated at 948.15 K
GM	12 layers mica/glass	no
GMG	6 layers mica/glass – 6 layers glass	no
GMHT	32 layers mica/glass	yes

The thermal conductivity of the mica tape can be derived from sample #4 and sample #5 measurements. The total thermal resistance $R_{\text{tot}(\#5)}$ of sample #5 can be written as the sum of the resistance of S-2 glass $R_{S-2(\#5)}$ (calculated from sample #4) and the resistance of mica R_{mica} :

$$R_{\text{tot}(\#5)} = R_{S-2(\#5)} + R_{\text{mica}} \quad (5.4)$$

According to (5.4) is possible to calculate the thermal resistance of mica and consequently its thermal conductivity. The resulting thermal conductivity of mica is shown in figure 5.14.

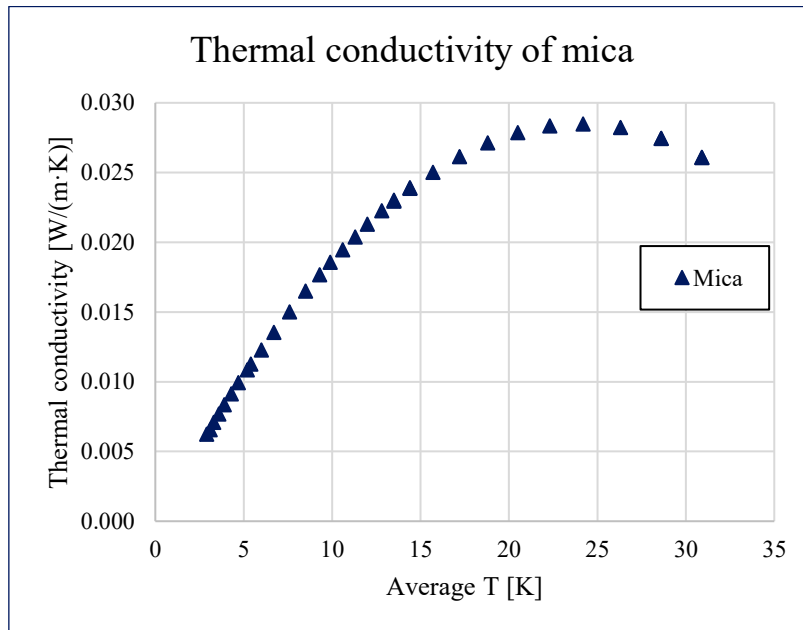


Figure 5.14: Thermal conductivity of mica.

5.2 Thermal conductivity measurements of coil segments and cable stacks components

Thermal properties of materials composing the coils have been recently measured at CERN Cryolab [CERN]. A total of three samples have been measured. The first two samples corre-

spend to coil segments extracted from 11 T practice coil 104 [Sar2015], which follow the standard 11 T manufacturing process. The conductor of this coil was RRP 54/61, and it is very different from the final layout (RRP 108/127). Coil sample #1 corresponds to a cut in the radial direction, coil sample #2 to a cut in the azimuthal direction (see figure 5.15). The third sample (coil sample #3) is composed of 10 stacked cables, cured, reacted and impregnated following the 11 T manufacturing process. Table 6 summarizes the main characteristics of the coil samples.

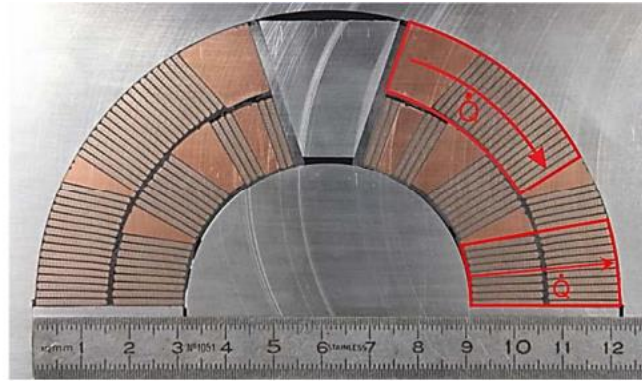


Figure 5.14: Picture of the 11 T dipole impregnated coil sample [Koe2017]. Coil sample #1 (down) and coil sample #2 (up) are indicated in red with indication of applied heat flow.

Table 5.6: Main characteristics of coil samples.

Coil sample	Type	Resin type	Insulation	Binder	Reacted?
#1	Coil, radial	CTD-101K	S-2 glass 636 11 TEX + mica	CTD-1202	yes
#2	Coil, azimuthal	CTD-101K	S-2 glass 636 11 TEX + mica	CTD-1202	yes
#3	Ten stacks	CTD-101K	S-2 glass 636 11 TEX + mica	CTD-1202	yes

Coil segments are glued to OFHC copper blocks. Finally, two electric heaters are mounted on the lower copper block of the sample [Koe2017]. Figure 5.15 shows a schematic representation of the samples, while their characteristic dimensions are listed in table 5.7.

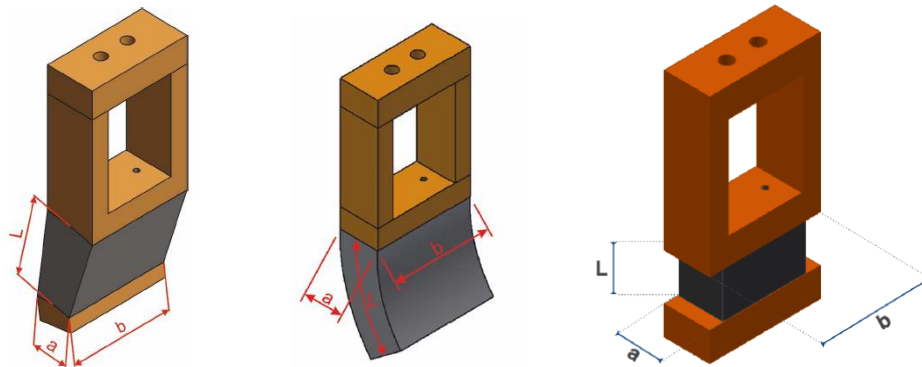


Figure 5.15: Schematic view of the coil samples. From left to right: coil sample #1, coil sample #2 and coil sample #3 [Koe2017, Borg2016].

Table 5.7: Main dimensions of the samples [Koe2017, Borg2016].

Parameter	Unit	Coil sample 1	Coil sample 2	Coil sample 3
a	[mm]	15.26	15.26	15.26
b	[mm]	40.30	40.30	29.07
L	[mm]	38.00	25.20	15.55
$A = a \times b$	[mm ²]	614.95	614.95	443.61

Figure 5.16 shows a picture of an unreacted Nb₃Sn cable of the sample, whose main parameters are reported in table 5.8.

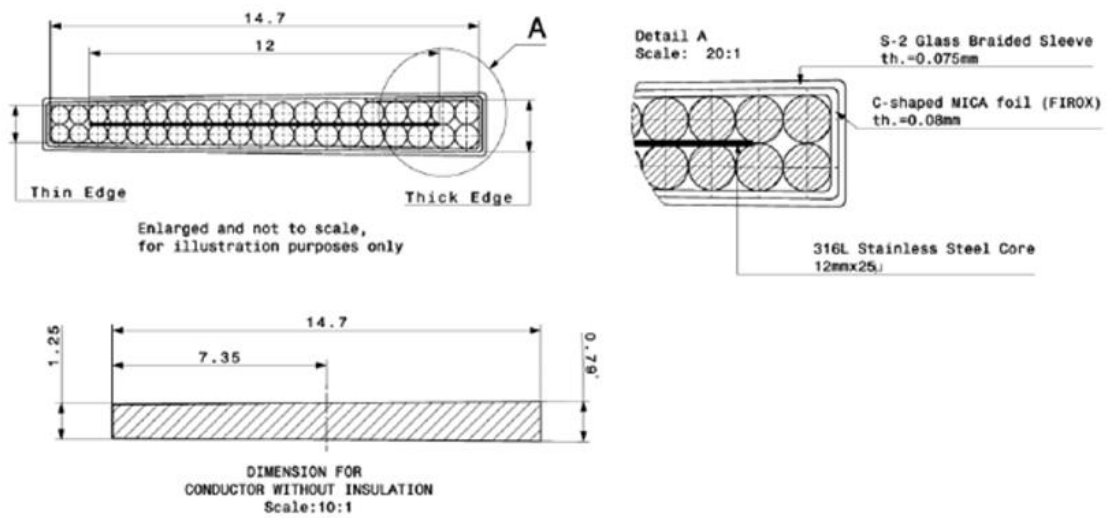


Figure 5.16: Schematic picture of an unreacted Nb₃Sn cable. Not in scale [CERNA].

Table 5.8: Main parameters of 11 T Nb₃Sn cable [CERNA].

Parameter	Unit	Value
Number of strands	[-]	40 (2 x 20)
Strand diameter	[mm]	0.70
Cu/non-Cu	[-]	1.15
Strand area	[mm ²]	0.38
SC strand area	[mm ²]	0.18
Cable width before/after reaction	[mm]	14.70/14.85
Bare cable mid-thickness before/after reaction	[mm]	1.25/1.307
Keystone angle	[deg]	0.79
Total insulation thickness at 5 MPa	[mm]	0.135
Nominal insulation thickness	[mm]	0.10
Mica layer thickness at 5 MPa	[mm]	0.05
Nominal mica layer thickness	[mm]	0.08
Transposition pitch	[mm]	100.00

5.2.1 Steady-state measurement method

The measurement methodology, described in detail in [Borg2016], is briefly presented here with reference to sample #3. The thermal conductivity measurements of the sample were performed in the temperature range from 5 K – 100 K using a steady-state method [Imb2003, Borg2016], which is described below.

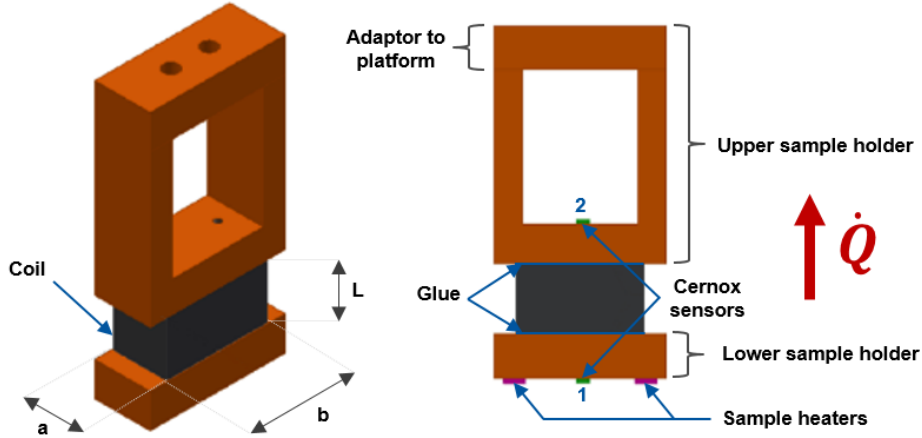


Figure 5.17: Sample holder and characteristic dimensions of the sample [Borg2016].

The sample is placed between two heat sinks: the cold sink is the upper sample holder that is in direct contact with the cold measurement platform, while the warm sink is the lower sample holder that is heated through the heaters. Sample heaters generate a constant heat flux \dot{Q} in axial direction, as shown in figure 5.17, which in turn causes a temperature gradient ΔT along the active length L of the sample. The temperature gradient is measured through two sensors, which could be considered separated by the same distance L for the calculation of thermal conductivity; indeed, in case of these measurements, the temperature sensors are placed further apart than the active coil sample length L . However, this approximation does not affect measurements since the conductivity of the copper sample holders far exceeds that of the coil. The system is enclosed in a stainless-steel vacuum chamber to avoid convective losses. Radiative losses could be reduced through a gold plating treatment of the vacuum chamber [Imb2003].

Thermal conductivity can be obtained from Fourier's law in axial direction [Poi2016]:

$$\dot{Q} = -k \frac{\partial T}{\partial l} \quad (5.5)$$

where \dot{Q} represents the heat flux flowing in the sample, equal to the power density applied through the heaters but in opposite direction with respect to the temperature differential $\frac{\partial T}{\partial l}$, and k is the thermal conductivity which is temperature dependent. Considering the cross-sectional area A of the sample, and approximating k to be a linear function of temperature, sample thermal

conductivity k_{sample} (in $\text{W}/(\text{m}\cdot\text{K})$) was calculated at an average temperature $\bar{T} = \frac{T_1+T_2}{2}$ as follows [Imb2003]:

$$k_{\text{sample}}(\bar{T}) = \frac{PL}{A\Delta T} \quad (5.6)$$

where T_1 is the temperature recorded by *Cernox 1* sensor placed on the warm sink, T_2 is the temperature recorded by sensor *Cernox 2* placed on the cold sink, P (in W) is the power applied through the heaters, L (in m) the distance between the two temperature sensors, A (in m^2) the coil active area and ΔT (in K) is the absolute temperature gradient measured between the two temperature sensors. Considering the thermal conductivity as a linear function of temperature, results a good approximation for metals at low temperature. Since our measurements are performed at cryogenic temperatures, the error due to this approximation is small for temperature gradient of a few Kelvin [Imb2003].

The determination of the absolute temperature gradient ΔT is summarized in the following and schematized in figure 5.18. After an initial cooldown and stabilization of the coil sample down to the minimum reachable temperature (around 5 K), a fixed heating power P is applied by the sample heaters (instant t_0); as result, a temperature gradient ΔT_{ON} is generated between the two sensors and, after some time (t_1 to t_2) required for stabilization, is recorded. At instant t_2 the sample heaters are switched off, the sample cools down, and after stabilization (t_3 to t_4) the residual temperature gradient ΔT_{OFF} is recorded between the two sensors. The temperature gradient ΔT_{ON} is 200 mK to 500 mK higher than ΔT_{OFF} , and this value can be adjusted by changing the power applied to the heaters [Borg2016]. Finally, to eliminate possible errors in temperature calibration or parasitic heat loads, the temperature gradient ΔT , used in equation (5.6), is given by the following formula:

$$\Delta T = \Delta T_{ON} - \Delta T_{OFF} \quad (5.7)$$

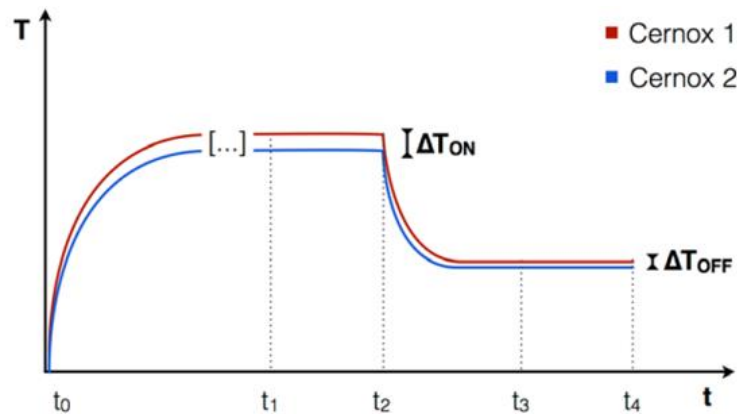


Figure 5.18: Schematized plot of the temperature gradient acquisition during a steady-state measurement of one data point [Borg2016].

Quasi steady-state measurements, which are not discussed in this thesis, have been also performed at Cryolab and widely discussed in [Borg2016]. Quasi steady-state method allows to acquire the measurement of one data point faster than steady-state method, although the accuracy of the measurement depends on the characteristics of the sample. Furthermore, one of the main disadvantages in using quasi steady-state method is the impossibility to measure the offset of the temperature gradient, that is the equivalent of ΔT_{OFF} for the static measurements [Borg2016].

5.2.2 Experimental setup description

The experimental setup for thermal conductivity measurements, described in detail in [Borg2016] and shown in figure 5.19, is briefly presented in this section. The experimental setup is mainly composed by a two-stage pulse refrigerator which provides up to 1 W of cooling power at 4.2 K. The so-called *1st stage* minimizes the heat load delivered by radiation to the *2nd stage* through an insulated polished copper thermal shield. The temperature of this stage is controlled by using electric heaters. The *2nd stage*, also called the *cold head*, is the coldest part of the refrigerator, and it is anchored with the measurement platform; this stage can reach a minimum temperature of 3.3 K, depending on parasitic heat loads. The measurement platform is used to control the sample temperature and instrumentation cabling through the heaters; it is directly connected to the cold head by means of G10 fiberglass plate to assure best thermal contact and perform measurements at higher temperatures. The measurement platform is provided by a copper thermal shield wrapped in multi-layer insulation to reduce heat inleaks to the sample. Finally, the sample holder is fixed to the measurement platform. It provides a mounting interface between the cold part of the instrumentation and the sample, and also it hosts the two temperature sensors (Cernox). An additional temperature sensor (TVO) is mounted on the sample adaptor to show the temperature of the measurement platform. Real pictures of samples are shown in figures 5.20-5.21

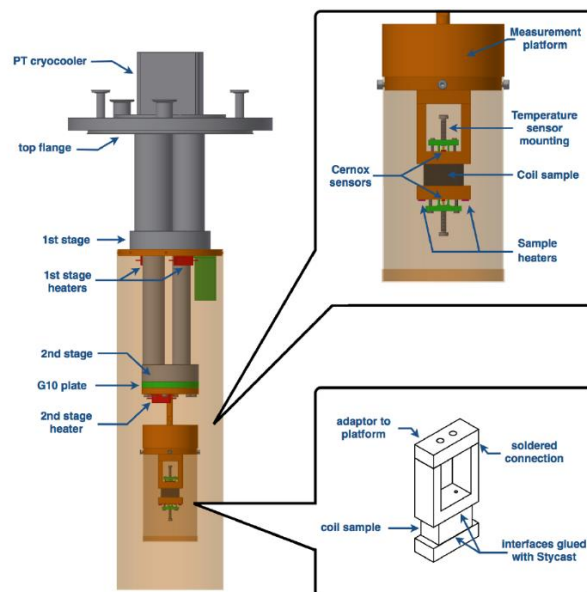


Figure 5.19: Schematized experimental setup for thermal conductivity measurements [Borg2016].

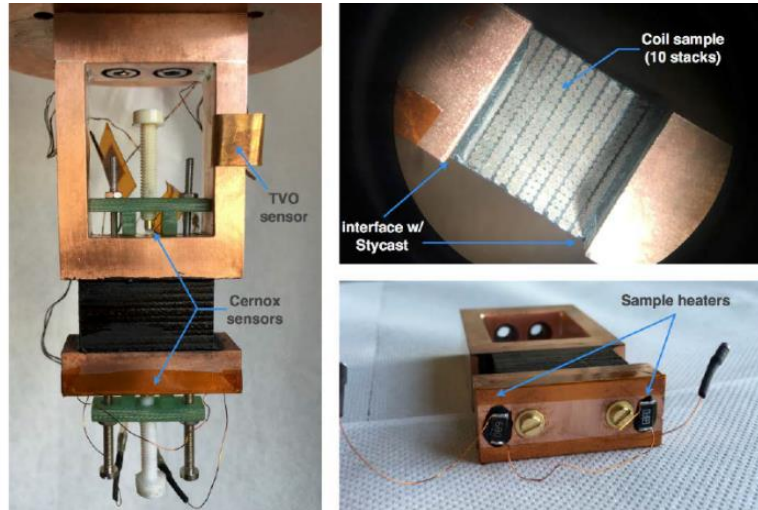


Figure 5.20: Coil sample #3 mounted in the adapter (left) and sample heaters (bottom right); enlargement on Nb₃Sn cable stacks [Borg2016].

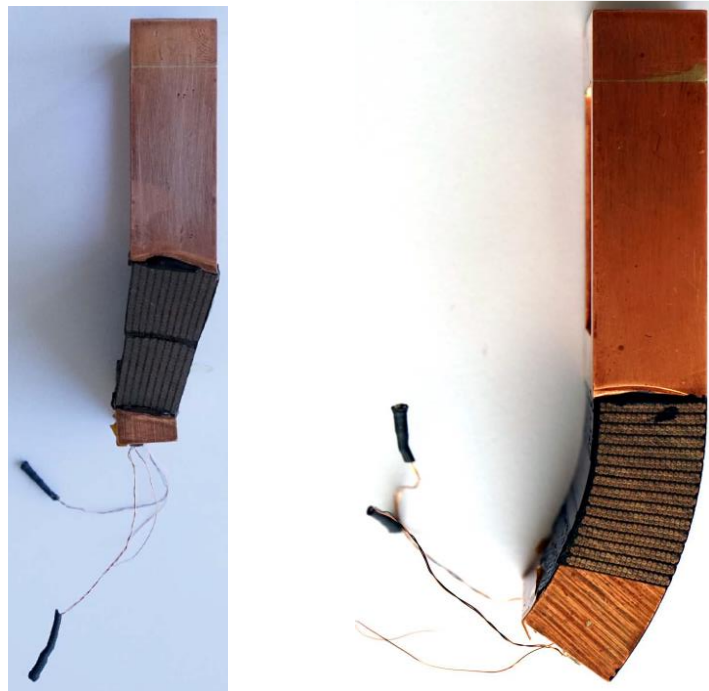


Figure 5.21: Coil sample #1 (left) and coil sample #2 sample heaters [CERNb].

5.2.3 Experimental results

Figure 5.22 shows the thermal conductivity k as a function of the average temperature T for the three coil sections. The relative measurement error varies from $\pm 4\%$ up to $\pm 8\%$ due to the different measurement ranges of data acquisition system. The error on the determination of the absolute temperature, due to the calibration of temperature sensors, is of ± 5 mK at 4.8 K and

± 165 mK at 100 K. The different coil samples are not directly comparable since coil sample #1 provides the coil thermal conductivity in the radial direction whereas coils sample #2 and #3 are in the azimuthal direction. Tables summarizing the experimental data are provided in Section 2 of Annex 2.

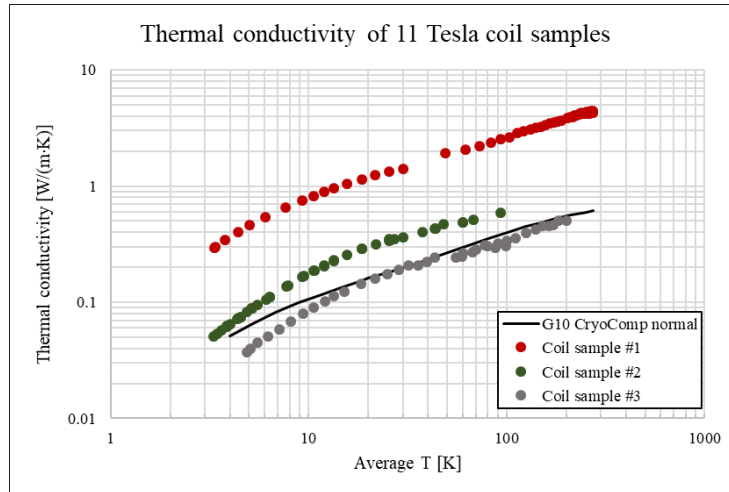


Figure 5.22: Coil samples #1, #2 and #3 thermal conductivity measurements compared with G10 thermal conductivity measured in normal direction.

Figure 5.23 shows the thermal conductivity of the coil samples in azimuthal direction and compare it with the thermal conductivity of G10. Results for coil sample #3 are very close to G10. This is not expected and will be further investigated in section 5.3, since the insulation in between cables is 0.2 mm. This represents 16% of the sample length; the rest is Nb₃Sn strands with thermal conductivity orders of magnitude higher. Thermal conductivity of coil sample #3 is 50 % higher. Visual inspection of the samples has been done (see figure 5.24), and the main difference among samples is that the insulation thickness in between two turns is 0.28 mm in coil sample #2 and 0.24 mm in coil sample #3.

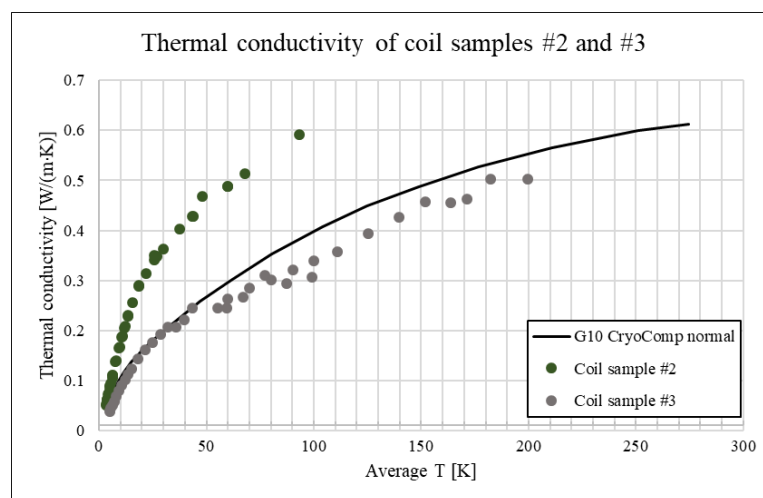


Figure 5.23: Coil samples #2 and #3 thermal conductivity measurements compared with G10 thermal conductivity measured in normal direction.

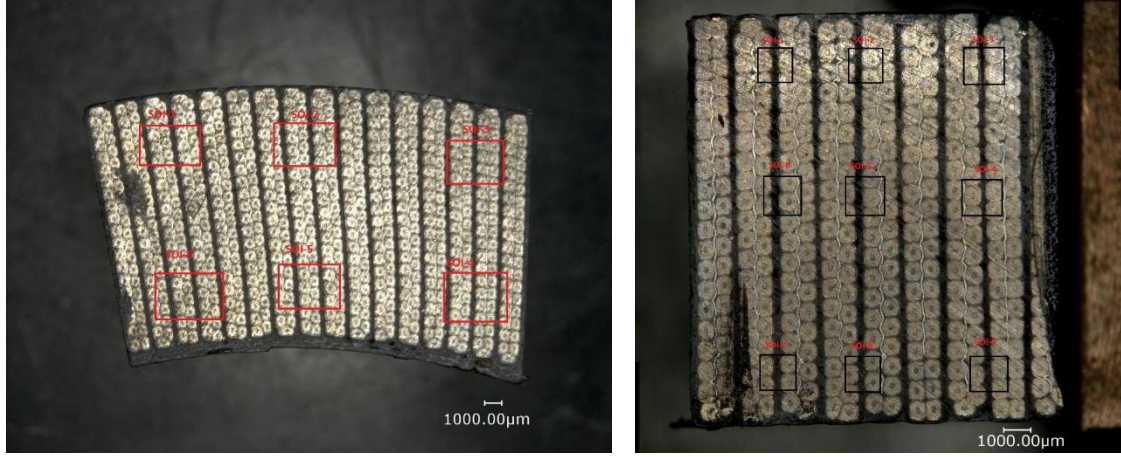


Figure 5.24: Visual inspection of the coil samples #2 (left) and #3 (right) [CERNb].

Assuming that the thermal resistance of the strands (Nb_3Sn and copper) is negligible with respect to the insulation, the thermal conductivity of the insulation can be derived from the coil measurements and compared to thermal conductivity measurement on single components described in section 5.1. The derived thermal conductivity of insulation was calculated for the three samples as follows:

$$k_{\text{ins,radial}} = \frac{k_{\text{sample}}(N_s(2t_{\text{ins}}) + t_{\text{int.layer}} + t_{\text{ins,OD}} + t_{\text{ins,ID}})}{L} \quad (5.8)$$

$$k_{\text{ins,azimuthal}} = 2t_{\text{ins}} \frac{k_{\text{sample}}N_s}{L} \quad (5.9)$$

$$k_{\text{ins,stacks}} = 2t_{\text{ins}} \frac{k_{\text{sample}}N_s}{L} \quad (5.10)$$

where t_{ins} is the insulation thickness of the cable, $t_{\text{int.layer}}$ the insulation thickness of the inter-layer (0.5 mm for the 11 T), $t_{\text{int.OD}}$ and $t_{\text{int.ID}}$ are respectively the insulation thickness of outer and inner diameter coil insulation (0.1 mm for the 11 T), k_{sample} the thermal conductivity of the sample, N_s the number of cables in the sample, and L the length of the coil sample. Figure 5.25 shows the derived thermal conductivity of the insulation for coil samples and compares it to G10. The very low thermal conductivity indicates that the approach used to derive the thermal conductivity of the insulation is not accurate enough. Section 5.3 discusses different elements that play a role on thermal conductivity of a coil sample in order to have a better interpretation of the experimental results.

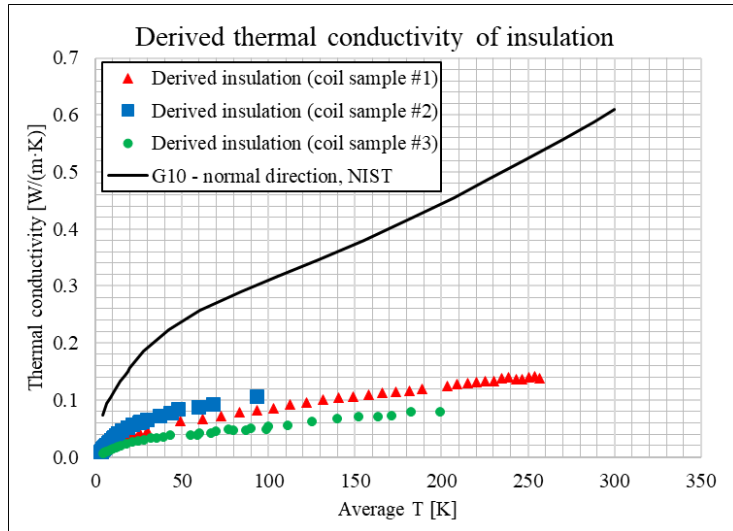


Figure 5.25: Derived thermal conductivity of insulation for coil samples.

Visual inspection in coil samples revealed a high concentration of voids in between the inner and outer layers for coil sample #1 (see figures 5.26 and 5.27). Assuming 20% of voids fraction in the coil-inter layer, measurements for coil sample #1 and coil sample #2 are consistent.

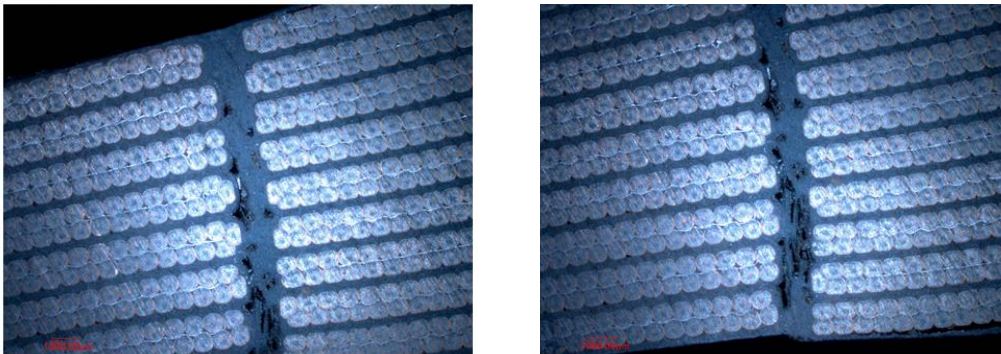


Figure 5.26: Visual inspection of coil sample #1: large voids were detected in inter layer region [CERNc].

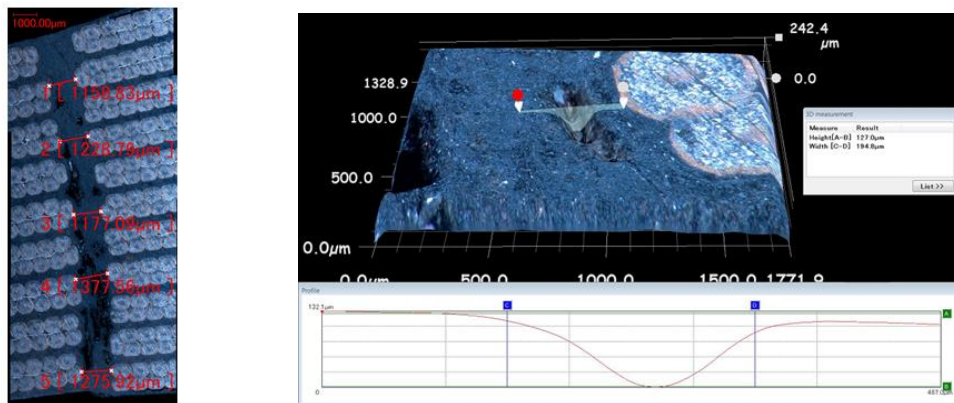


Figure 5.27: Visual inspection of coil sample #1 [CERNc].

5.3 Numerical model of Nb₃Sn cable stacks

Thermal design of Nb₃Sn cables needs to take into account the non-linear temperature dependence of material properties, as well as thermal contact resistance existing between contacting surfaces. The complexity of the problem calls for numerical computation. A FE model of 10 stack parallel sample, i.e., coil sample #3, was built-up in COMSOL Multiphysics[®] to numerically replicate the absolute steady-state measurement methodology used at CERN Cryolab [Borg2016], described in section 5.2, and assess the thermal conductivity of Nb₃Sn cable stacks in the range from 5 K to 100 K.

Simulations were carried-out in steady conditions to estimate the sample thermal maps, the temperature profile inside the cables, the heat flow path inside cable strands, and the effect of strand transposition and thermal contact resistance on thermal conductivity of the sample.

5.3.1 Model implementation

5.3.1.a Geometry of the numerical model

The 2-D geometry of the sample used in the simulations inclusive of a description of the components is shown on the right in figure 5.28. Values of geometrical parameters are listed in table 5.7 of Section 5.2.

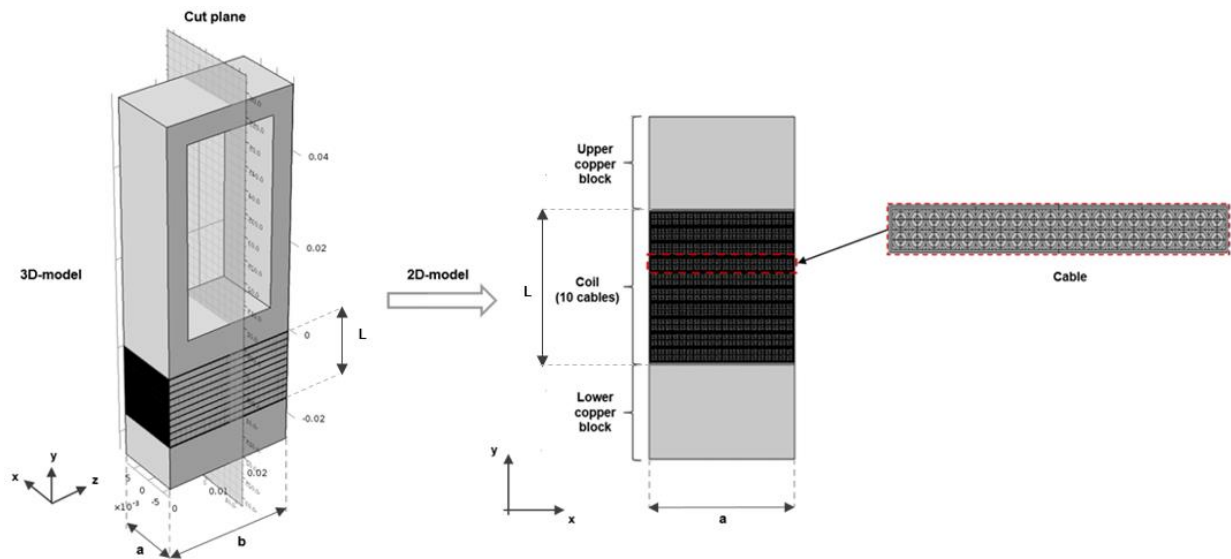


Figure 5.28: 3-D geometry (left) and 2-D geometry (right) of the numerical model.

The strategy of using a 2-D model represents in this case a good compromise between accuracy of results and computational time. We decided to model only the part between the two Cernox sensors; this is a good approximation, since the temperature along the upper block is uniform during the measurement process because of the high thermal conductivity of the copper.

The geometry was totally coded in COMSOL and consists in a sample of 10 Rutherford cables, of which a representation is shown in figure 5.29. Each cable consists of 40 strands which were simplified as concentric octagons [Val2018]. Each strand is composed of copper (yellow) and a region which contains the Nb₃Sn and the matrix (green). The cable is impregnated with CTD-101K epoxy (light blue), which fills the gaps between strands, and wrapped by an insulation layer of mica (red) and G10 (purple). A stainless-steel core (black) 25 μm thick was included in the geometry, despite its impact on the total thermal conductivity is negligible. Cable keystoneing was not taken into account in the geometry. Finally, the coil sample is placed in between two OFHC copper blocks (or sample holders), which are glued to the coil using a thin layer of high thermal conductivity epoxy resin (Stycast®).

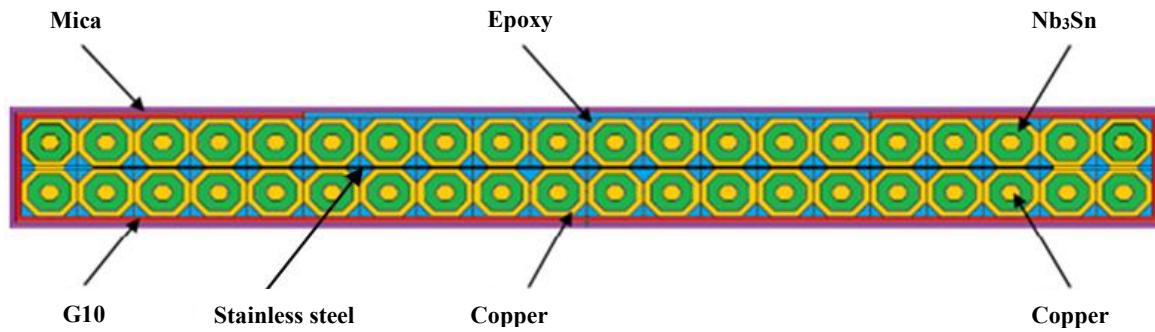


Figure 5.29: Geometry of the numerical model and enlargement on a cable.

The presented 2-D model is an approximation of a real Rutherford cable with unknown accuracy with respect to a general application. Indeed, the geometry does not consider the twist pitch of the cable, but strand transposition effect on total thermal conductivity was considered separately in a second analysis (see section 5.3.2). Finally, the effect of interstrand thermal contact resistance on overall thermal conductivity was considered invariant along the not-shown direction of the numerical model.

5.3.1.b Governing equation

In the first step of our investigation, labelled from now on *Case A*, thermal simulations were carried-out in steady conditions in order to determine the temperature distribution and consequently the transverse thermal conductivity of the sample. In this first case the strand transposition and interfacial thermal contact effect were not considered. The simulation consists in solving the two-dimensional heat balance equation under steady-state conditions:

$$\frac{\partial}{\partial x} \left(k \frac{\partial T}{\partial x} \right) + \frac{\partial}{\partial y} \left(k \frac{\partial T}{\partial y} \right) + \dot{Q} = 0 \quad (5.11)$$

where T (in K) is the temperature, k (in W/(m·K)) the thermal conductivity and the term \dot{Q} is the heat generation (in W/m²). In all simulations, values of thermal heat source correspond to the power provided by the heaters during the experimental tests. This power density is applied on the bottom surface of lower copper block, i.e., at $y=0$ (see figure 5.30). From simulations,

temperature gradient between the two sensors is acquired and the thermal conductivity of the sample is computed using equation (5.6) showed in section 5.2.1. Perfect thermal contact was in principle assumed at the interfaces between the different materials. Therefore, the temperature distribution is continuous and the equation to be solved is unchanged at the internal boundaries between materials. Results of this case study are reported in section 5.4.1.

5.3.1.c Boundary conditions

With reference to 2-D model represented in figure 5.30, adiabatic boundary conditions were set at $x=0$ and $x=a$:

$$k \left. \frac{\partial T}{\partial x} \right|_{x=0, x=a} = 0 \quad (5.12)$$

that is the heat flow in x -direction at $x=0$ and $x=a$ is zero, since the sample is placed in a vacuum chamber during the real experiment.

The temperature T_2 at the top of the system, i.e., at $y=L$, simulates the cold heat sink temperature T_{cold} . This temperature is maintained constant by a cryocooler to whom the upper surface of the sample is anchored. It is also the initial value of temperature assigned to all domains. The cold heat sink temperature T_{cold} changes during the different steady-state measurements of data points. The determination of T_{cold} temperature, and consequently of T_2 , was carried-out by using the approach described as follows.

Knowing from experimental tests the values of the power P (in W) and the experimental thermal conductivity k_{sample} (in W/(m·K)) (see table AS2.3 in Section 2 of Annex 2), the temperature gradient $\Delta T = T_1 - T_2$ between the two sensors can be calculated as:

$$\Delta T = \frac{PL}{Ak_{\text{sample}}} \quad (5.13)$$

where L (in m) is the distance between the two Cernox sensors, A the cross-sectional area of the sample (in m²), T_1 and T_2 (in K) respectively the temperature of sensors Cernox 1 and Cernox 2, placed in turn at the bottom and at the top of the model. Since we defined adiabatic conditions in our model, the residual heat load is basically zero, therefore in equation (5.7) we can consider ΔT_{OFF} negligible for our analyses. From the average temperature T_{ave} and temperature gradient ΔT , it is possible to calculate the temperature of the two sensors as follows:

$$T_1 = T_{\text{ave}} + \frac{\Delta T}{2} \quad (5.14)$$

$$T_2 = T_{\text{ave}} - \frac{\Delta T}{2} \quad (5.15)$$

Because of the high thermal conductivity of the upper copper sample holder, it follows with very good approximation:

$$T_{\text{cold}} \cong T_2 \quad (5.16)$$

i.e., the temperature T_2 recorded during the experiments in the Cernox 2 is almost equal to the temperature T_{cold} of the adaptor platform which is in direct contact with the cold part of measurement instrumentation. Boundary conditions used in simulations are summarized in figure 5.30.

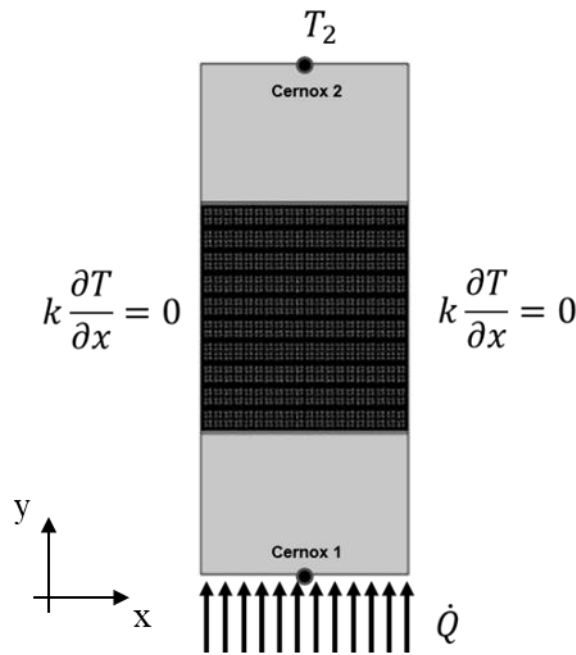


Figure 5.30: Boundary conditions of the numerical model.

5.3.1.d Material properties

Material properties were extracted from literature [CRYO, NIST, BNL] and coded in MATLAB following the NIST parametrization described in [Man2018]. Since the analyzed problem consists in heat transferring under steady-state conditions, the only physical property as a function of temperature required in the model is the thermal conductivity k (in $\text{W}/(\text{m}\cdot\text{K})$) for each considered material. Thermal conductivity curves as a function of temperature for materials used in the model are reported in figures 5.31-5.36.

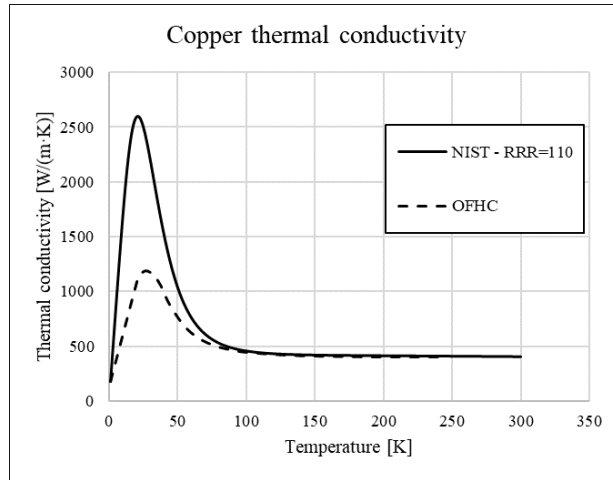


Figure 5.31: Thermal conductivity of copper (RRR=110) [NIST] and OFHC copper [BNL].

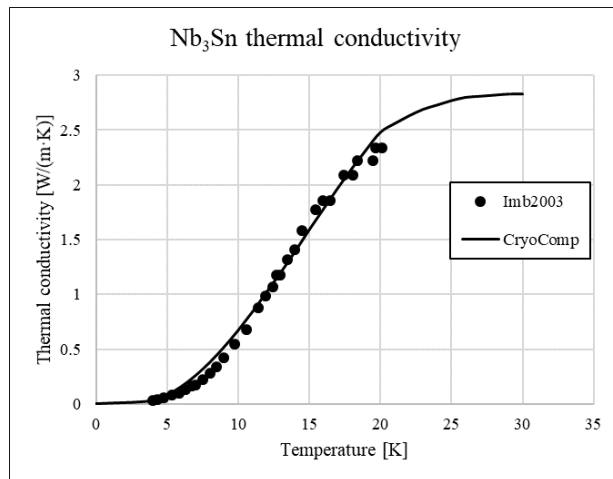


Figure 5.32: Nb₃Sn thermal conductivity [CRYO, Imb2003].

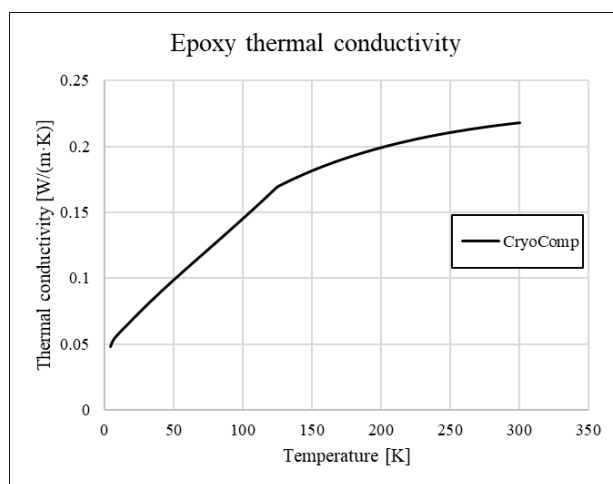


Figure 5.33: Epoxy thermal conductivity [CRYO].

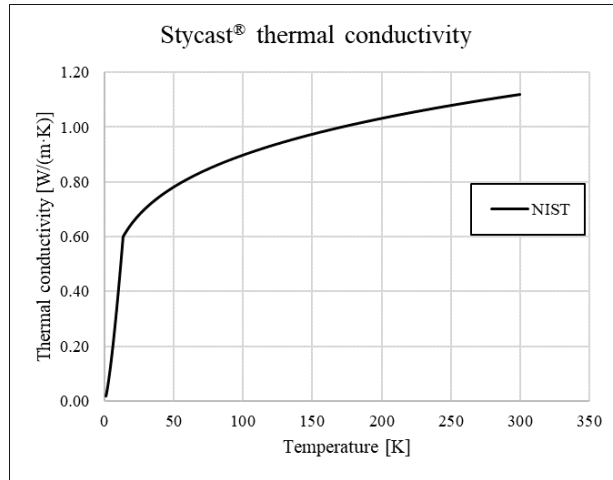


Figure 5.34: Stycast® thermal conductivity [NIST].

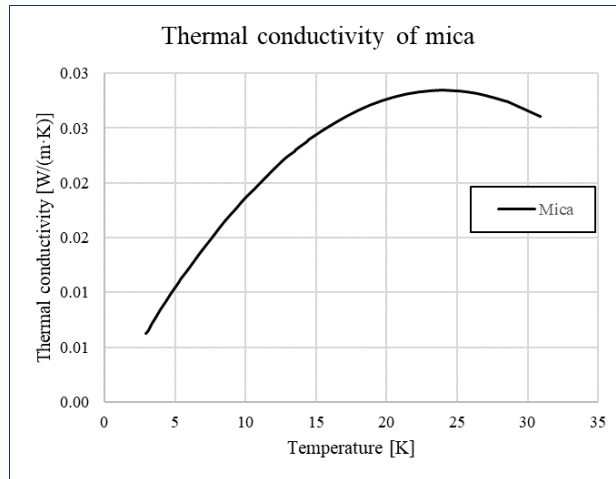


Figure 5.35: Mica thermal conductivity. Fit performed results obtained in section 5.1.5.

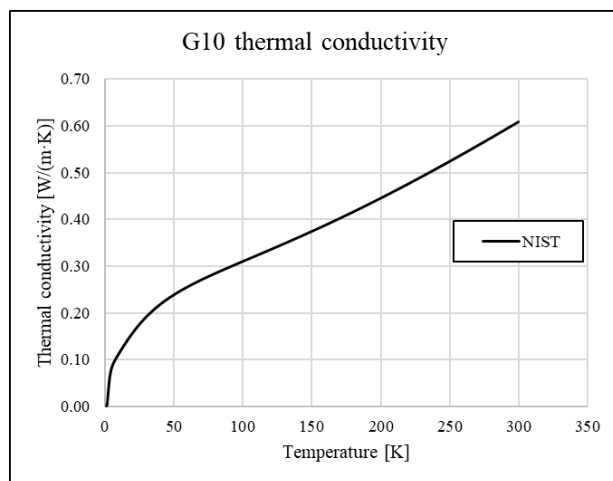


Figure 5.36: G10 thermal conductivity [NIST].

5.3.2 Strand transposition effect modelling

In the second step of our investigation, labelled from now on *Case B*, the effect of strand transposition on the transverse thermal conductivity was estimated, following the approach used in [Imb2003].

The thermal conductivity along the strands $k_{\text{long}}(T)$ is given by:

$$k_{\text{long}}(T) = \sum_i k_{\text{long}}^i(T) \quad (5.17)$$

where the index i represents the different materials of the sample and $k_{\text{long}}^i(T) = f_i k_i(T)$ is the thermal conductivity contribution along the strands for each considered material. The term $f_i = \frac{A_i}{A_{\text{cable}}}$ represents the fraction of the different components over the cable cross-sectional area A_{cable} .

Heat flow involves only the region of strand transposition, if we assume uniform temperature on surfaces normal to the axial direction. This length L_{transp} is called transposition length and it is few millimeters [Imb2003]. If the sample were half pitch long, the contribution of the transposition effect k_{pitch} on the transverse thermal conductivity is given by:

$$k_{\text{pitch}}(T) = k_{\text{long}}(T) \frac{h_{\text{cable}}^2}{L_{\text{pitch}} L_{\text{transp}}} \quad (5.18)$$

where h_{cable} is the cable thickness, L_{pitch} the twist pitch length that represents the length over which the cable is transposed and L_{transp} the transposition length that is few millimeters. Since it is difficult to have an exact measure of L_{transp} , it was set at 5.3 mm and then used to fit the experimental data [Imb2003]. Figure 5.37 shows a schematic network of strands in a Rutherford cable in which the twist pitch length L_{pitch} and twisting angle φ are shown.

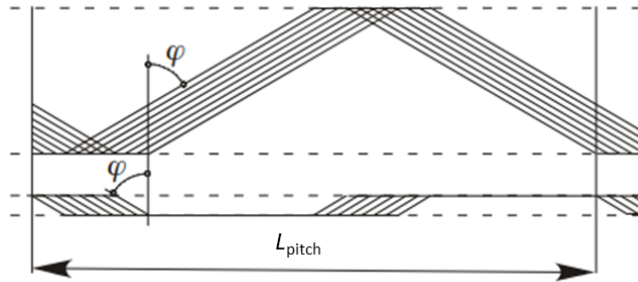


Figure 5.37: Schematic network of strands in a Rutherford cable. [Man2015].

The measured sample is shorter than half the twist pitch, therefore not all the strands are transposed from one layer to the other. The total transverse thermal conductivity of the sample $k_{\text{tot}}(T)$, which takes into account the effect of strand transposition, can be written as:

$$k_{\text{tot}}(T) = k_{\text{cable}}(T) + k_{\text{pitch}}(T) \frac{b}{L_{\text{pitch}}} \quad (5.19)$$

where $k_{\text{cable}}(T)$ is the computed thermal conductivity of coil sample #3 in *Case A* and b the length of the sample in z -direction. Results of *Case B* are reported in section 5.4.2.

5.3.3 Interfacial thermal contact resistance modelling

The final step of our investigation, labelled from now on *Case C*, was focused on the modelling of interfacial thermal contact resistance between cable strands, also called *interstrand thermal resistance* [Will2009]. This analysis was carried-out to obtain a more accurate evaluation of coil sample thermal conductivity. The evaluation of thermal contact resistance represents a key challenge because it is the primary factor limiting the heat transfer in many cryogenic applications [Zhe2016]. Consequently, the thermal conductivity of a cable in axial direction decreases significantly because of the thermal resistance due to the contact between the two layers of strands. However, the experimental characterization as well as the numerical modelling of the thermal contact resistance requires a large effort, principally because it depends strongly from surfaces characteristics and mechanical parameters hard to acquire. In addition, for copper, thermal resistance depends on the oxidation level [Imb2003].

Ideally, two surfaces are considered in “perfect” contact when each point of both surfaces is in contact along the entire nominal contact area. In reality, the actual contact area between two surfaces is not perfectly smooth and is considerably smaller than the corresponding nominal contact area. As consequence, the heat transfer across the strands layers takes place through surface-asperity micro-contacts and air-filled micro-gaps producing a significant thermal resistance, the so-called *thermal contact resistance*. The thermal contact resistance is principally governed by the effective roughness of the two surfaces in contact, the presence of interstitial gas and the contact pressure [Gru2005]. A schematic view of two materials in contact and inclusive of heat-flux lines is shown in figure 5.38.

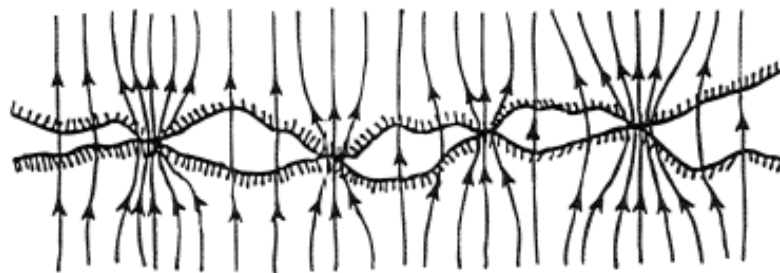


Figure 5.38: Schematic view of two materials in contact and heat-flux lines [THERM].

5.3.3.a Theory of thermal contact resistance

The thermal contact resistance R_{th} (in K/W) to which two surfaces in contacts are subjected is given by:

$$R_{th} = \frac{\Delta T}{P} = \frac{\Delta T}{\dot{Q}A_a} \quad (5.20)$$

where ΔT is the temperature drop over the interface, \dot{Q} (in W/m²) is the heat flux that crosses the joint and A_a (in m²) is the *apparent cross-section area* or nominal area [Mant2002]. The apparent contact area is the sum of the cross-sectional area where portions of both surfaces are in contact, the so-called *contact area* A_c , and the *void area* A_v where contact does not occur [Rem2011].

In literature [Mant2002], it is common referring to the *joint thermal contact conductance* h_j (in W/(m²·K)) instead of contact resistance:

$$h_j = \frac{1}{R_{th}A_a} \quad (5.21)$$

In addition, we can define the joint thermal contact conductance as the sum of three heat conductances in series as follows:

$$h_j = h_c + h_r + h_g \quad (5.22)$$

where h_c is the *contact conductance* which is referred to the thermal conduction between contacting surfaces of the two interface materials, h_r is the *radiative conductance* that governs the thermal radiation between the two materials, and h_g is the *gap conductance* that represents the conduction through air-filled micro-gaps between the two materials.

With reference to temperature range investigated for cable stacks thermal conductivity measurements (5 K to 100 K), conduction is the main mode of heat transfer through contact interfaces. Indeed, thermal radiation is insignificant under 873.15 K [Sav2003], and also natural convection is considered negligible if the thickness of interfacial gaps is less than 10 μ m [Gru2005]. Therefore, for our applications the joint thermal contact conductance can be assumed equal to the contact conductance, i.e.:

$$h_j = h_c \quad (5.23)$$

For this reason, the governing equation to be solved in this case is once again the two-dimensional heat balance equation under steady-conditions (5.11) used in solving *Case A*, plus

the equations used in COMSOL to model thermal contacts. Boundary conditions and applied heat source remain also the same used in *Case A*.

The theoretical model used in the numerical analysis to model the thermal contact resistance in cable stacks is the Cooper-Mikic-Yovanovic (CMY) plastic model [CMY1969, Gru2005, Zhe2016]. The CMY model proposes a relationship between main factors influencing thermal contact conductance, as follows:

$$\frac{h_c \sigma}{k_s m} \propto \frac{p}{H_c} \quad (5.24)$$

where, considering subscripts 1 and 2 referred to the upper and lower surfaces in contact:

- σ is the *effective RMS surface roughness* (in m) of the two surfaces, defined as:

$$\sigma = \sqrt{\sigma_1^2 + \sigma_2^2} \quad (5.25)$$

- m is the *effective mean absolute asperity slope* of surface profile, defined as:

$$m = \sqrt{m_1^2 + m_2^2} \quad (5.26)$$

- k_s is the *harmonic mean thermal conductivity* (in W/(m·K)) of the contact materials, defined as:

$$k_s = \frac{2k_1 k_2}{k_1 + k_2} \quad (5.27)$$

- p is the *contact pressure* (in Pa) between the contacting surfaces, which, together with the surface roughness, has a strong influence on the thermal contact conductance;
- H_c is the *surface microhardness* (in Pa), which influences the plastic deformation of the surface peaks of the softer material.

An illustration of two contacting surfaces showing the main geometrical parameters of CMY plastic model is shown in figure 5.39.

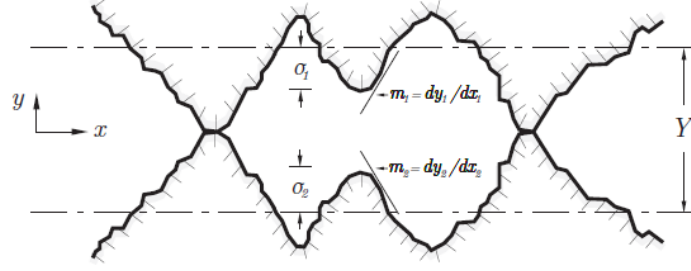


Figure 5.39: Schematic view of two materials in contact and CMY model geometrical parameters [Has2012].

In our model we assumed that, during the manufacturing process of cables, plastic deformations occur between surfaces in contact. The contact conductance was defined in the model using the Yovanovich correlation [Yov1982]:

$$h_c = 1.25 \frac{k_s m}{\sigma} \left(\frac{p}{H_c} \right)^{0.95} \quad (5.28)$$

This model is valid for the p/H_c range $[10^{-6}; 2.3 \cdot 10^{-2}]$ and, according to Sridhar and Yovanovich [Sri1994], it fits more closely experimental data in several experiments than other selected theoretical elastic and plastic models. Results of *Case C* are reported in section 5.4.3.

5.3.3.b Analogy between thermal and electrical contact resistance

As further step in our analysis, we analyzed the existing relationship between thermal contact resistance and electrical contact resistance in the contact region between the strands of a cable. To do that, we calculated for each cable the thermal contact resistance R_{th} (in K/W) as follows [Hyo2018]:

$$R_{th} = \frac{\Delta T}{P} \quad (5.29)$$

where ΔT [K] is the temperature gradient generated between the upper part and the lower part of the contact interface between strands due to the thermal contact resistance and P is a given power [W] that generates and heat flow passing through the interface. If we consider the contact between strands as a contact between metal materials, i.e. stainless steel-copper contact, the thermal conductivity becomes proportional to electrical conductivity, and this relationship is explained by the Wiedemann-Franz law [Hyo2018]:

$$\frac{k}{\gamma_c T} = 2.45 \cdot 10^{-8} \quad (5.30)$$

where k (in $W/(m \cdot K)$) is the thermal conductivity, γ_c [$\Omega^{-1}m^{-1}$] is the electric conductivity, T is the temperature of the metal and the value $2.45 \cdot 10^{-8}$ [$W\Omega K^{-2}$] is the *Lorentz number*. By changing the conductivities to the resistances and using the contact resistances, the equation 5.30 becomes:

$$\frac{R_{el}}{R_{th}T_{ct}} = \tilde{C} \quad (5.31)$$

where R_{el} is the electrical contact resistance (in Ω), R_{th} the thermal contact resistance, T_{ct} is the average temperature of the contact surfaces and the constant \tilde{C} is an experimental constant that, according to T. Hyodo et al. [Hyo2018], varies with contact pressure and surface roughness. Computing the thermal contact resistance from equation (5.29) and the average temperature of the contact surfaces from temperature distribution of finite element model, we finally calculated the electrical contact resistance for the interfaces between strands in cables of investigated coil sample #3. Results of this analysis are reported in section 5.4.4.

5.3.4 Numerical solution

Continuous equations were spatially discretized by a Finite Element approach based on the Galerkin method on non-uniform and non-structured computational grids made of free triangular elements. We preliminary studied the influence of spatial discretization in order to assure mesh-independent results. A computational grid made of about 17,087 elements was used for computations. The mesh presents a maximum relative error of 2% with respect to the finer grid used for the initial mesh test. Steady solutions of computed equations were performed by using an iterative dumped Newton-Raphson scheme [Hin2005] based on the discretized PDE linearization by a first-order Taylor expansion.

5.4 Results of thermal conductivity simulations on Nb₃Sn cables stacks

Simulations were carried-out for with different configurations (see table AS2.4 in Section 2 of Annex 2) in solving the heat transfer equation, in order to simulate thermal conductivity measurements performed at Cryolab on coil sample #3. The presented numerical procedure could be used for other coil samples. In the following we present an extract of obtained results.

5.4.1 Results of *Case A*: thermal conductivity of coil sample #3

The thermal distribution obtained for a steady simulation of the coil sample, when a power of $P=8.20E-5$ W is provided and the cold temperature T_2 is fixed at 4.85 K (test run #1 of table AS2.3), is shown in figure 5.40. In figure 5.41, the sample temperature profile as function of sample height is shown. In this case, the computed temperature gradient is 27.9 mK and the

overall thermal conductivity 0.105 W/(m·K). Changing in slope of temperature profile corresponds to the different thermal conductivity of sample materials: a reduction of temperature occurs in correspondence of insulating materials, i.e., G10, mica and epoxy layers.

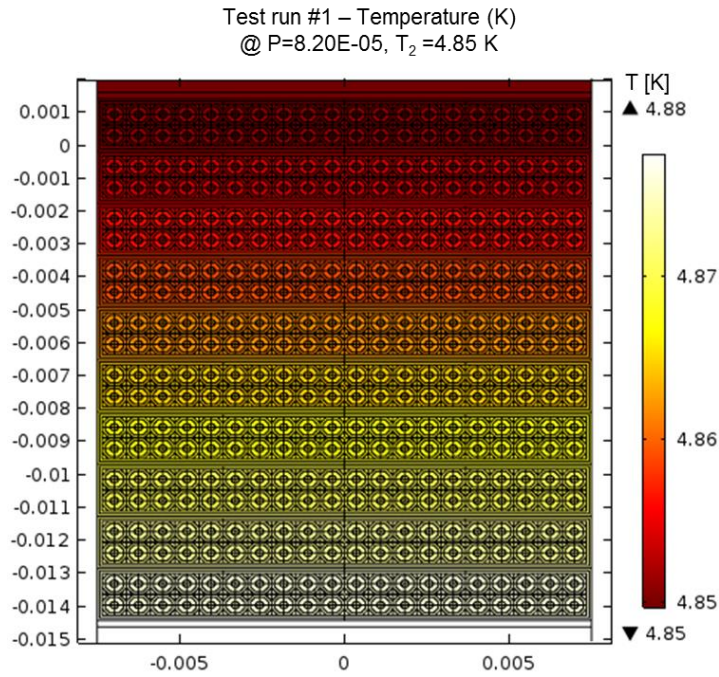


Figure 5.40: Thermal map of coil sample.

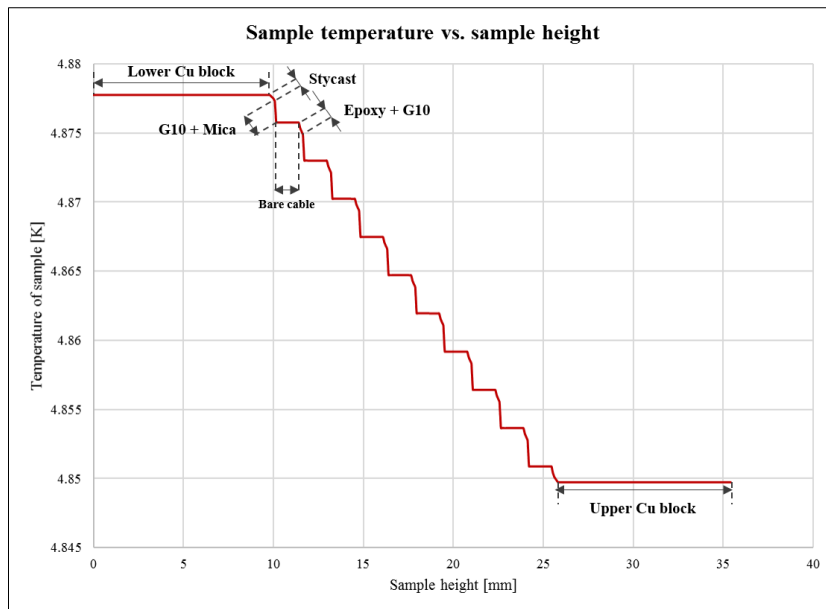


Figure 5.41: Temperature of sample vs. Sample height.

Thermal conductivity results from simulations for the analyzed sample compared with experimental data from CERN Cryolab are shown in figure 5.42. We performed in total 25 test runs with different values of cold temperature and applied power according to data listed in

table AS2.4 (see Section 2 of Annex 2). The obtained results show a trend similar to experimental one. However, a mismatch occurs below 40 K due to the thermal contact resistance between layers of cables, that was not considered in this first analysis. Results shows also that at very low temperatures thermal resistance is higher than higher temperatures.

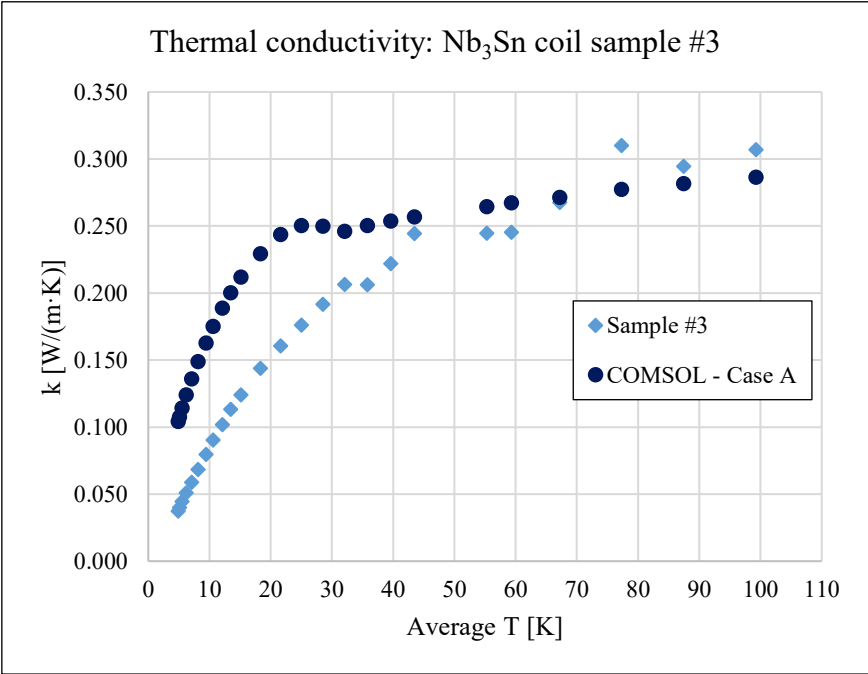


Figure 5.42: Comparison between experimental (light blue diamonds) and simulated (dark blue circles) thermal conductivity for sample #3.

To understand the impact of different insulating materials on the overall thermal conductivity of the sample, we compared the standard configuration of sample #3 (i.e., Glass+mica+SS in figure 5.43) with other two configurations: in one case, we used only G10, in another case we considered G10+mica as cable insulation. We did not consider the stainless-steel core in these two cases to see the also the impact of this layer on the thermal conductivity. Results reported in figure 5.43 confirm that thermal conductivity contribution of the stainless-steel core can be considered negligible. Furthermore, G10 configuration, i.e., only glass configuration, has total thermal conductivity 60% higher than the standard configuration of the sample #3.

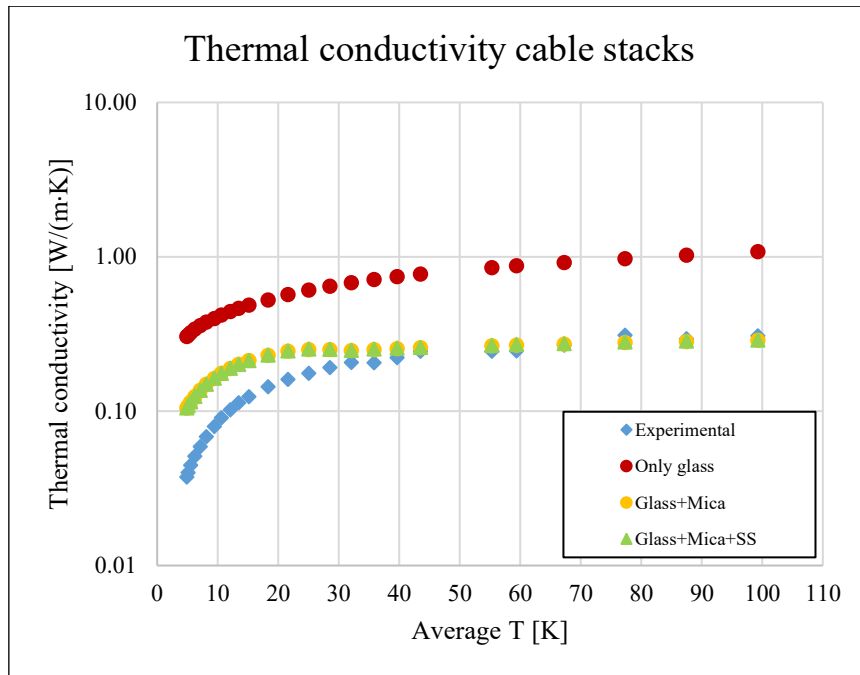


Figure 5.43: Comparison between experimental thermal conductivity of sample #3 (light blue diamonds) and different insulating configurations of the same sample.

Finally, figure 5.44 reports the total heat flux magnitude inclusive of heat streamlines inside cable strands. According to L. Imbasciati [Imb2003], the heat flux goes mainly through the copper layer that surrounds the superconducting core which have a much lower thermal conductivity.

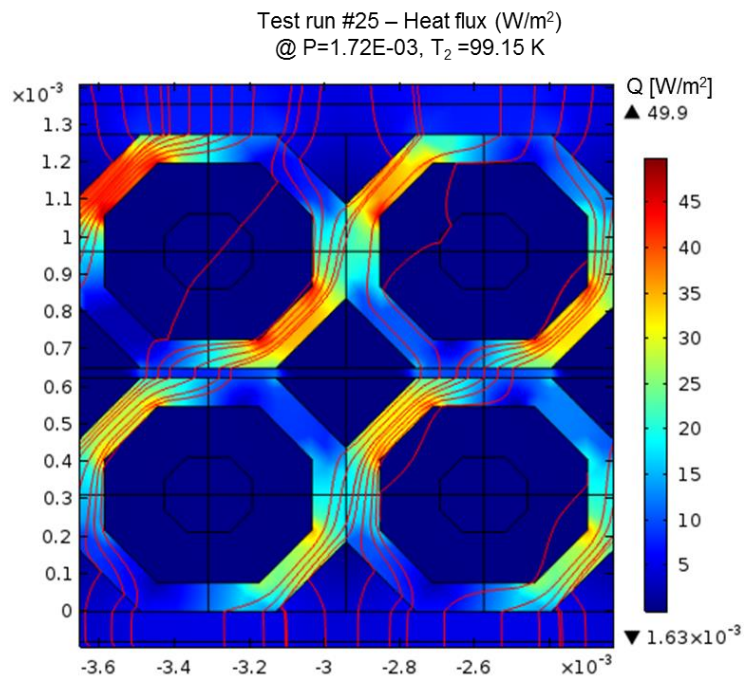


Figure 5.44: Heat flux magnitude and heat streamlines inside the strands.

5.4.2 Results of Case B: strand transposition effect on thermal conductivity of coil sample #3

The strand transposition effect on the thermal conductivity analysis of cable stacks was analyzed in the two following cases [Imb2003]:

- Homogeneous case ($b = L_{pitch}$): we consider the sample homogeneous. The heat source is uniform and heat flows involve only the region of the transposition of the strands, at the edge of the cable.
- Non-homogeneous case ($b < L_{pitch}$): we consider the sample as inhomogeneous. This case represents better the transient heat diffusion, like during a quench. As not all the strands are transposed, thermal gradient can establish within the planes normal to the axial direction.

Figure 5.45 shows the thermal conductivity curves for investigated cases compared to the experimental data. The dotted dark blue line represents the case that does not consider the transposition effect. The red continuous line and the dashed black line represent respectively the non-homogeneous and homogeneous studied cases. Finally, the light blue dash-dotted line represents the non-homogeneous case in which we consider $L_{transp} = L_{pitch}$; the thermal conductivity in this case is close to thermal conductivity curve of COMSOL model in which the transposition effect is not considered at all, and also to the experimental data.

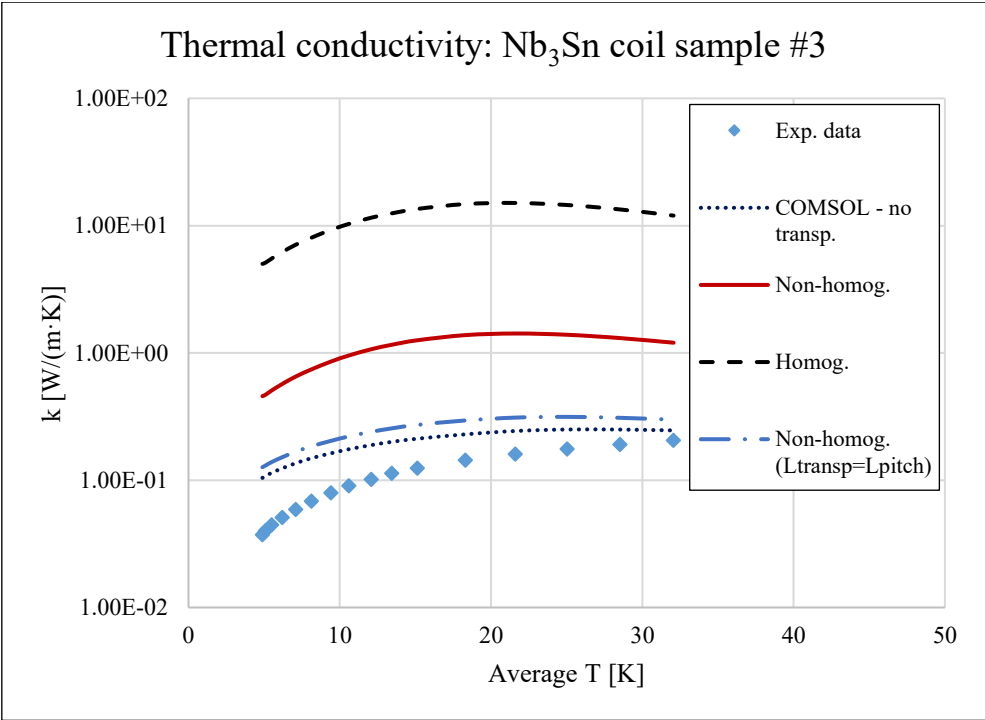


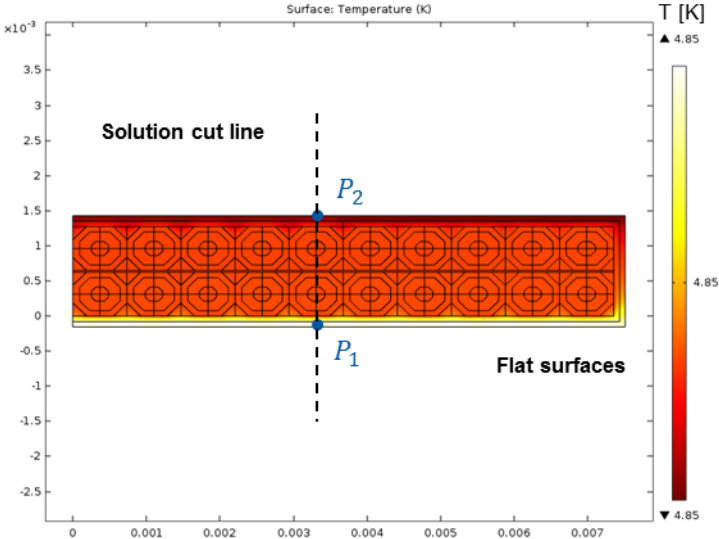
Figure 5.45: Sample #3 thermal conductivity data compared to COMSOL model and cases in which transposition effect was studied.

5.4.3 Results of Case C: effect of interstand thermal resistance on thermal conductivity of coil sample #3

The effect of interfacial thermal resistance on the overall thermal conductivity of the sample was studied at the interface between two adjacent strands, analyzing the Cu-SS and Cu-epoxy contacts. Since the experimental determination of the four CMY model parameters (the effective RMS surface roughness σ , the effective mean absolute asperity slope of surface profile m , the contact pressure p and the surface microhardness H_c) for each considered material requires a large effort, and also there are a lot of controversial ranges of values in literature [Gme1999], we decided to carry-out a sensitivity analysis on above-mentioned parameters to figure-out the parameters which affect more the interfacial thermal resistance phenomenon on cable stacks. From results, these parameters are the effective surface roughness and the contact pressure, as found also by M. Grujicic et al. in [Gru2005].

We chose for both investigated contacts mean values of m and H_c suggested by COMSOL software library for generic contacts, which are respectively 0.4 and 3 GPa. To assess the sensitivity of the thermal contact resistance to the variation of the two other parameters, i.e. σ and p , we varied the surface roughness in a range between 1.0 and 5.0 μm and the contact pressure in a range between 1 and 5 MPa.

Figures 5.46 shows the thermal behaviour comparison for one middle-cable of the sample between the cases in which flat surfaces (a) and thermal contacts are considered (b). Input parameters used in this case are: $P=8.20\text{E-}05\text{ W}$, $T_2=4.85\text{ K}$, $\sigma=2\text{ }\mu\text{m}$, $m=0.4$, $p=5\text{ MPa}$ and $H_c=3\text{ GPa}$. In figure 5.47, cable temperature profiles for the same cases are shown.



(a)

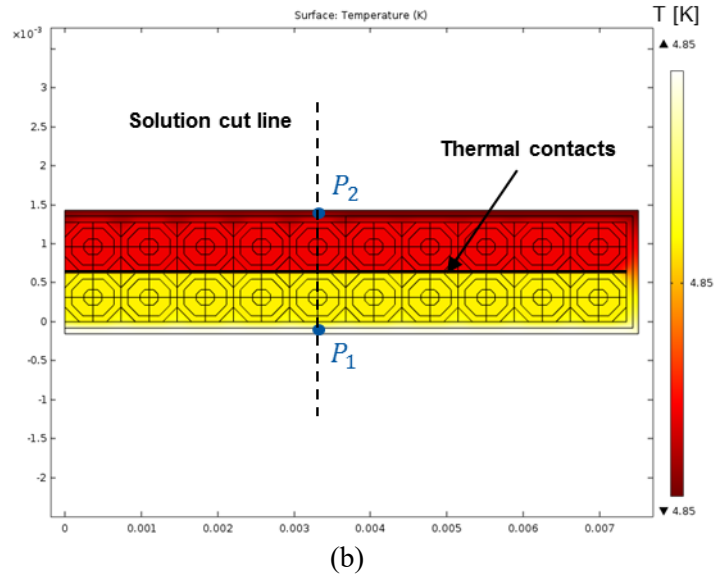
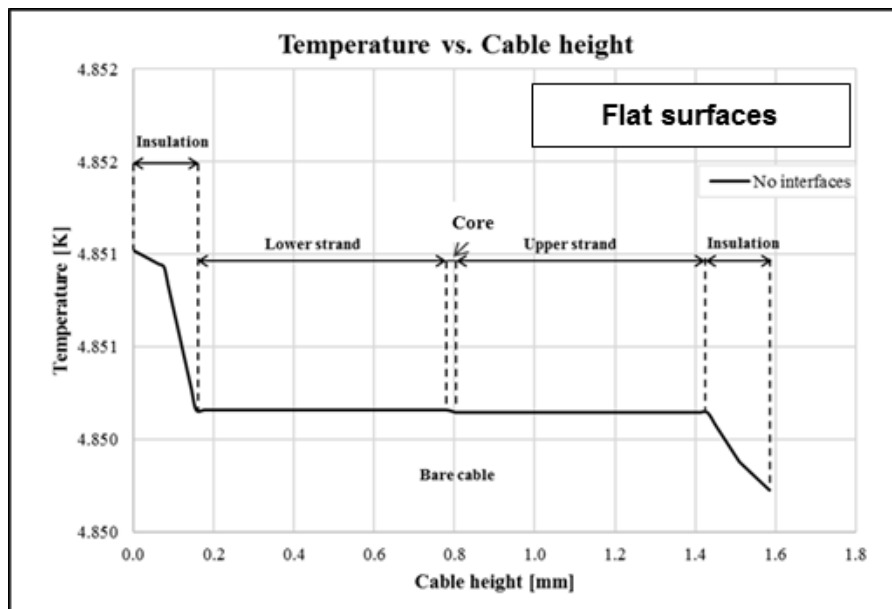
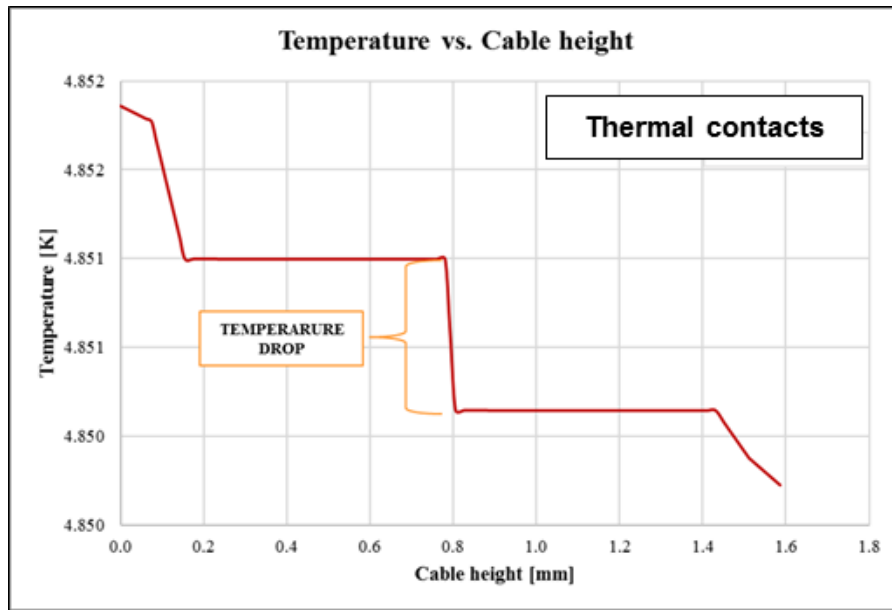


Figure 5.46: Middle-cable with flat surfaces (a) and modelled thermal contacts (b).

The thermal gradient between the bottom and top of the cable, i.e. the temperature difference measured between the two points P_1 and P_2 , increases by almost a factor two for the investigated case when we consider thermal contacts at the interface between strands. Indeed, the effect of interfaces manifests itself as a discontinuity in temperature gradient on a macroscopic scale, as shown in figure 5.47-b, and a constriction of the heat flow lines on a microscopic level (see figure 5.47-b).



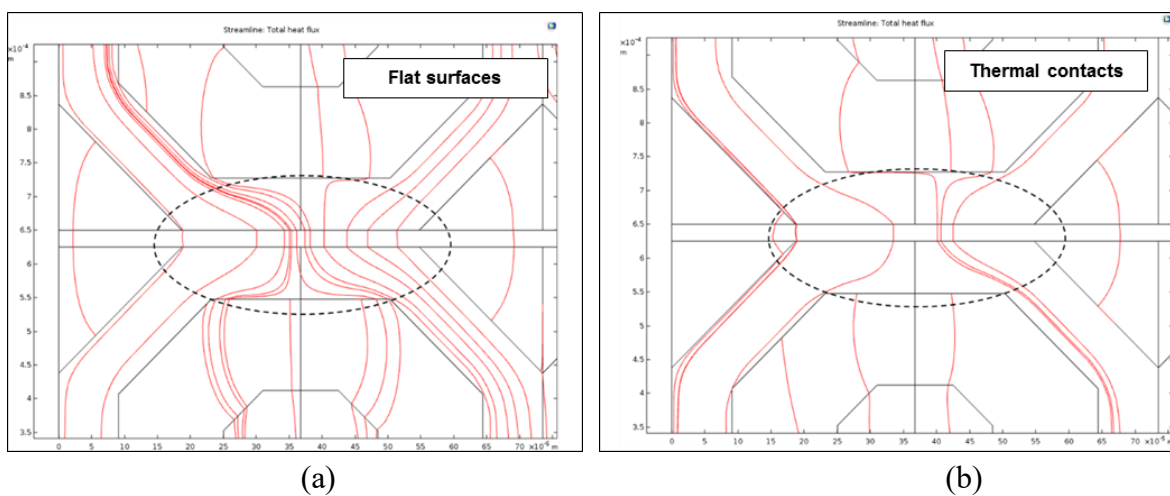
(a)



(b)

Figure 5.47: Cable temperature profile for flat surfaces (a) and with modelled thermal contacts (b).

Inserting thermal contacts in between the strands, the two surfaces touch at only a limited number of discrete points. Therefore, the heat flow between the two contacting surfaces is confined to limited areas and the heat transfer takes place through the surface asperities and air-filled micro-gaps, increasing the thermal resistance. Figure 5.48 shows the heat flux path close the interface zone in the two investigated cases (flat surfaces and thermal contacts). A lower number of heat flux lines per area (in red) pass through the interface when we consider no flat surfaces (figure 5.48-b). In presence of heat flow, interfaces produce a finite temperature drop which is proportional to the heat source applied to the model. As a consequence, the total thermal conductivity of the cable stacks decreases.



(a)

(b)

Figure 5.48: Heat flux path close to interface zone for flat surfaces (a) and with modelled thermal contacts (b).

Analyses to assess the sensitivity on thermal conductivity of the sample can be summarized as follows:

- In the first analysis, labelled from now on *Case C-1*, we kept constant the contact pressure at 5 MPa, changing the value of surface roughness in the range 1.0 to 5.0 μm .
- In the second analysis, labelled from now on *Case C-2*, we kept constant the surface roughness at 2.5 μm , which is the average surface roughness used in the previous case, changing the value of contact pressure in the range 1 to 3 MPa.

Results are plotted respectively in figures 5.49-5.50. Plots shows that the thermal conductivity increases with the increase of contact pressure while decreases with the increase of surface roughness as expected. This evidence is confirmed by results obtained by J. Zheng et al. in [Zhe2016]. Values of parameters that fit better in *Case C-1* the experimental data are a contact pressure of 5 MPa and a surface roughness of 4.0 μm . In *Case C-2*, the experimental data are well fitted by the curve obtained for a contact pressure of 3 MPa and a surface roughness of 2.5 μm . The Yovanovich correlation was found to be qualitatively and quantitatively in good agreement with experimental results for sample #3.

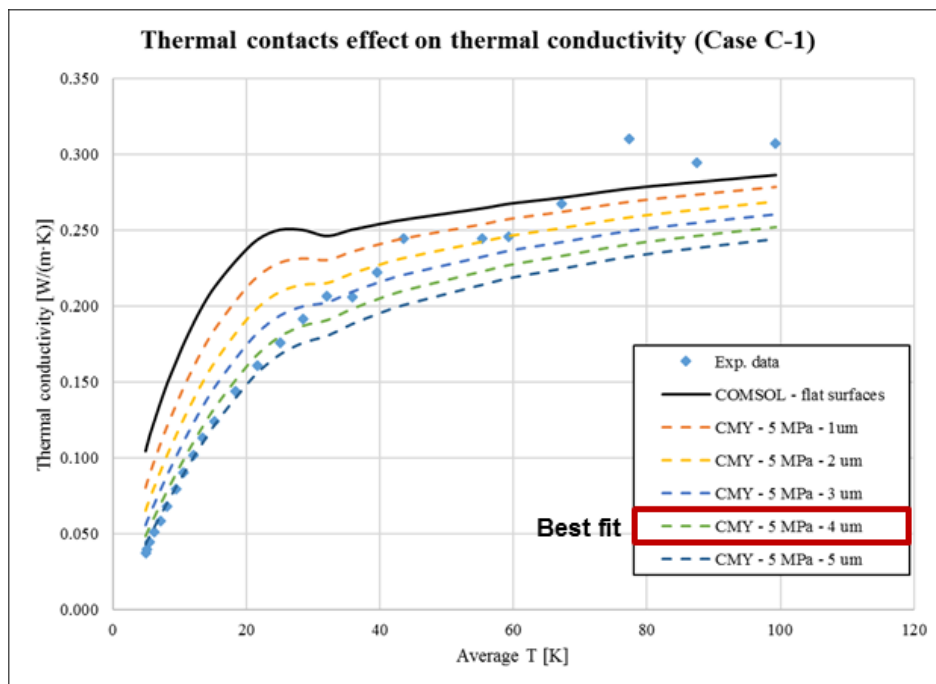


Figure 5.49: Comparison between experimental data and simulated results for thermal contact effect on thermal conductivity (*Case C-1*).

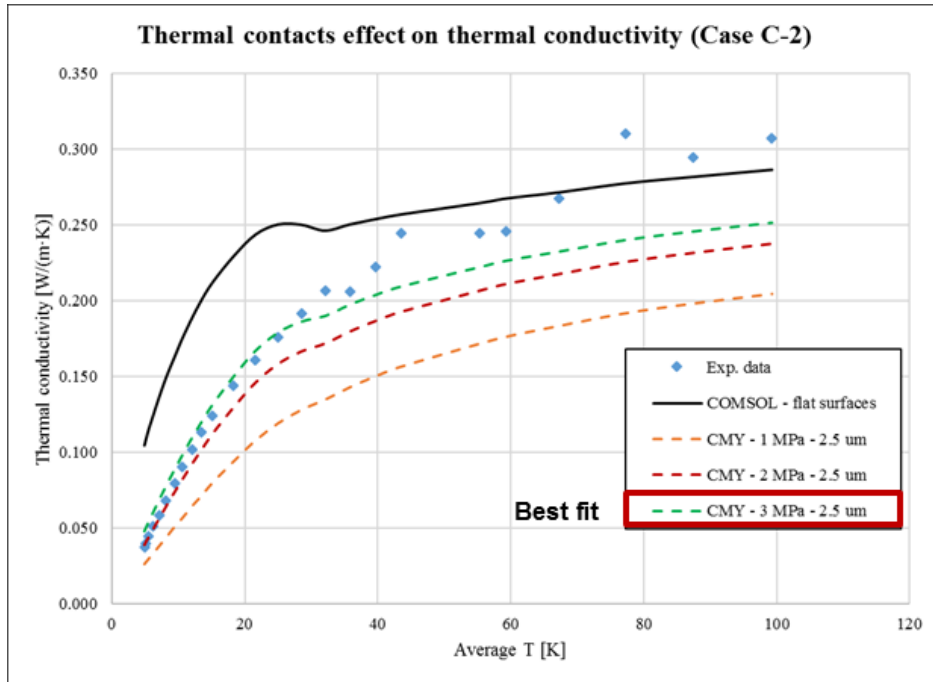


Figure 5.50: Comparison between experimental data and simulated results for thermal contact effect on thermal conductivity (*Case C-2*).

5.4.4 Results of the analogy between thermal and electrical contact resistance

Thermal and electrical contact resistance at the interface between cable strands was evaluated for cables of sample #3 by using the same numerical model and power levels of *Case C*. In order to see possible changes in contact resistance from cable-to-cable, we focused our attention on two cables of the sample, which are *cable #1* and *cable #5* shown in figure 5.51. We used the Cooper-Mikic-Yovanovich parameters which better fit the thermal conductivity experimental data in *Case C-1*, i.e. $\sigma = 4.0 \mu\text{m}$, $m=0.4$, $H_c=3 \text{ GPa}$ and $p=5 \text{ MPa}$. We assumed that the experimental constant \tilde{C} of equation 5.31 is equal to $2.45 \cdot 10^{-8} [\text{W}\Omega\text{K}^{-2}]$, i.e. the Lorenz number. Actually, the constant \tilde{C} changes with contact pressure and surface roughness, but we can consider it constant if the heat transfer between two contacting surfaces is dominated by electron transport [Hyo2018], and this condition is quite well verified at high and very low temperature [Bre1973]. A series of experiments was carried-out by Y. Hyodo et al. [Hyo2018] to investigate on the experimental thermal constant \tilde{C} as a function of contact pressure and surface roughness for two conductive materials in contact.

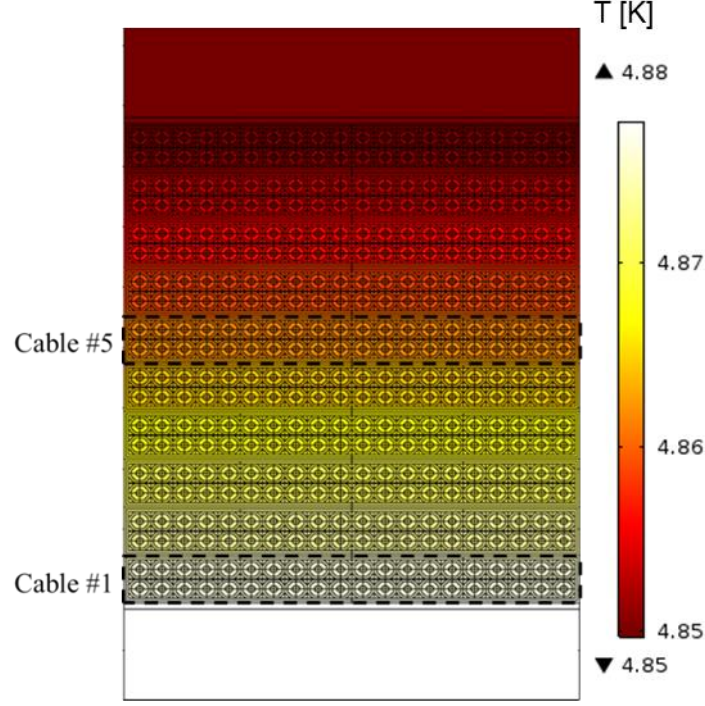


Figure 5.51: Thermal map of cable stacks sample. Cables #1 and #5 were taken as reference to analyze the interstrand thermal and electrical resistance.

After having obtained the thermal map of cable stack sample, shown in figure 5.50, we evaluated the temperature gradient ΔT_i due to the thermal contact resistance at the interface between two strands of a cable i , as follows:

$$\Delta T_i = T_{\text{upper}_i} - T_{\text{lower}_i} \quad (5.32)$$

where T_{upper_i} and T_{lower_i} are respectively the computed temperature at the upper and lower part of the interstrand interface; the power P (in W) equivalent to the heat flow passing through the interface was calculated as:

$$P = \frac{P_{\text{upper}_i} + P_{\text{lower}_i}}{2} \quad (5.33)$$

Then, we obtained the interstrand thermal resistance R_{th_i} (in K/W) for the considered i -cable:

$$R_{\text{th}_i} = \frac{\Delta T_i}{P} \quad (5.34)$$

To estimate the interstrand electrical resistance, we firstly calculated the average temperature of the contact surfaces T_{ct_i} as follows:

$$T_{cti} = \frac{T_{upper_i} + T_{lower_i}}{2} \quad (5.35)$$

Then from Wiedemann-Franz law the interstrand electrical resistance (in Ω) was calculated as follows:

$$R_{eli} = \tilde{C} R_{thi} T_{cti} \quad (5.36)$$

Figures 5.52 and 5.53 presents respectively the thermal contact resistance and the electrical contact resistance as a function of the average temperature of the contact surfaces between strands of investigated cables. Values of computed thermal and electrical contact resistance are basically the same for considered cables, because there are no important changes in gradient temperature and average temperature from one cable to another in the sample. Results of electrical contact resistance are quantitatively in accordance to values found in literature [de-Rap2014, Bres2017] of adjacent contact resistance for Nb₃Sn Rutherford cables. Furthermore, the calculated electrical resistance of stainless-steel core is in the order of n Ω and it can be considered negligible in respect to the interstrand electrical contact resistance.

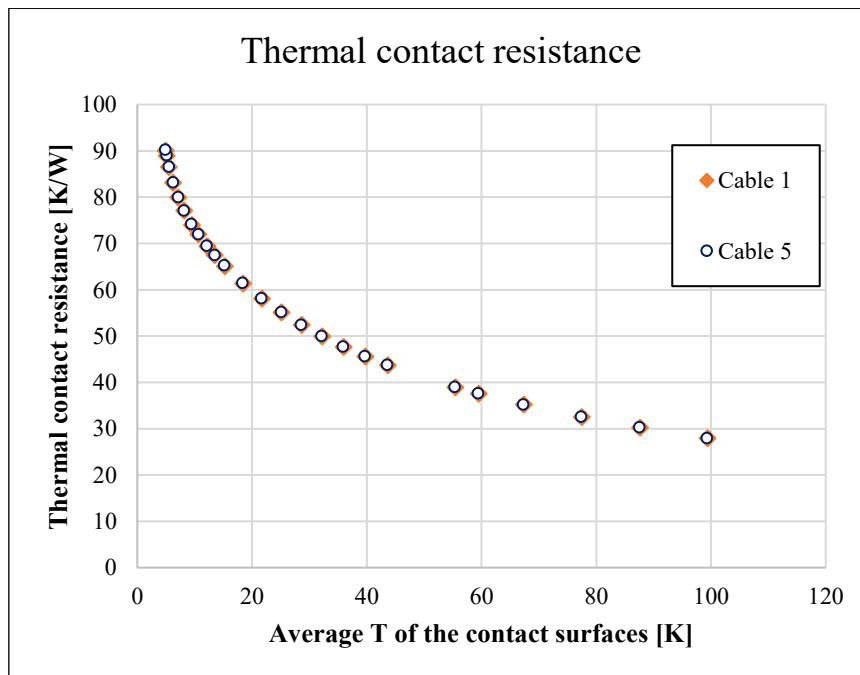


Figure 5.52: Thermal contact resistance as a function of the average temperature of the contact surfaces for cables #1 and #5, using $C=2.45 \cdot 10^{-8}$ ($W\Omega K^{-2}$).

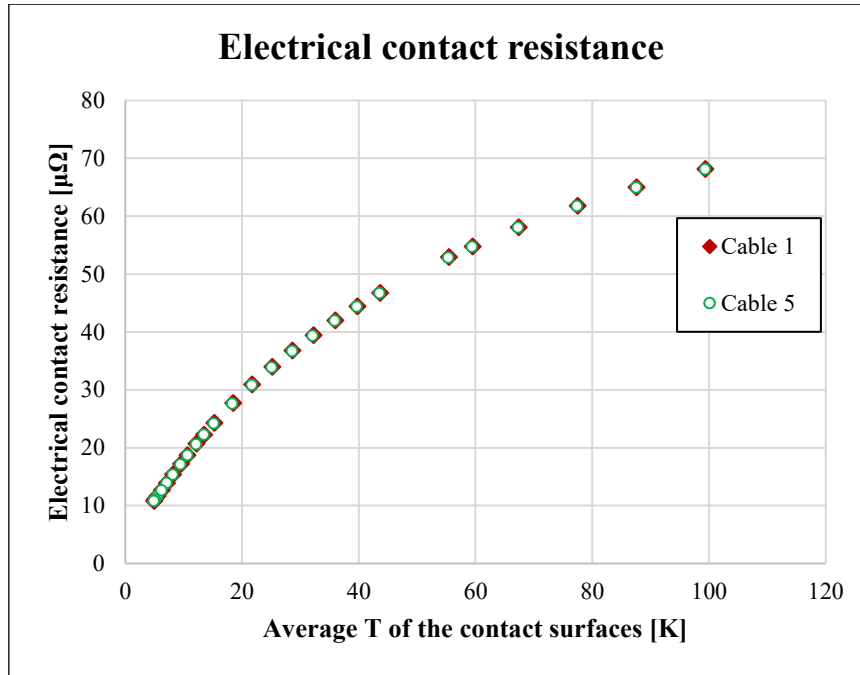


Figure 5.53: Electrical contact resistance as a function of the average temperature of the contact surfaces for cables #1 and #5, using $C=2.45 \cdot 10^{-8}$ ($W\Omega K^{-2}$).

5.5 Concluding remarks on cable stacks analysis

This chapter describes in first part the results from the experimental campaign has been launched to characterize the thermal properties of Nb_3Sn coils. Table 5.53 summarizes the thermal conductivity at 10 K for the different investigated samples and compares it with reference values available in literature. In the second part, a numerical model of epoxy-impregnated Nb_3Sn cable stacks sample was carried-out to reproduce the thermal conductivity measurements performed at CERN Cryolab. Strand transposition effect and thermal contacts were also considered in the model. The model is based on solving the heat diffusion equation inclusive of equations of CMY model to estimate the thermal conductivity of the sample. Finally, thermal contact resistance was computed and translated in electrical contact resistance for the contacting surfaces between strands of cables. The stability of the model has been well verified, as well as the good accuracy in prediction of experimental measurements. The model could be improved by launching an experimental campaign that could permit to measure the CMY model parameters for each considered material. In addition, the presented numerical model could be adapted to study the thermal conductivity measurements of other coil samples.

Table 5.8: Thermal conductivity of investigated samples at 10 K.

	Thermal conductivity @ 10 K [W/(m·K)]	Coil Pack	Insulation
Coil samples	Kapton-Prepeg + Epoxy (FNAL-INFN-LASA)	0.2	0.05
	E-glass tape + Epoxy (FNAL-INFN-LASA)	0.2	0.05
	S-glass + Mica + Epoxy, coil (CERN)	0.2 (azimuthal) / 0.85 (radial)	0.035
	S-glass + Mica + Epoxy, ten stack (CERN)	0.1	0.014
Slab samples	Epoxy CTD101K (CERN)	0.052 (wo correction)/ 0.075 (w correction)	
	Epoxy CTD101K + S-2 glass 636 11 TEX (CERN)	0.064 (wo correction)/ 0.104 (w correction)	
	Epoxy CTD101K + S-2 glass 636 11 TEX + ceramic binder CTD-1202 (CERN)	0.068 (wo correction)/ 0.118 (w correction)	
	Epoxy CTD101K + S-2 glass 636 11 TEX + Mica COGEBI FIROX® P 63P24A + ceramic binder CTD-1202 (CERN)	0.041 (wo correction)/ 0.053 (w correction)	
Bulk samples	Epoxy CTD101K (CERN)	0.116	
References	G10 (Cryosoft database)	0.11	
	Epoxy (Cryosoft database)	0.06	

Conclusions

The research included in this thesis studied the protection of high-field accelerator magnets using quench protection heaters and the thermal conductivity of Nb₃Sn coil samples. A numerical heater-coil thermal model was built in COMSOL to evaluate the heater delays as a function of a large number of parameters for MQXF and 11 T magnet short models. The model solves the heat diffusion equation from heater to cable in two dimensions and returns the quench heater delay when the temperature of the cable reaches the current sharing temperature. From transient simulations, the quench heater delay as a function of the magnet current for different cases, thermal maps of the coil, the temperature evolution in the cable as well as in the heater and the quench location were computed. The implemented numerical model results stable and permits to evaluate the impact of changing powering parameters or materials on quench heater delays. Performance of MQXFS heaters are in agreement with expectations. The proposal of insert quench heaters in the inter layer of 11 T magnet has permitted to have a small reduction of the quench load. The proposal to add an additional layer of 0.2 mm between heater and insulated cable for both magnets translates into an increase of a factor 3 in the heater delays. Results from simulations are in good agreement with experimental data, with a good reproducibility at high current. The heater-to-coil heat transfer model could be improved by considering thermal contact between layers and including AC losses. Finally, the evaluation of the analytical adiabatic temperature of the heater has permitted to estimate the maximum temperature that heater could reach in ideal condition.

Thermal conductivity of the different insulation layers used in Nb₃Sn impregnated coils plays a key role in thermodynamic processes during a quench, therefore a good characterization is needed. An experimental campaign has been launched to characterize the thermal properties of Nb₃Sn coils. From experimental results, the thermal conductivity measured in impregnated S2-glass is close to the typical value for G10 available in literature. When including mica to the insulation lay-out, thermal conductivity decreases by almost a factor 2. Thermal conductivity of thin epoxy samples gives value close to the literature values, but the thermal conductivity of bulk samples is higher than expected. Measurements on coil samples in the azimuthal direction are close to previous measurements in FNAL and INFN-LASA. A large difference was found between coil samples and ten stack samples. We have found a factor 2 difference between the measurements on coil segments and ten stacks which has not been fully understood.

Successively, a numerical investigation was carried-out in order to assess the thermal conductivity of impregnated Nb₃Sn cable stacks sample. A numerical model of epoxy-impregnated Nb₃Sn cable stacks sample was built in COMSOL to reproduce the thermal conductivity measurements performed at CERN Cryolab. From steady simulations, thermal conductivity curve, the thermal maps, and the heat flux magnitude maps inclusive of heat streamlines were computed for the coil sample. Strand transposition effect on the overall thermal conductivity of the sample was taken into account through an analytical calculation. Then, a thermal analysis was performed considering including interfacial thermal contacts inside cable strands, by using the Cooper-Mikic-Yovanovich plastic model, in order to have a more accurate evaluation of thermal conductivity of sample. Finally, thermal contact resistance at the interface between two

adjacent strands was computed and translated in electrical contact resistance. From results, it appears that thermal levels are considerably similar to those obtained during experimental tests on cable stacks sample. Similarly, the simulated thermal behavior inside strands well represents that of a real Nb₃Sn cable under thermal test. The thermal conductivity analysis coming from our investigation results in good agreement with literature evidences and experimental finding, both qualitatively and quantitatively. However, further efforts are needed to experimentally measure the four characteristic parameters of CMY model for each considered material and the experimental constant of Wiedemann-Franz law, in order to have a more accurate evaluation of thermal phenomena inside cable strands. Moreover, the presented numerical model could be adopted to study also the overall thermal conductivity of other coil samples.

Annex 1

Section 1: Real coil resistive voltage signals from tests MBHSP106 magnet

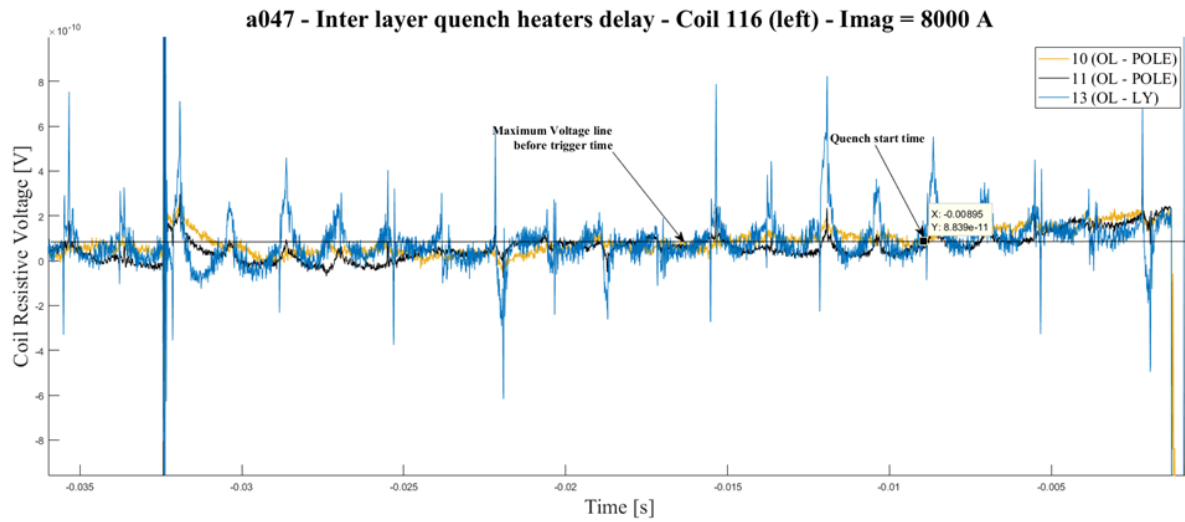


Figure AS1.1: Coil resistive voltage as a function of time for coil 116 (InL heaters) at $I_{mag}=8$ kA

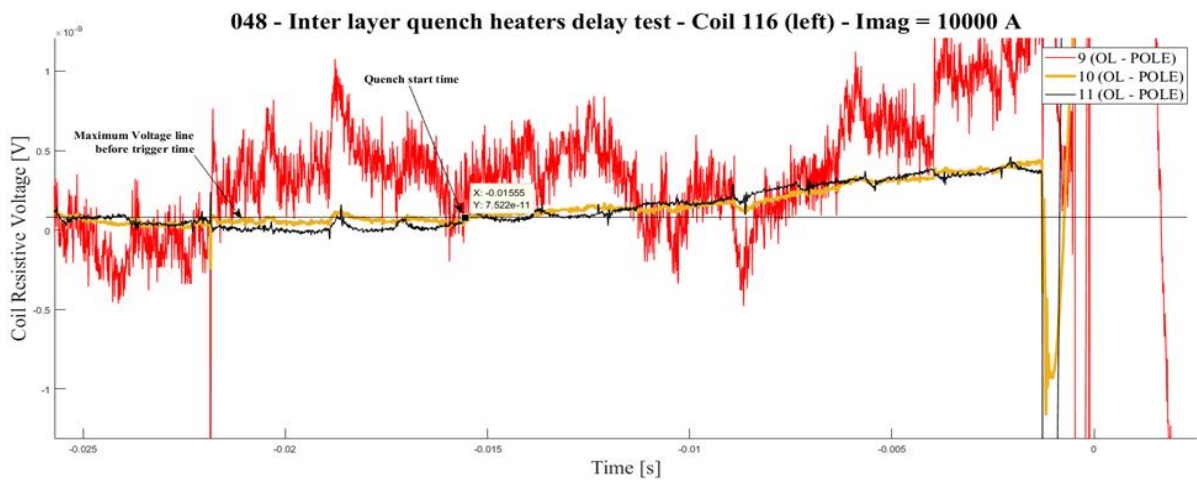


Figure AS1.2: Coil resistive voltage as a function of time for coil 116 (InL heaters) at $I_{mag}=10$ kA

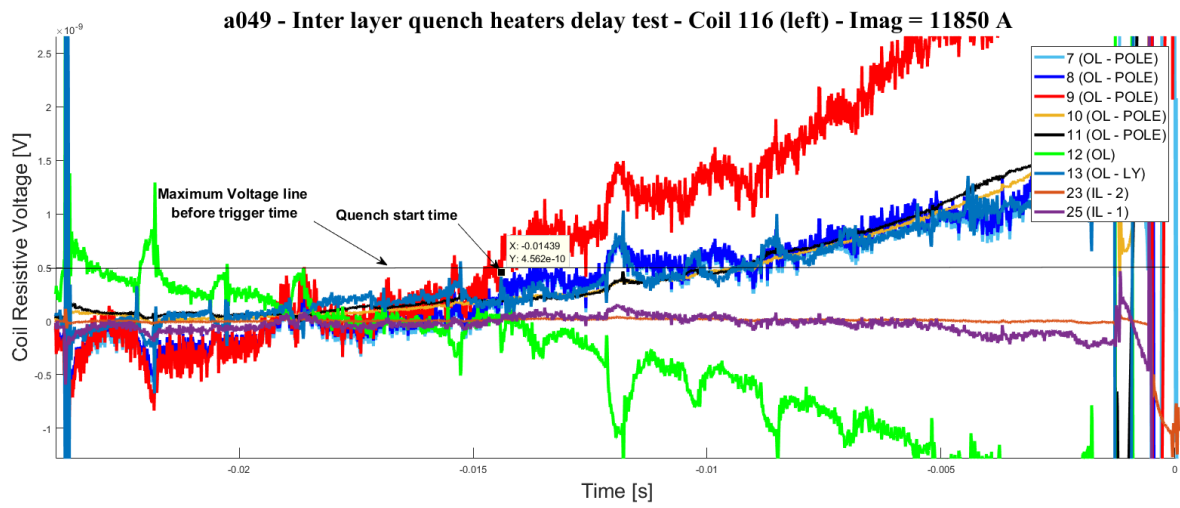


Figure AS1.3: Coil resistive voltage as a function of time for coil 116 (InL heaters) at $I_{mag}=11.85 \text{ kA}$

Annex 2

Section 1: Thermal conductivity measurements for single components

Table AS1.1: Thermal conductivity steady-state measurements of sample #1.

T_{ave} [K]	k_{sample} [W/(m·K)]
2.98	0.0426
3.11	0.0440
3.33	0.0462
3.60	0.0476
3.92	0.0481
4.29	0.0485
4.66	0.0484
5.01	0.0485
5.35	0.0484
5.90	0.0481
6.66	0.0483
7.57	0.0492
8.45	0.0495
9.21	0.0505
9.87	0.0516
10.47	0.0526
11.19	0.0534
11.90	0.0552
12.58	0.0560
13.30	0.0571
15.63	0.0610
18.70	0.0677
21.94	0.0737
25.82	0.0785
30.28	0.0880

Table AS1.2: Thermal conductivity steady-state measurements of sample #2.

T_{ave} [K]	k_{sample} [W/(m·K)]
6.04	0.0863
6.42	0.0883
7.11	0.0938
7.99	0.1042
11.39	0.1241
15.69	0.1735
20.57	0.2150
25.79	0.2539
33.11	0.2467
37.01	0.2704
40.68	0.3945
64.89	0.3662
79.14	0.6399

Table AS1.3: Thermal conductivity steady-state measurements of sample #3.

T_{ave} [K]	k_{sample} [W/(m·K)]
2.86	0.0345
3.05	0.0368
3.10	0.0375
3.35	0.0415
3.59	0.0424
4.28	0.0462
4.73	0.0507
5.40	0.0508
5.94	0.0518
7.53	0.0565
8.48	0.0591
9.21	0.0610
10.59	0.0652
12.72	0.0716
15.69	0.0799
17.18	0.0817
18.74	0.0856
20.45	0.0922
20.45	0.0875
22.26	0.0954
22.26	0.0906
24.11	0.0984

24.11	0.0946
26.16	0.0982
26.26	0.0951
28.44	0.1039
28.44	0.1007
30.74	0.1076
34.54	0.1082
35.98	0.1186
85.20	0.2175
116.53	0.2264
131.20	0.2163
224.99	0.2946
233.49	0.3014
240.07	0.3075
247.30	0.3137
253.33	0.3183
260.47	0.3219
267.32	0.3266
293.82	0.3498
293.82	0.3303
293.81	0.3146

Table AS1.4: Thermal conductivity steady-state measurements of sample #4.

T_{ave} [K]	k_{sample} [W/(m·K)]
2.95	0.0341
3.06	0.0352
3.28	0.0382
3.57	0.0410
3.91	0.0438
4.32	0.0462
4.72	0.0484
5.19	0.0508
5.41	0.0514
5.94	0.0543
6.65	0.0568
7.52	0.0600
8.45	0.0637
9.18	0.0659
9.92	0.0686
10.59	0.0708
11.32	0.0735
12.03	0.0759

12.72	0.0783
13.50	0.0810
14.40	0.0846
15.66	0.0880
17.15	0.0930
18.78	0.0982
20.41	0.1004
22.18	0.1067
23.98	0.1146
26.16	0.1165
28.44	0.1220
30.63	0.1266
33.04	0.1274
35.78	0.1296
40.44	0.1424
45.70	0.1538
50.24	0.1730
55.32	0.1837
60.35	0.1957
65.24	0.2042
70.78	0.2150
80.29	0.2330
90.57	0.2439
100.48	0.2453
110.03	0.2568
120.71	0.2673
130.48	0.2750
140.52	0.2838
150.22	0.2929
160.88	0.2980
170.08	0.3040
180.81	0.3120
189.74	0.3332
200.58	0.3256
210.88	0.3478
220.88	0.3569
232.22	0.3736
283.14	0.3600
286.84	0.3757

Table AS1.5: Thermal conductivity steady-state measurements of sample #5.

T_{ave} [K]	k_{sample} [W/(m·K)]
2.91	0.0139
3.06	0.0152
3.32	0.0169
3.61	0.0186
3.95	0.0203
4.34	0.0219
4.75	0.0236
5.24	0.0253
5.46	0.0262
6.00	0.0279
6.71	0.0300
7.60	0.0328
8.55	0.0355
9.33	0.0373
9.94	0.0389
10.61	0.0404
11.30	0.0424
12.03	0.0442
12.89	0.0479
13.52	0.0474
13.70	0.0474
14.48	0.0500
14.53	0.0500
15.74	0.0520
17.21	0.0547
18.84	0.0580
20.52	0.0612
22.39	0.0635
24.24	0.0646
26.40	0.0652
28.64	0.0658
28.64	0.0703
31.02	0.0705
33.41	0.0699
36.38	0.0699
36.38	0.0699
290.53	0.2411

Table AS1.6: Thermal conductivity steady-state measurements of sample #7.

T_{ave} [K]	k_{sample} [W/(m·K)]
2.93	0.0466
3.09	0.0480
3.58	0.0530
4.26	0.0603
5.15	0.0731
5.84	0.0748
6.03	0.0778
6.64	0.0808
7.43	0.0851
7.57	0.0870
9.22	0.0968
10.49	0.1042
12.01	0.1186
13.45	0.1213
15.81	0.1318
18.99	0.1428
22.77	0.1570
27.00	0.1643
31.55	0.1806
37.07	0.1832
296.11	0.8422

Table AS1.7: Thermal conductivity steady-state measurements of sample #8.

T_{ave} [K]	k_{sample} [W/(m·K)]
4.33	0.0596
4.46	0.0608
4.49	0.0610
4.82	0.0639
4.86	0.0641
5.30	0.0676
5.62	0.0701
5.85	0.0714
5.88	0.0716
6.78	0.0775
7.09	0.0791
7.97	0.0843
8.36	0.0863
9.67	0.0934
10.97	0.1010
12.37	0.1140
13.59	0.1140
14.87	0.1200
16.20	0.1270
16.87	0.1270
17.58	0.1320
18.29	0.1340
19.05	0.1380
19.74	0.1390
21.16	0.1420
22.56	0.1440
23.99	0.1450
25.09	0.1550
26.63	0.1590
28.20	0.1600
29.79	0.1640
31.42	0.1640
33.21	0.1670
35.19	0.1730
42.20	0.1800

Section 2: Thermal conductivity measurements for coil segments

Table AS2.1: Thermal conductivity steady-state measurements of coil sample #1 and computed thermal conductivity for insulation.

T_{ave} [K]	k_{sample} [W/(m·K)]	k_{ins} [W/(m·K)]
3.34	0.2946	0.0096
3.38	0.2998	0.0098
3.77	0.3431	0.0112
4.39	0.4056	0.0132
5.05	0.4653	0.0152
6.01	0.5414	0.0176
7.64	0.6523	0.0212
9.26	0.7530	0.0245
10.60	0.8268	0.0269
12.00	0.8944	0.0291
13.41	0.9577	0.0312
15.57	1.0421	0.0339
18.57	1.1431	0.0372
21.76	1.2453	0.0406
25.51	1.3345	0.0435
29.92	1.4145	0.0461
48.90	1.9135	0.0623
61.75	2.0530	0.0669
72.84	2.2159	0.0722
83.20	2.3866	0.0777
93.18	2.5378	0.0827
102.97	2.6295	0.0857
112.66	2.8525	0.0929
122.15	2.9490	0.0961
131.42	3.0630	0.0998
140.45	3.2027	0.1043
149.22	3.2626	0.1063
157.69	3.3661	0.1097
165.89	3.4724	0.1131
173.78	3.5243	0.1148
181.43	3.5671	0.1162
189.04	3.6810	0.1199
203.35	3.8266	0.1247
209.27	3.9425	0.1284
214.91	3.9544	0.1288

220.26	4.0535	0.1320
225.33	4.0716	0.1326
230.14	4.1011	0.1336
234.69	4.2169	0.1374
238.97	4.2814	0.1395
242.99	4.1782	0.1361
246.78	4.1840	0.1363
250.33	4.2751	0.1393
253.65	4.3304	0.1411
256.75	4.2408	0.1381
259.66	4.3889	0.1430
262.38	4.1915	0.1365
264.91	4.2818	0.1395
267.29	4.4065	0.1435
269.50	4.2604	0.1388
271.57	4.4450	0.1448
273.50	4.3142	0.1405

Table AS2.2: Thermal conductivity steady-state measurements of coil sample #2 and computed thermal conductivity for insulation.

T_{ave} [K]	k_{sample} [W/(m·K)]	k_{ins} [W/(m·K)]
3.31	0.0508	0.0090
3.46	0.0532	0.0095
3.64	0.0572	0.0102
3.87	0.0618	0.0110
3.87	0.0625	0.0111
3.88	0.0622	0.0110
4.00	0.0649	0.0115
4.36	0.0718	0.0128
4.46	0.0736	0.0131
4.46	0.0736	0.0131
4.53	0.0750	0.0133
4.53	0.0750	0.0133
4.90	0.0824	0.0146
5.13	0.0885	0.0157
5.18	0.0885	0.0157
5.50	0.0944	0.0168
6.11	0.1059	0.0188
6.37	0.1112	0.0198
6.37	0.1112	0.0198
7.71	0.1370	0.0243
7.91	0.1400	0.0249
9.30	0.1648	0.0293

9.48	0.1678	0.0298
10.59	0.1872	0.0333
10.74	0.1885	0.0335
11.93	0.2050	0.0364
12.00	0.2087	0.0371
13.36	0.2308	0.0410
13.44	0.2286	0.0406
15.61	0.2555	0.0454
18.60	0.2885	0.0513
18.66	0.2900	0.0515
21.80	0.3145	0.0559
25.56	0.3408	0.0606
25.92	0.3453	0.0614
26.99	0.3487	0.0620
30.02	0.3627	0.0645
37.44	0.4023	0.0715
43.48	0.4284	0.0761
43.84	0.4285	0.0761
48.18	0.4686	0.0833
59.98	0.4888	0.0869
59.98	0.4888	0.0869
68.03	0.5144	0.0914
93.44	0.5910	0.1050

Table AS2.3: Thermal conductivity steady-state measurements of coil sample #3.

T_{ave} [K]	P [W]	k_{sample} [W/(m·K)]	k_{ins} [W/(m·K)]	ΔT [K]
4.89	8.20E-05	0.0374	0.0058	0.0768
5.08	8.18E-05	0.0400	0.0062	0.0718
5.49	4.16E-05	0.0446	0.0069	0.0327
6.20	8.10E-05	0.0510	0.0079	0.0557
7.09	8.05E-05	0.0588	0.0091	0.0480
8.13	7.99E-05	0.0684	0.0106	0.0409
9.42	5.82E-04	0.0797	0.0123	0.2560
10.60	7.87E-05	0.0905	0.0140	0.0305
12.08	5.75E-04	0.1019	0.0158	0.1978
13.45	7.76E-05	0.1133	0.0175	0.0240
15.12	1.06E-03	0.1241	0.0192	0.2996
18.32	1.31E-03	0.1438	0.0223	0.3182
21.61	1.29E-03	0.1606	0.0249	0.2820
25.03	1.28E-03	0.1761	0.0272	0.2550
28.52	1.27E-03	0.1916	0.0296	0.2326
32.06	1.63E-03	0.2064	0.0320	0.2773
35.80	1.82E-03	0.2061	0.0319	0.3104

39.61	1.81E-03	0.2220	0.0344	0.2864
43.48	1.80E-03	0.2444	0.0378	0.2587
55.27	1.99E-03	0.2445	0.0379	0.2847
59.34	1.77E-03	0.2454	0.0380	0.2528
67.23	1.76E-03	0.2676	0.0414	0.2302
77.31	1.74E-03	0.3101	0.0480	0.1970
87.46	1.73E-03	0.2946	0.0457	0.2058
99.25	1.72E-03	0.3068	0.0475	0.1963

Table AS2.4: Simulated thermal conductivity steady-state tests of coil sample #3.

Test run #	T_{ave}	T_1	T_2	ΔT_{COMSOL}	P	$k_{sample-COMSOL}$
[-]	[K]	[K]	[K]	[K]	[W]	[W/(m·K)]
1	4.89	4.8776	4.8497	0.0279	8.20E-05	0.1050
2	5.08	5.0719	5.0449	0.0270	8.18E-05	0.1082
3	5.49	5.4910	5.4781	0.0129	4.16E-05	0.1150
4	6.20	6.1984	6.1752	0.0232	8.10E-05	0.1247
5	7.09	7.0869	7.0659	0.0210	8.05E-05	0.1366
6	8.13	8.1253	8.1062	0.0191	7.99E-05	0.1496
7	9.42	9.4148	9.2876	0.1272	5.82E-04	0.1633
8	10.60	10.6012	10.5852	0.0160	7.87E-05	0.1757
9	12.08	12.0875	11.9791	0.1084	5.75E-04	0.1893
10	13.45	13.4487	13.4349	0.0138	7.76E-05	0.2007
11	15.12	15.1530	14.9750	0.1780	1.06E-03	0.2128
12	18.32	18.3584	18.1563	0.2020	1.31E-03	0.2305
13	21.61	21.6615	21.4735	0.1881	1.29E-03	0.2452
14	25.03	25.0854	24.9039	0.1814	1.28E-03	0.2520
15	28.52	28.5874	28.4073	0.1801	1.27E-03	0.2518
16	32.06	32.1610	31.9260	0.2350	1.63E-03	0.2480
17	35.80	35.9067	35.6485	0.2582	1.82E-03	0.2523
18	39.61	39.7155	39.4623	0.2532	1.81E-03	0.2558
19	43.48	43.6016	43.3531	0.2485	1.80E-03	0.2590
20	55.27	55.3956	55.1297	0.2659	1.99E-03	0.2666
21	59.34	59.4431	59.2088	0.2342	1.77E-03	0.2697
22	67.23	67.3445	67.1155	0.2290	1.76E-03	0.2738
23	77.31	77.4329	77.2107	0.2222	1.74E-03	0.2799
24	87.46	87.5735	87.3563	0.2172	1.73E-03	0.2843
25	99.25	99.3619	99.1497	0.2122	1.72E-03	0.2890

Table AS2.5: Thermal conductivity quasi steady-state measurements of coil sample #3.

T_{ave} [K]	k_{sample} [W/(m·K)]	k_{ins} [W/(m·K)]
60.08	0.2634	0.0408
70.01	0.2843	0.0440
80.01	0.3020	0.0468
90.15	0.3209	0.0497
100.06	0.3384	0.0524
111.13	0.3568	0.0553
125.41	0.3942	0.0611
139.82	0.4257	0.0659
152.09	0.4572	0.0708
163.55	0.4548	0.0704
171.35	0.4634	0.0718
182.40	0.5018	0.0777
199.74	0.5031	0.0779

References

- [AGY] AGY, *Product information: 636 S-2 Glass Yarn*, available in: https://www.agy.com/wp-content/uploads/2014/03/636_S-2_Yarn-Aero-space.pdf.
- [Amb2011] Ambrosio G., Andreev N., Anerella M., Barzi E., Bingham B., Bocian D., Bossert R., Caspi S., Chlachidize G., Dietderich D. and Escallier J., 2011. Test results of the first 3.7 m long Nb₃Sn quadrupole by LARP and future plans, *IEEE Transactions on Applied Superconductivity*, 21 (3), pp. 1858-1862.
- [And2001] Andreev N., Arkan T., Bauer P., Bossert R., Brandt J., Caspi S., Chichili D. R., Carson J., DiMarco J., Feher S. and Ghosh A. 2001. Field quality in Fermilab-built models of quadrupole magnet for the LHC interaction region. *IEEE transactions on applied superconductivity*, 11 (1), pp. 1566-1569.
- [Apo2015] Apollinari G., Béjar Alonso I., Brüning O., Lamont M. and Rossi L., 2015. *High-Luminosity Large Hadron Collider (HL-LHC): Preliminary Design Report (CERN) Rep.* CERN CERN-2015-005.
- [Bar2013] Barth C., 2013, *High Temperature superconductor cable concepts for fusion magnets* (Vol. 7). KIT Scientific Publishing.
- [BNL] Brookhaven National laboratory database. [Online]. Available: <http://materialdatabase.magnet.fsu.edu/Copper.htm>.
- [Bor2001] Bordry F. and Thiesen H., 2001. LHC inner triplet powering strategy. In *Proceedings of the Particle Accelerator Conference 2001* (Vol. 1, pp. 636-635). IEEE.
- [Borg2016] Borges de Sousa P., 2016. *Measurement Report of the Thermal Conductivity/Conductance of Impregnated Nb₃Sn coil samples: Coil sample #3, 10 stack parallel sample*, CERN TE/CRG-CI.
- [Borg2016a] Borges de Sousa P., 2017. *Measurement Report of the Thermal Conductivity/Conductance of Impregnated Nb₃Sn coil samples: Coil sample #8: S-2 glass 636 11 TEX reacted without ceramic binder and impregnated in CTD-101K resin, 7 mm-thick sample*, CERN TE/CRG-CI.
- [Borg2016b] Borges de Sousa P., 2016. *Measurement Report of the Thermal Conductivity/Conductance of Impregnated Nb₃Sn coil samples - 11 TESLA dipole samples: CTD-101K bulk sample*, CERN TE/CRG-CI.
- [Borg2016c] P. Borges de Sousa, 2016. *Measurement Report of the Thermal Conductivity/Conductance of Impregnated Nb₃Sn coil samples - 11 TESLA dipole samples: sample #3 S-2 glass 636 11 tex reacted without ceramic binder and impregnated in CTD-101K resin; sample #4 S-2 glass 636 11 tex reacted w/ ceramic binder CTD-1202 and impregnated in CTD-101K resin*, CERN TE/CRG-CI.

- [Bot2009] Bottura L. and Bordini B., 2009. $J_c(B, T, \epsilon)$ Parametrization for the ITER Nb₃Sn Production. *IEEE Transactions on Applied Superconductivity*, 19 (CERN-AT-2008-036), pp. 1521-1524.
- [Boz2016] Bozza G., Malecha Z. M. and Van Weelderen R., 2016. Development and application of a generic CFD toolkit covering the heat flows in combined solid-liquid systems with emphasis on the thermal design of HiLumi superconducting magnets. *Cryogenics*, 80, pp. 253-264.
- [Bre1973] Brechna H., 1973. *Superconducting Magnet Systems*, Springer, Berlin, Germany, 1st Ed.
- [Bres2017] Breschi M., Felcini E. and Bottura L., 2017. Quench Level of the HL-LHC Nb₃Sn IR Quadrupoles. *IEEE Transactions on Applied Superconductivity*, 27 (4), pp. 1-5.
- [Brü2015] Brüning O. and Rossi L., 2015. *The High Luminosity Large Hadron Collider: the new machine for illuminating the mysteries of Universe* (Vol. 24). World Scientific Publishing Company.
- [CERN] Measurements at CERN, private communication.
- [CERN1991] CERN document server. Aerial view of CERN and the surrounding region. [Online]. Available: <http://cds.cern.ch/record/39026>.
- [CERN2009] CERN press release. Two circulating beams bring first collisions in the LHC. [Online]. Available: <http://press.cern/press-releases/2009/11/two-circulating-beams-bring-first-collisions-lhc>.
- [CERN2012a] CERN document server. The accelerator complex. [Online]. Available: <https://home.cern/about/accelerators>.
- [CERN2012b] CERN document server. ALICE: A Large Ion Collider. [Online]. Available: <https://home.cern/about/experiments/alice>.
- [CERN2012c] CERN document server. ATLAS: The largest volume particle detector ever built. [Online]. Available: <https://home.cern/about/experiments/atlas>.
- [CERN2012d] CERN document server. CMS: The Compact Muon Solenoid. [Online]. Available: <https://home.cern/about/experiments/cms>.
- [CERN2012e] CERN document server. LHCb: The Large Hadron Collider beauty experiment. [Online]. Available: <https://home.cern/about/experiments/lhcb>.
- [CERN2012f] CERN document server. Higgs within reach. [Online]. Available: <https://home.cern/about/updates/2012/07/higgs-within-reach>.
- [CERN2012g] CERN document server. Experiments. [Online]. Available: <https://home.cern/about/experiments>.
- [CERN2012h] CERN document server. Radiofrequency cavities. [Online]. Available: <https://home.cern/about/engineering/radiofrequency-cavities>

- [CERN2013] CERN document server. CERN congratulates Englert and Higgs on Nobel in physics. [Online]. Available: <https://home.cern/about/updates/2013/10/CERN-congratulates-Englert-and-Higgs-on-Nobel-in-physics>.
- [CERN2014] CERN document server. The Higgs boson. [Online]. Available: <https://home.cern/topics/higgs-boson>.
- [CERN2014a] CERN document server. Coiled cable. [Online]. Available: <https://home.cern/images/2014/07/coiled-cable>.
- [CERN2015] CERN document server. The High-Luminosity LHC. [Online]. Available: <https://home.cern/topics/high-luminosity-lhc>.
- [CERN2016] CERN document server. The CERN accelerator complex. [Online]. Available: <https://cds.cern.ch/record/2197559>.
- [CERN2017] CERN document server. ISOLDE. [Online]. Available: <https://home.cern/about/experiments/isolde>.
- [CERNa] CERN presentations, private communication.
- [CERNb] CERN presentations, private communication.
- [CERNc] CERN presentations, private communication.
- [CESUR] Ankara University – Center of Excellence for Superconductivity Research. Low-High temperature superconductivity. [Online]. Available: <http://cesur.en.ankara.edu.tr/low-high-temperature-superconductivity/>.
- [CMY1969] Cooper M. G., Mikic B. B. and Yovanovich M. M., 1969. Thermal contact conductance. *International Journal of heat and mass transfer*, 12 (3), pp. 279-300.
- [CRYO] CryoComp version 5.1. © 2010 Eckels Engineering.
- [deRap2014] de Rapper W. M., 2014. *Thermal stability of Nb₃Sn Rutherford cables for accelerator magnets*, PhD dissertation University of Twente, the Netherlands.
- [Dev1992] Devred A., 1992. Quench origins. In *AIP Conference Proceedings 2001* (Vol. 249, No. 2, pp. 1262-1308). AIP.
- [Dev2004] Devred A., 2004. *Practical low-temperature superconductors for electromagnets*, CERN-2004-006.
- [Eva2008] Evans L. and Bryant P., 2008. LHC machine. *Journal of Instrumentation*, 3 (08), p. S08001.
- [Eva2009] Evans L. 2009. *The Large Hadron Collider: a marvel of technology*. EPFL Press.
- [Fel2012] Felice H., Prestemon S., Ferracin P. and Todesco E., 2012. *Magnet Specifications in Circular Accelerators – USPAS 2012*. [Online]. Available: <https://indico.cern.ch/event/440690/contributions/1089749/attachments/1143439/1638605/U2rr.pdf>.

- [Fer2015] Ferracin P., 2015. Protection of Superconducting Accelerator Magnets – Episode I. [Online]. Available: https://indico.cern.ch/event/440690/contributions/1089767/attachments/1148951/1648371/U12_final.pdf
- [Fer2016] Ferracin P., Ambrosio G., Anerella M., Ballarino A., Bajas H., Bajko M., Bordini B., Bossert R., Cheng D. W. and Chlachidze G., 2016. Development of MQXF: The Nb₃Sn Low- β Quadrupole for the HiLumi LHC. *IEEE Transactions on Applied Superconductivity*, 26 (4), pp. 1-7.
- [Fer2017] Ferracin P., 2017. *Design of Superconducting Magnets for Particle Accelerators and Detectors – Short Course of EUCAS 2017 Conference*. [Online]. Available: <https://indico.cern.ch/event/626645/>.
- [Gia2015] Gianotti F. and Virdee T.S., 2015. The discovery and measurements of a Higgs boson. *Phil. Trans. R. Soc. A*, 373 (2032), p. 20140384.
- [Gme1999] Gmelin E., Asen-Palmer M., Reuther M., and Villar R., 1999. Thermal boundary resistance of mechanical contacts between solids at sub-ambient temperatures. *Journal of Physics D: Applied Physics*, 32 (6), p. R19.
- [Gre1992] Greene A. F., 1992. *Recent status of superconductors for accelerator magnets*. (NO. BNL-47621). Brookhaven National Lab.
- [Gru2005] Grujicic M., Zhao C. L. and Dusel E. C., 2005. The effect of thermal contact resistance on heat management in the electronic packaging. *Applied Surface Science*, 246 (1-3), pp. 290-302.
- [Gur2011] Gurevich A., 2011. To use or not to use cool superconductors? *Nature materials*. 10 (4), p. 255.
- [Has2012] Hasselström A. K. and Nilsson U. E., 2012. *Thermal contact conductance in bolted joints*. Diploma work no. 85/2012 Chalmers University of Technology, Gothenburg, Sweden.
- [Hil2009] Hiltunen I., Jarvela J., Mikkonen R., Stenvall A. and Viljamaa J., 2009. Transverse Thermal Conductivity in an Epoxy Impregnated MgB₂ Coil. *IEEE Transactions on Applied Superconductivity*, 19 (3), pp. 2407-2410.
- [Hin2005] Hindmarsh A. C., Brown P. N., Grant K. E., Lee S. L., Serban R., Shumaker D. E. and Woodward C. S., 2005. SUNDIALS: Suite of nonlinear and differential/algebraic equation solvers. *ACM Transactions on Mathematical Software (TOMS)*, 31 (3), pp. 363-396.
- [Hyo2018] Hyodo Y., Hatakeyama T., Kibushi R. and Ishizuka M., 2018. Measurement of thermal and electrical contact resistance between conductive materials. In *Proceedings of International Conference on Electronics Packaging and iMAPS All Asia Conference (ICEP-IAAC)* (pp. 132-135). IEEE.
- [Imb2003] Imbasciati L., Ambrosio G., Bauer P., Pedrini D., Previtali V., Rossi L. and Volpini G., *Measurements and Modelling of Thermal Conductivity of Impregnated Nb₃Sn Cable Stacks*, Fermi National Accelerator Laboratory, 2003.

- [Imb2003a] Imbasciati L., 2003. *Studies of quench protection in Nb₃Sn superconducting magnets for future particle accelerators*. PhD dissertation Vienna University of Technology, Wien, Austria.
- [Izq2016] Izquierdo Bermudez S., Auchmann B., Bajas H., Bajko M., Bordini B., Bottura L., Chlachidze G., Karppinen M., Rysti J., Savary F. and Willering G., 2016. Quench protection studies of the 11-T Nb₃Sn dipole for the LHC upgrade. *IEEE Transactions on Applied Superconductivity*, 26 (4), pp. 1-15.
- [Izq2017] Izquierdo Bermudez S. et al., 2017. *Overview of the Quench Heater Performance for MQXF, the Nb₃Sn low-β Quadrupole for the High Luminosity LHC*, Presentation for EUCAS 2017 Conference, Geneva.
- [Izq2018] Bermudez S. I., Ambrosio G., Bajas H., Bourcey N., Chlachidze G., Troitino J. F., Ferracin P., Perez J. C., Pincot F-O., Ravaioli E., Santini C., Stoynev S., Todesco E., Sabbi G. L. and Vallone G., 2018. Overview of the Quench Heater Performance for MQXF, the Nb₃Sn low-β Quadrupole for the High Luminosity LHC, *IEEE Transactions on Applied Superconductivity*.
- [Izq2018a] Bermudez S. I., Willering G., Bajas H., Bajko M., Bordini B., Bottura L., Perez J. C., de Rijk G. and Savary F., 2018. Quench Protection of the 11-T Nb₃Sn Dipole for the High Luminosity LHC, *IEEE Transactions on Applied Superconductivity*, 28 (3).
- [Koe2017] Koettig T., Maciocha W., Izquierdo Bermudez S., Rysti J., Tavares S., Cachera F. and Bremer J., 2017. Thermal conductivity measurements of impregnated Nb₃Sn coil samples in the temperature range of 3.5 K to 100 K. In *IOP Conference Series: Materials Science and Engineering* (Vol. 171, No. 1, p. 012103). IOP Publishing.
- [Lee2014] Lee P. J., 2014, Master J_c Plots and Nb₃Sn Scaling Spreadsheet , *ASC maintained pages for The Applied Superconductivity Center*. [Online]. Available: <http://fs.magnet.fsu.edu/~lee/plot/plot.h>.
- [LHCCLOSER] LHC-CLOSER website. LHC parameters. [Online]. Available: http://lhccloser.es/taking_a_closer_look_at_lhc/1.lhc_parameters.
- [LUVATA] Luvata website – Luvata joins forces to develop superconductor technology [Online]. Available: <http://www.luvata.com/es-MX/News-Room/News/Luvata-joins-forces-to-develop-superconductor-technology/?backurl=/es-MX/News-Room/News/>.
- [Mac2014] Maciocha W., 2014. *Thermal conductivity measurement: CTD-101K*, CERN TE/CRG-CI.
- [Man2015] Manfreda G., Bellina F., Bajas H. And Perez J. C., 2015. *Analysis of the quench propagation along Nb₃Sn Rutherford cables with the THELMA code*. Presentation for CHATS-AS Workshop 2015, Bologna, Italy.

- [Man2018] G. Manfreda, 2018. *Review of ROXIE's Material Properties Database for Quench Simulation*, Internal note 2018-1178007 EDMS Nr. 1178007, CERN.
- [Mant2002] Mantelli M. B. H. and Yovanovich M. M., 2002. Thermal Contact Resistance. *Spacecraft Thermal Control Handbook*, Vol. 1, Chap. 16, pp. 599-633.
- [Mar] Marchevsky M.. Quench detection and protection for HTS accelerator magnets [Online]. Available: https://indico.cern.ch/event/396905/contributions/1837518/attachments/1152844/1655698/MM_WAMHTS3.pdf
- [Mes1996] Mess K.-H, Schmueser P. and Wolff S. 1996, *Superconducting accelerator magnets*. World Scientific.
- [MICA] Firox[®] P. [Online]. Available: <http://www.fkaeng.com/userfiles/Firox%20P%20-%20UK%20-%20mv-.pdf>.
- [Nil2017] Nilsson E., Bermudez S. I., Ballarino A., Bordini B., Bottura L., Fleiter J., Lackner F., Loffler C., Perez J. C., Prin H. and de Rijk G., 2017. Design and optimization of the Nb₃Sn 11 T dipole for the high luminosity LHC. *IEEE Transactions on Applied Superconductivity*, 27 (4).
- [NIST] NIST, Material properties database, 2011.
- [NOBEL2013] Nobel Prize website. The Nobel Prize in Physics 2013. [Online]. Available: https://www.nobelprize.org/nobel_prizes/physics/laureates/2013/.
- [Osw2011] Gröbner O., 2011. Overview of the LHC vacuum system. *Vacuum*, 60 (1-2), pp. 25-34.
- [Oud1994] den Ouden A. and ten Kate H. H., 1994. Thermal conductivity of mica/glass insulation for impregnated Nb₃Sn windings in accelerator magnets. *Cryogenics*, 34, pp. 385-388.
- [Rem2011] R. Remsburg, 2011. *Advanced thermal design of electronic equipment*. Springer Science & Business Media.
- [Rep-MBHSP106] Bermudez S. I., Barbagallo C., Willering G., Mangiarotti F. J., 2018. *Report on Quench Protection Tests: MBHSP106*, Internal note 2018-09, EDMS Nr. 2032117, CERN.
- [RepMQXFS5] Bermudez S. I., Troitino J. F., Barbagallo C., Bajas H., 2018. *Report on Quench Protection Tests: MQXFS5*, Internal note 2018-01, EDMS Nr. 1891255, CERN.
- [Rus2011] Russenschuck S., 2011. *Field computation for accelerator magnets: analytical and numerical methods for electromagnetic design and optimization*. John Wiley & Sons.
- [Salmi2014] Salmi T., Arbelaez D., Caspi S., Felice H., Prestermon, Chlachidze G. and ten Kate H. H. J. 2014, Modeling heat transfer from quench protection heaters to superconducting cables in Nb₃Sn magnets, *arXiv preprint arXiv:1401.3939*.

- [Salmi2015c] Salmi T., 2015. *Optimization of Quench Protection Heater Performance in High-Field Accelerator Magnets Through Computational and Experimental Analysis*. PhD dissertation Tampere University of Technology, Tampere, Finland.
- [Sar2015] Sarasola X., 2015. *Inspection of the 2-m long 11 T coil #104 – Position of the conductors and quality of the impregnation*, EDMS 1473645.
- [Sav2003] Savija I., Culham J. R., Yovanovich M. M. and Marotta E. E., 2003. Review of thermal conductance models for joints incorporating enhancement materials. *Journal of thermophysics and heat transfer*, 17 (1), pp. 43-52.
- [S-POWER2015] SuperPower website. [Online]. Available : <http://www.superpower-inc.com/content/2g-hts-wire>.
- [Sri1994] Sridhar M. R. and Yovanovich M. M., 1994. Review of elastic and plastic thermal contact conductance and comparison with experiment. *Journal of Thermophysics and Heat Transfer*, 8 (4), pp. 663-640.
- [Tay2000] Taylor T., 2000. *Superconducting Magnets and RF Cavities for the LHC* (No. CERN-LHC-PROJECT-REPORT-379, pp. 1-10).
- [THERM] THERMOPEDIA™ website, Thermal contact resistance. [Online]. Available: <http://www.thermopedia.com/content/1188>.
- [Tod2013] Todesco E., 2013. Quench limits in the next generation of magnets. In *Conference Proceedings of WAMSDO: Workshop on accelerator magnet superconductors, design and optimization*, CERN-2013-006 10.
- [Val2018] Vallone G., Bordini B. and Ferracin P., 2018. Computation of the Reversible Critical Current Degradation in Nb₃Sn Rutherford Cables for Particle Accelerator Magnets. *IEEE Transactions on Applied Superconductivity*, 28 (4), pp. 1-6.
- [Ver2008] Verweij A., Schmidt R., Gruwé M., Parma V., Thiessen H., Fehér S., Zerlauth M., Denz R., Ponce L., Kain V. and Pojer M., 2008, *Performance of the main dipole magnet circuits of the LHC during commissioning* (No. LHC-PROJECT-Report-11440).
- [Wie2007] Wiedemann H, 2007. *Particle accelerator physics* (Vol. 314). Berlin: Springer.
- [Wil1983] Wilson M. N., 1983. *Superconducting magnets*. Oxford University Press. New York
- [Will2009] Willering G., 2009. *Stability of superconducting Rutherford cables*. PhD dissertation University of Twente, Enschede, the Netherlands.
- [Yov1982] Yovanovich M., 1982. Thermal Contact Correlations, *AIAA paper*, 81, pp. 83-95.
- [Zhe2016] Zheng J., Li Y., Chen P., Yin G., and Luo H., 2016. Measurements of interfacial thermal contact conductance between pressed alloys at low temperatures. *Cryogenics*, 80, pp. 33-43, 2016.

[Zlo2015]

Zlobin A. V., Andreev N., Apollinari G., Auchmann B., Barzi E., Bermudez S. I., Bossert R., Buehler M., Chlachidze G., DiMarco J., Karppinen M., Nobrega F., Novitski I., Rossi L., Smekens D., Tartaglia M., Turrioni D. and Velez G., 2013. 11-T Twin-Aperture Nb₃Sn Dipole Development for LHC Upgrades. *IEEE Transactions on Applied Superconductivity*, 25 (3), pp. 1-9.